Universitetet
i Stavanger

FACULTY OF SCIENCE AND TECHNOLOGY

MASTER'S THESIS

Study programme/specialisation: Engineering Structures and Materials / Mechanical Systems	Spring semester, 2018 Open
Author: Daniel Årrestad Stave	Daniel Å. Stave …………………………………………… (signature of author)

Programme coordinator: Dimitrios Pavlou

Supervisor(s): Knut Erik Teigen Giljarhus, Luca Oggiano

Title of master's thesis:
Cyclist Posture Optimisation using CFD

Credits: 30

Keywords: CFD, OpenFOAM, cyclist science, optimisation, skeleton rigging	Number of pages: 67+6 Stavanger, 1st of June 2018

Title page for Master's Thesis
Faculty of Science and Technology

Universitetet
i Stavanger

Cyclist Posture Optimisation using CFD

Daniel Årrestad Stave

Supervisors:
Associate professor Knut Erik Giljarhus, University of Stavanger
Dr. Luca Oggiano, Norwegian University of Science and Technology,
and Institute for Energy Technology

Faculty of Science and Technology
Department of Mechanical and Structural Engineering and Materials Science

Abstract

A procedure for optimising the posture of a cyclist concerning the drag force predicted by computational fluid dynamics is developed and executed using open-source software only. The computational setup is validated by testing it on simpler geometry, a sphere, for which extensive experimental studies are available for, and results confirmed to have good agreement with experimental studies performed by Achenbach (1972,1974). Five 3D scanned postures of the Team Sky athlete Tao Geoghegan Hart are simulated, and by comparing the drag force of the present result with similar models simulated in the literature, the drag force of the present results are confirmed to be realistic. The relative change in drag of the postures is confirmed to agree with simulations of the same postures using commercial software. The optimisation procedure is based on a single 3D scanning of a given cyclist, which is modified using skeleton rigging. Hence, for the first time, skeleton rigging is utilised to study the optimal posture of a cyclist. The modifications of the cyclist posture are limited to the distance between elbows, elbow extension and distance between hands, and the boundaries of the modifications are defined in such a way that all the resulting postures satisfy the corresponding regulations by International Cycling Union. Simulation results show that a small distance between elbows, minimum elbow extension and any distance between hands, is the favourable combination for reducing the drag force. The elbow extension seems to be the most crucial parameter, secondly the distance between elbows, and then, the distance between the hands. Additionally, a cyclist posture which experiences a small drag force is also characterised by a narrow wake, a small frontal area and a streamlined flow. A regression model is constructed based on the simulation results of optimisation. This regression model did not reveal any new local minimums compared to the simulation results, yet, proved itself useful when analysing the trends of between posture and drag.

Preface

This thesis concludes my Master of Science education in Engineering Structures and Materials with specialisation in Mechanical Systems at the University of Stavanger (UIS), performed throughout spring 2018, at the Department of Mechanical and Structural Engineering and Materials Science, in collaboration with the Norwegian University of Science and Technology (NTNU).

I would like to use this opportunity to thank my supervisor at UIS; Associate professor Knut Erik Giljarhus, and my supervisor at NTNU; Dr Luca Oggiano. I am incredibly grateful for the guidance, shared knowledge, support, patience, time and effort, they have invested in this thesis, making this a thrilling last semester. My supervisors have shown a genuine interest in the topics of discussion and problem solving throughout the thesis, and their willingness to help a confused student shall not be forgotten.

With the help of these people, and the support from my family, friends and girlfriend, this thesis has been a fantastic experience.

Daniel Å. Stave

3rd of June 2018, Grimstad, Norway.

Contents

List of Symbols

Latin letters

Symbol	**Description**	**Unit**
A	Frontal area of the body	m^2
arg_1	Argument of F_1, given by Equation (2.16)	^{o}
C_D	Drag coefficient	$-$
$CD_{k\omega}$	Argument of arg_1, given by Equation (2.17)	$-$
C_f	Friction variation	$-$
C_μ	Constant of Equation (2.13)	$-$
E	Constant in Equation (2.22)	$-$
e_{ra}	Expansion ratio	$-$
D_F	Drag force according to regression model	N
div	Divergence	$-$
E_e	Elbow extension	$-$
E_p	Distance between elbows	$-$
F_1	Blending function given by Equation (2.15)	$-$
F_D	Drag force	N
$grad$	Gradient	$-$
H_p	Distance between hands	$-$
k	turbulent kinetic energy	$\mathrm{kg\ m^2\ s^{-2}}$
L	Characteristic length scale	m
h_T	Total height of viscous mesh	m
n	Direction normal the boundary	$-$
n_{ce}	Number of cell layers	$-$
P	Mean pressure	Pa
p	Pressure	Pa
$p^{'}$	Fluctuating pressure	Pa
Re	Reynolds number	$-$
T_i	Turbulence intensity	$-$
t	Time	s
U_∞	Free-stream velocity	m/s
$\mathrm{div}\ \mathbf{U}$	Volumetric deformation	s^{-1}
U	Mean velocity in the x-direction	m/s
u	Velocity in the x-direction	m/s
$u^{'}$	Fluctuating velocity in the x-direction	m/s
u^+	Dimensionless velocity	$-$
u_r	Frictional velocity	m/s
V	Mean velocity in the y-direction	m/s
v	Velocity in the y-direction	m/s
$v^{'}$	Fluctuating velocity in the y-direction	m/s
W	Mean velocity in the z-direction	m/s
w	Velocity in the z-direction	m/s
$w^{'}$	Fluctuating velocity in the z-direction	m/s
x	x-direction	m
y	y-direction	m
y_{cl}	The height of the cells in the layer furthest from the wall (in the viscous mesh)	m
y_d	Distance normal from the wall	m
z	z-direction	m

List of Symbols (continuing)

Greek letters

Symbol	**Description**	**Unit**
β	Constant of Equation (2.13)	–
β_1	Constant given by Equation (2.18)	–
β_2	Constant given by Equation (2.18)	–
β^*	Constant given by Equation (2.18)	–
γ_1	Constant given by Equation (2.18)	–
γ_2	Constant given by Equation (2.18)	–
γ_2	Constant of Equation (2.13)	–
δ_{ij}	Kronecker delta	–
δ_{std}	Standard deviation	–
κ	von Kármáns constant, equal to 0.41	–
μ	Dynamic viscosity	$\mathrm{Pa} \cdot \mathrm{s}$
μ_t	Eddy viscosity	$\mathrm{Pa} \cdot \mathrm{s}$
ρ	Density	$\mathrm{kg/m^3}$
σ_k	Constant of Equation (2.12) equal to 0.5	–
σ_ω	Constant of Equation (2.13) equal to 0.5	–
$\sigma_{\omega 2}$	Constant of Equation (2.13) equal to 0.856	–
τ	Shear stress at wall	$\mathrm{N/m^2}$
τ_{xx}	Reynolds normal stress at the surface normal to the x-direction	$\mathrm{N/m^2}$
τ_{xy}	Reynolds shear stress at the surface normal to the x direction in y-direction	$\mathrm{N/m^2}$
τ_{xz}	Reynolds shear stress at the surface normal to the x-direction in z-direction	$\mathrm{N/m^2}$
τ_{yy}	Reynolds normal stress at the surface normal to the y-direction	$\mathrm{N/m^2}$
τ_{yx}	Reynolds shear stress at the surface normal to the y-direction in x-direction	$\mathrm{N/m^2}$
τ_{yz}	Reynolds normal stress at the surface normal to the y-direction in z-direction	$\mathrm{N/m^2}$
τ_{zz}	Reynolds normal stress at the surface normal to the z-direction	$\mathrm{N/m^2}$
τ_{zx}	Reynolds shear stress at the surface normal to the z-direction in the x-direction	$\mathrm{N/m^2}$
τ_{zy}	Reynolds shear stress at the surface normal to the z-direction in the y-direction	$\mathrm{N/m^2}$
ϕ	Constant of Equation (2.14)	–
ϕ_1	Constant of Equation (2.14)	–
ϕ_2	Constant of Equation (2.14)	–
ω	Rate of dissipation of k	$\mathrm{s^{-1}}$

Abbreviations

CAD	Computer-Assisted Drawing
CFD	Computational Fluid Dynamics
DES	Detached Eddy Simulation
LES	Large Eddy Simulation
NTNU	Norwegian University of Science and Technology
SIMPLE	Semi-Implicit Method for Pressure Linked Equations
RANS	Reynolds-averaging Navier-Stokes
SST	Shear Stress Transport
UCI	International Cycling Union
UIS	University of Stavanger
URANS	Unsteady Reynolds-Averaged Navier-Stokes

Chapter 1

Introduction

As the level of competition in sports is ever increasing, with milliseconds separating the first and second place, close attention to detail might be the difference between winning and losing. While a scientific approach to increasing sports performance through optimisation of diet and training is second nature for many top-level athletes, a similar approach to aerodynamics is less common. Great development has been made in cyclic science in recent years. Studies have been performed on bicycle performance (Chowdhury, Alam & Khan, 2011; Barry, Burton, Sheridan, Thompson & Brown, 2014; Lukes, Chin & Haake, 2005), cyclist's posture (Grappe, Candau, Belli & Rouillon, 1997; Jeukendrup & Martin 2001; García-López, Rodríguez-Marroyo, Juneau, Peleteiro, Martínez & Villa, 2008), race clothing (Oggiano, Troynikov, Konopov, Subic & Alam, 2009; Chowdhury, Alam & Subic, 2010) and the shape of the cyclist's helmet (Alam, Chowdhury, Wei, Mustary & Zimmer, 2014; Mustary, Chowdhury, Loganathan, Alharthi & Alam, 2014; Chabroux, V., Barelle, C. & Favier, D., 2008; Brownlie, Ostafichuk, Tews, Muller, Briggs & Franks, 2010). The posture of a cyclist has a large influence on the drag, and by optimising the posture, a significant reduction in drag can be expected. The drag of a cyclist for different postures can be found through experiments using a wind-tunnel or time-trials. However, as these experiments are generally costly and time-consuming, other methods are sought. By the use of 3D scanning and computational fluid dynamics (CFD), the drag for a specific posture can be predicted. However, as 3D scanning is associated with the same challenges as wind-tunnel experiments, in addition to being error-prone, a more efficient procedure is sought.

1.1 Objective and Scope

The objective of this research is to identify the trends associated with posture and drag force for a given cyclist using CFD. These trends should indicate what type of postures that are worth testing in either wind-tunnel or time-trial experiments, with the eventual goal of obtaining the optimal posture.

The scope of this thesis is to develop a procedure for optimising the posture of a cyclist using CFD and execute it. By one 3D scanning of the cyclist, its model is obtained, and further modified using skeleton rigging. Modification of the cyclist's posture is limited to the distance between elbows, elbow extension, and the distance between hands.

1.2 Thesis outline

In Chapter 2, the central theory used in this thesis is presented, i.e. the theory of fluid flow, CFD, boundary conditions and kinematics. In Chapter 3, the simulation of flow over a sphere is presented and results compared with the literature. In Chapter 4, simulations of flow over a cyclist are presented and results compared with the literature. In Chapter 5, the method of skeleton rigging is validated, and a parameter study of cyclist posture is presented. In Chapter 6, the conclusions and recommendations are presented. The references are presented after Chapter 6 and after that the appendix.

Chapter 2

Theory

The central theory used to solve the problems involved in this thesis are presented in this chapter, starting with fluid flow, followed by, computational fluid dynamics, boundary conditions, and ending with kinematics.

2.1 Fluid flow

When a fluid is at rest, it exerts a normal force upon every surface that it is in contact with, which, in terms of fluid mechanics, is known as pressure. When an object has non-zero relative motion, i.e. velocity, to the surrounding fluids, the fluid exerts a non-uniform pressure force and a viscous shear force upon the surface area of the object (which is in contact with the fluid), these forces are known as the drag force. It is often useful to make the effect of the drag force dimensionless, which can be done by calculating the drag coefficient (White, 2011, p. 317)

$$C_D = \frac{2F_D}{\rho U_\infty^2 A} \tag{2.1}$$

where F_D is the drag force, ρ is the density of the surrounding fluid, U_∞ is the free stream (relative) velocity of the fluid (to the object), and A is the surface area facing the direction of relative motion, also known as the frontal area.

The drag force exerted on an object can be found using CFD, which requires a mathematical description of the fluid flow. Through everyday observations, the behaviour of fluid has been known to change with increasing velocity. From a scientific point of view, the fluid behaviour changes with increasing value of the Reynolds number, Re, a dimensionless quantity which describes the relationship between the inertial forces to viscous forces, which can be calculated by (White, 2011, p. 27)

$$Re = \frac{U_\infty L \rho}{\mu} \tag{2.2}$$

where U_∞ is freestream velocity, L is characteristic length scale which for a sphere is its diameter, and μ is the fluids dynamic viscosity.

The Reynolds number is used to predict the behaviour of the fluid to be either laminar, turbulent or in a transition between them. At low Reynolds numbers, the flow is laminar. Thus, the flow is smooth and neighbouring layers of fluid slide past each other in an orderly fashion. At high Reynolds numbers, the flow is turbulent. Thus, the flow behaviour is rapidly fluctuating in time and space (Versteeg & Malalasekera, 2007, p. 41). Transition flows have a combination of these characteristics. The relationship between the Reynolds number and drag coefficient for a sphere with corresponding flow regimes are presented in Figure 2.1. As seen in this figure, the drag crisis occurs in the critical flow regime. The drag crisis is because of the transition from laminar to turbulent boundary layer, as the

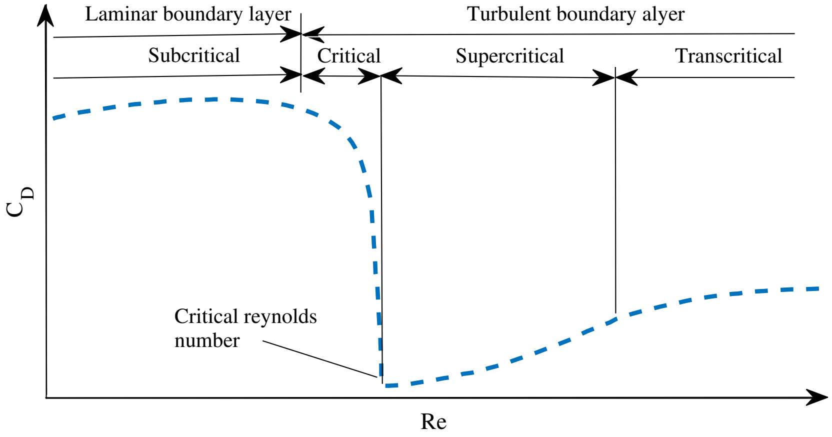

Figure 2.1: Relationship between the Reynolds number and drag coefficient for sphere with corresponding flow regimes

latter is more resistant to flow separation than a laminar boundary layer is, the turbulent boundary layer remains attached to the sphere surface for a longer distance around the sphere. Hence, the wake is much narrower with a corresponding lower drag.

Most flows in engineering applications of CFD, including this projects, experience a turbulent flow (Versteeg & Malalasekera, 2007, p. 40). If turbulence is present, the mathematical description of the fluid flow must take into account the effect of turbulence. In this thesis, this is done by the method of Reynolds-Averaging. This method describes the effect of turbulence, i.e. random fluctuations, on the mean flow, by decomposing the flow properties, i.e. velocities and pressure, to a sum of the mean and fluctuating component (Versteeg & Malalasekera, 2007, p. 63)

$$u = U + u',\ v = V + v'\ , w = W + w',\ p = P + p' \tag{2.3}$$

where u, v and w is the velocity in the x-,y- and z-direction, p is the pressure, capital letter denotes the mean value component, and $'$ denotes the fluctuating component.

By considering the conservation laws of mass, momentum and energy, we can establish the mathematical representation of fluid flow. These equations are physically and mathematically complex, and by the use of appropriate hypothesis, idealisations and simplifications, their complexity can be reduced and solved numerically. The Navier-Stokes equations can describe the governing equations for an (assumed to be) incompressible flow, and by introducing the effects of turbulence through Reynolds-Averaging, the governing equations of the flows solved in this project becomes the Reynolds-Averaged Navier-Stokes (RANS) equations (Versteeg & Malalasekera, 2007, pp. 63-64)

$$\text{div}\ \mathbf{U} = 0 \tag{2.4}$$

$$\frac{\partial U}{\partial t} + \text{div}(U\mathbf{U}) = -\frac{1}{\rho}\frac{\partial P}{\partial x} + \nu\ \text{div}(\text{grad}(U)) + \frac{1}{\rho}\Big[\frac{\partial}{\partial x}(-\rho\overline{u'^2}) + \frac{\partial}{\partial y}(-\rho\overline{u'v'}) + \frac{\partial}{\partial z}(-\rho\overline{u'w'})\Big] \tag{2.5}$$

$$\frac{\partial V}{\partial t} + \text{div}(V\mathbf{U}) = -\frac{1}{\rho}\frac{\partial P}{\partial y} + \nu\ \text{div}(\text{grad}(V)) + \frac{1}{\rho}\Big[\frac{\partial}{\partial x}(-\rho\overline{u'v'}) + \frac{\partial}{\partial y}(-\rho\overline{v'^2}) + \frac{\partial}{\partial z}(-\rho\overline{v'w'})\Big] \tag{2.6}$$

$$\frac{\partial W}{\partial t} + \text{div}(W\mathbf{U}) = -\frac{1}{\rho}\frac{\partial P}{\partial z} + \nu\ \text{div}(\text{grad}(W)) + \frac{1}{\rho}\Big[\frac{\partial}{\partial x}(-\rho\overline{u'w'}) + \frac{\partial}{\partial y}(-\rho\overline{v'w'}) + \frac{\partial}{\partial z}(-\rho\overline{w'^2})\Big] \tag{2.7}$$

where

- div denotes divergence, and div $\mathbf{U}$ is the volumetric deformation, given by

$$\frac{\partial U}{\partial x} + \frac{\partial V}{\partial y} + \frac{\partial W}{\partial z}$$

- t is the time
- grad denotes gradient
- ν is the kinematic viscocity
- $\overline{u'}$, $\overline{v'}$ and $\overline{w'}$ is the time averaged value of the fluctuating velocity components in the x-, y- and z-direction

The terms involving the time-averaged products of the fluctuating velocity components in the Equation 2.5-2.7 are often expressed in terms of the six Reynolds stresses (Versteeg & Malalasekera, 2007, p. 64), which consists of three normal stresses

$$\tau_{xx} = -\rho\overline{u'^2},\ \tau_{yy} = -\rho\overline{v'^2},\ \tau_{zz} = -\rho\overline{w'^2} \tag{2.8}$$

and three shear stresses

$$\tau_{xy} = \tau_{yx} = -\rho\overline{u'v'},\ \tau_{yz} = \tau_{zy} = -\rho\overline{v'w'},\ \tau_{xz} = \tau_{zx} = -\rho\overline{u'w'} \tag{2.9}$$

assuming an isotropic fluid. The Reynolds stresses are a direct consequence of the decomposition of the flow properties, and a turbulence model is required to calculate them. There exists a wide range of turbulence models. However, there exists no complete turbulence model that is applicable for every type of flow. Therefore, the turbulence model which is best suited for the specific problem should be chosen. The shear stress transport(SST) $k-\omega$ model combines the strengths of traditional $k-\varepsilon$ and $k-\omega$ models. It can be considered a hybrid model, by utilising the $k-\varepsilon$ in the free stream far away from walls, and the $k-\omega$ in the near-wall region (Versteeg & Malalasekera, 2007, p. 91). This model is often considered to be the default model for general purpose CFD, and Versteeg & Malalasekera (2007, p. 92) claims that the $SST\ k-\omega$ model is a suitable and the most general, turbulence model for simulation of external dynamics. External dynamics is a term defined as fluid flow around a body that is completely submerged in the fluid. Hence, the SST $k-\omega$ turbulence model is used in this thesis.

By adopting the so-called suffix notation, where i and j denotes either the x-, y and z-direction. The chosen turbulence model calculates the Reynolds stresses by

$$\tau_{ij} = -\rho\overline{u_i'u_j'} = \mu_t\Big(\frac{\partial U_i}{\partial x_j} + \frac{\partial U_j}{\partial x_i}\Big) - \frac{2}{3}\rho k\delta_{ij} \tag{2.10}$$

where

- μ_t is the eddy viscosity, which remains unknown until the transport equations for turbulence are introduced
- k is the turbulent kinetic energy, given by

$$k = \frac{1}{2}(\overline{u'^2} + \overline{v'^2} + \overline{w'^2}) \tag{2.11}$$

- δ is the Kronecker delta which is equal to 1 if $i = j$ and otherwise 0

The model introduces two additional transport equations, i.e. two transport equations for turbulence, one for k

$$\frac{\partial(\rho k)}{\partial t} + \frac{\partial(\rho u_j k)}{\partial x_j} = \tau_{ij}\frac{\partial u_i}{\partial x_j} - \beta^* \rho \omega k + \frac{\partial}{\partial x_j}\Big[(\mu + \sigma_k \mu_t)\frac{\partial k}{\partial x_j}\Big] \tag{2.12}$$

and one for ω, which is the rate of dissipation of the turbulent kinetic energy

$$\begin{aligned}\frac{\partial(\rho \omega)}{\partial t} + \frac{\partial(\rho u_j \omega)}{\partial x_j} = \frac{\gamma\rho}{\mu_t}\tau_{ij}\frac{\partial u_i}{\partial x_j} - \beta\rho\omega^2 + \frac{\partial}{\partial x_j}\Big[(\mu + \sigma_\omega \mu_t)\frac{\partial \omega}{\partial x_j}\Big] \\ +2(1-F_1)\frac{\rho\sigma_{\omega 2}}{\omega}\frac{\partial k}{\partial x_j}\frac{\partial \omega}{\partial x_j}\end{aligned} \tag{2.13}$$

where

$$\mu_t = \frac{\rho k}{\omega}$$

and each of the constants is a blend of an inner ϕ_1 and an outer ϕ_2 constant, blended by

$$\phi = F_1\phi_1 + (1-F_1)\phi_2 \tag{2.14}$$

additional functions are given by

$$F_1 = tanh(arg_1^4) \tag{2.15}$$

$$arg_1 = min\Big[max\Big(\frac{\sqrt{k}}{\beta^*\omega d}, \frac{500\nu}{d^2\omega}\Big), \frac{4\rho\sigma_{\omega 2}k}{CD_{k\omega}d^2}\Big] \tag{2.16}$$

$$CD_{k\omega} = max\Big(2\rho\sigma_{\omega 2}\frac{1}{\omega}\frac{\partial k}{\partial x_j}\frac{\partial \omega}{\partial x_j}, 10^{-20}\Big) \tag{2.17}$$

and the remaining constants are given by

$$\begin{aligned}\gamma_1 = \frac{\beta_1}{\beta^*} - \frac{\sigma_{\omega 1}\kappa^2}{\sqrt{\beta^*}},\ \gamma_2 = \frac{\beta_2}{\beta^*} - \frac{\sigma_{\omega 2}\kappa^2}{\sqrt{\beta^*}},\ \sigma_k = 0.5,\ \sigma_\omega = 0.5,\ \sigma_{\omega 2} = 0.856, \\ \beta_1 = 0.075,\ \beta_2 = 0.0828,\ \beta^* = 0.09,\ \kappa = 0.41\end{aligned} \tag{2.18}$$

2.2 Computational fluid dynamics

Computational fluid dynamics(CFD) is a branch of fluid dynamics which solves problems involving fluid flow by the use of numerical analysis. It has a great practical application on engineering problems and is in this project used to analyse the aerodynamics of a sphere and a cyclist. In this thesis, the open-source CFD software OpenFOAM is used. The execution of a CFD analysis is a procedure generally divided into three steps, which has the following functions:

- Pre-processor: The function of the pre-processor is to define the physical problem that is to be solved. Thus, geometry has to be defined, and this geometry should further be meshed, physical or chemical phenomena that are to be modelled selected, fluid properties defined, and finally, boundary conditions set.
- Solver: The function of the solver is mainly to solve the problem defined in the pre-processor, by numerical calculation. There are many approaches to this. However, we concentrate on the method used in this project, the finite volume method, which is a special formulation of the finite difference method (Versteeg & Malalasekera, 2007, p. 3). The governing equations of an incompressible fluid flow consist of partial differential equations, which are extremely hard to solve analytically for complex problems. Thus, the equations are solved numerically using the finite volume method, which is a special finite difference formulation that is central to the most well-established CFD codes (Versteeg & Malalasekera, 2007, p. 3). The steps of the algorithm are

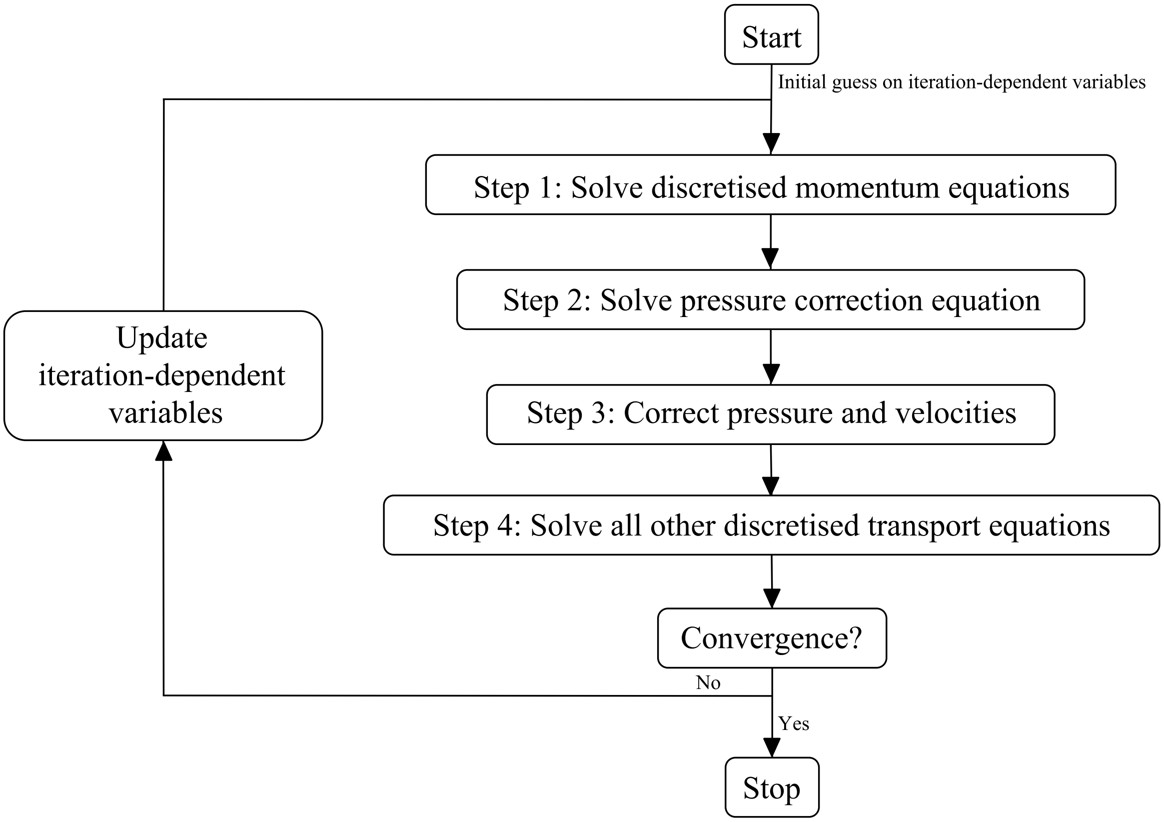

Figure 2.2: The steps of the SIMPLE algorithm, which is used in the *simpleFoam* solver.

1. Integrate the governing equations over the finite number of control volumes
2. Discretise the resulting integral equations into a system of algebraic equations
3. Solve the system of algebraic equations by an iterative method.

To solve the discretised governing equations, i.e. the algebraic equations, of a fluid problem using OpenFOAM, a solver must be chosen based on the characteristics of the problem. Since our problem is a steady-state simulation of an incompressible Newtonian fluid which experiences turbulence, by (OpenFOAM a, n.d.), our obvious choice is a solver known as *simpleFoam.* This solver uses an algorithm known as ”semi-implicit method for pressure linked equations” (SIMPLE) to solve the algebraic equations. The steps of this algorithm are presented and illustrated in Figure 2.2, and for more information about the algorithm the reader is referred to Versteeg & Malalasekera (2007, p. 186).

- Post-processor: Finally, the function of the post-processor is to evaluate the results given by the solver, which are presented in the form of numerical values. Hence, to gain a better understanding and overview of these values, the common practice is to plot them, or if the transient solution is of interest, animate them.

2.3 Boundary conditions

Turbulence can be present anywhere in a flow, however, since our main interest is the drag, we are particularly interested in the turbulence that occurs close to walls. Appropriate boundary conditions have to be defined to model this type of turbulence correctly. By considering the no-slip condition, which is that a fluid that is in contact with an object, usually referred to as a wall, always has zero relative velocity, thus, by equation 2.2 the Reynolds number is 0, and the viscous forces dominate the inertial forces. Hence, the flow near the wall is influenced by viscous effects, not the free stream parameters (Versteeg & Malalasekera, 2007, p. 57), and its mean velocity is a function f of

$$U = f(y_d, \rho, \mu, \tau_w) \tag{2.19}$$

where y_d is the distance from the wall and τ_w is the shear stress at the wall.

Dimensional analysis shows that (Versteeg & Malalasekera, 2007, p. 57)

$$u^+ = \frac{U}{u_\tau} = f\Big(\frac{\rho u_\tau y_d}{\mu}\Big) = f(y^+) \tag{2.20}$$

where u^+ is the dimensionless velocity, u_τ is the frictional velocity, and y^+ is the dimensionless distance from the wall.

Equation 2.20 is known as the law of the wall, first published by Theodore von Kármán in 1931 (von Kármán, 1931), based on the work of Ludwig Prandtl on turbulence near walls. The characteristic plot of u^+ as a function of y^+ is plotted in Figure 2.3, which introduces three different layers, i.e.

- viscous sub-layer, $0 \leq y^+ < 5$, where
  $$u^+ = y^+ \tag{2.21}$$
- buffer layer, $5 \leq y^+ < 30$
- log-law layer, $30 \leq y^+ < 500$, where
  $$u^+ = \kappa^{-1}\ln(Ey^+) \tag{2.22}$$
  where κ is the von Kármáns constant, equal to 0.4, and E is also a constant, equal to 9.8.

To capture the effects of the law of the wall, a particularly fine mesh along the boundaries of walls are needed, which can be achieved by utilising a viscous mesh, as illustrated in Figure 2.4. To determine the parameters of the viscous mesh, we consider the turbulent boundary conditions of the chosen turbulence model, which are to be specified at the following locations

- inlet; distributions of k and ω must be specified, and they can be approximated by (OpenFOAM b, n.d.)
  $$k = \frac{3}{2}(U_\infty T_i)^2 \tag{2.23}$$
  $$\omega = \frac{\sqrt{k}}{C_\mu L} \tag{2.24}$$
  where T_i is the turbulence intensity, C_μ is a constant equal to 0.09, and L is the characteristic length scale, which in the case of a sphere is equal to its diameter.
- outlet; (Versteeg & Malalasekera, 2007, p. 76)
  $$\frac{\partial k}{\partial n} = 0, \ \frac{\partial \omega}{\partial n} = 0 \tag{2.25}$$
  where n is the direction normal to the boundary.

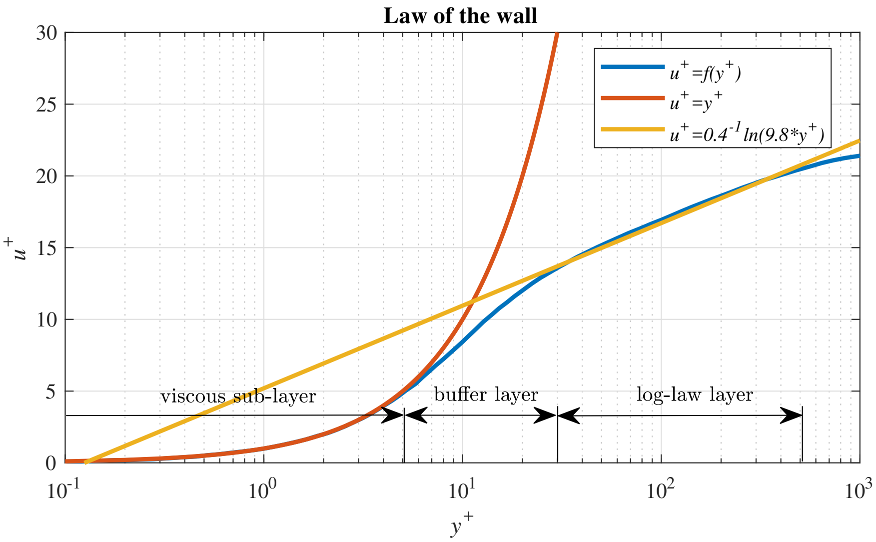

Figure 2.3: The law of the wall and three corresponding layers

- free stream; k and ω must be specified, or Equation 2.25 must be satisfied in the free stream (Versteeg & Malalasekera, 2007, p. 76). According to Robertson (2015, p. 80) they can be specified by

$$k = 10^{-6} \tag{2.26}$$

$$\omega = \frac{5U_\infty}{L} \tag{2.27}$$

- solid walls; which according to Robertson (2015, p.80) can be specified by

$$k = 0 \tag{2.28}$$

$$\omega = \frac{60\nu}{\beta_1 y_{dc}^2} \tag{2.29}$$

  where β_1 is a constant equal to 0.075, and y_{dc} is the height of the first cell from the wall.

By Equation 2.29 and setting $y = y_{dc}$, the effects of turbulence are related to one of the parameters of the viscous mesh, i.e. y, which can be calculated by

$$y = y_{dc} = \frac{y^+\mu}{u_\tau \rho} \tag{2.30}$$

where y^+ is the dimension-less wall distance, ideally equal to one on the surface of the wall, hence set equal to one in the calculation of y, and u_τ is given by (Ertesvåg, 2000, p. 67)

$$u_\tau = \sqrt{\frac{\tau_w}{\rho}} \tag{2.31}$$

where τ_w is the shear stress along the wall, given by (White, 2011, p. 480)

$$\tau_w = \frac{C_f \rho U_\infty^2}{2} \tag{2.32}$$

where C_f is the friction variation given by (White, 2011, p. 473)

$$C_f = \frac{0.027}{Re^{1/7}} \tag{2.33}$$

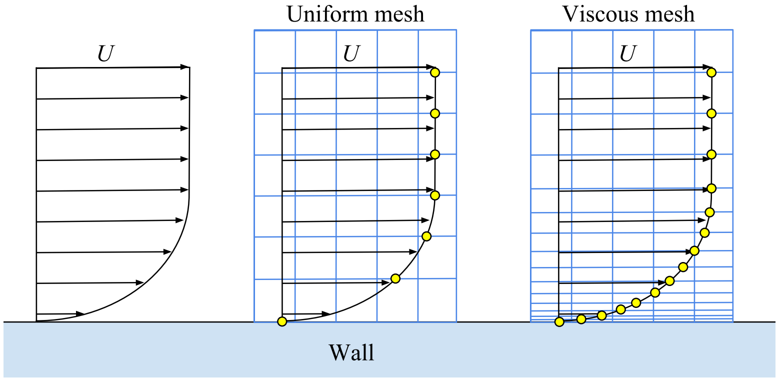

Figure 2.4: Velocity profile for a fluid in contact with a wall, illustrated separately, in an uniform mesh, and in a viscous mesh. As illustrated, it becomes clear that a uniform mesh is unable to capture the rapid change in velocity towards the wall. Assuming that the uniform mesh is not so fine that it is able, which normally is not the case. Hence a viscous mesh is needed.

Thus, by substituting Equation 2.33 into 2.32

$$\tau_w = 0.0135\frac{\rho U_\infty^2}{Re^{1/7}} \tag{2.34}$$

the resulting expression into Equation 2.31

$$u_\tau = \sqrt{\frac{0.0135 U_\infty^2}{Re^{1/7}}} \tag{2.35}$$

and, once more, the resulting expression into Equation 2.30, a more useful form of the latter equation is obtained, and we finally obtain an expression for calculating y_{dc}

$$y_{dc} = \frac{1}{\sqrt{0.0135}}\frac{y^+ Re^{1/14}\mu}{U_\infty \rho} \tag{2.36}$$

In addition to y_{dc}, the viscous mesh has several other important parameters worthy of a discussion, which are the

- Expansion ratio e_{ra}, i.e. the increase in the height of neighbouring cells, wherein the cells closer to the wall has a lower height compared to the cells further from the wall. Typically, its set equal to 1.2, as is the case in this thesis
- Total height of viscous mesh h_T. At some point the viscous mesh intersects with a uniform background mesh, this distance from the wall is the total height of the viscous mesh, and by considering a fixed e_{ra} and y^+, and hence y_{dc}, the number of cell layers is its only parameter
- Number of cell layers n_{ce} is the number of cell layers in the viscous mesh. By keeping the previously mentioned parameters fixed, n_{ce} should have a numerical value that makes the height of the cell furthest from the wall approximately equal to the height of the cells in the background mesh. Thus, enabling a smooth mesh-vice transition between the viscous mesh and the uniform background mesh. This value can be calculated by

  $$n_{ce} = \frac{\ln y_{cl} - \ln y_{dc}}{\ln e_{ra}} \tag{2.37}$$

  where y_{cl} is the height of cells in the layer furthest from the wall (in the viscous mesh), which should be set equal to he height of the cells in the background mesh, once again, to ensure an

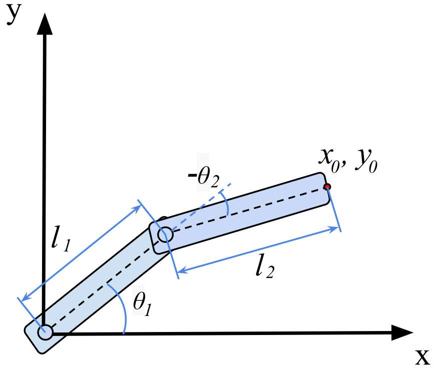

Figure 2.5: Robot arm consisting of two bodies connected to each other and the ground by revolute joints

appropriate mesh transition. The observant reader will notice that this equation can return a non-integer n_ce, thus, n_{ce} should be rounded downwards to the nearest integer, as this would make y_{cl} a bit smaller than those of the background mesh.

To summarise, to ensure a mesh which has sufficient fineness to include the effects of the law of the wall the following guidelines are given on the most important parameters of the mesh

- y^+, ideally set equal to one
- y_{dc}, calculate by Equation 2.36
- e_{ra}, set equal to 1.2
- h_T, indirectly determined by the other parameters
- n_{ce}, calculate by Equation 2.37

Certain mesh generators struggles with generating cell layers for complex geometries with normal sized h_T, thus, the n_{cl} is often reduced from the value calculated by Equation 2.37, as this is known to simplify the process of cell layer generation, however, at the cost of optimal mesh transition.

2.4 Kinematics

Kinematics is mathematical description of motion without considering the physical forces needed to perform the movement. Kinematics is used in this project to change the posture of the cyclist, by the principle of inverse kinematics, which is the same principle as for inverse mathematics, you know the answer but you do not know how to calculate it. Consider the robot arm consisting of two revolute joints presented in figure 2.5. Let us assume that the tool-tip position, i.e. the red circle in Figure 2.5, of the robot is a known position (x_0, y_0). However, we do not know the joint angles θ_a and θ_b. By the principle of inverse kinematics, these angles can be calculated for any tool-tip position.

The tooltip position of the robot is given by

$$x = l_1\text{cos}(\theta_1) + l_2\text{cos}(\theta_1 + \theta_2) \tag{2.38}$$

$$y = l_1\text{sin}(\theta_1) + l_2\text{sin}(\theta_1 + \theta_2) \tag{2.39}$$

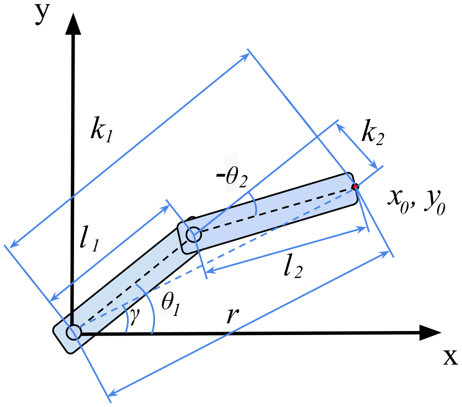

Figure 2.6: Figure 2.5 with additional definitions needed to find the equation for θ_1

which is known as the forward kinematics. Now we start our work on deriving the inverse kinematics, i.e. explicit equations for θ_1 and θ_2. First, we square and sum Equation 2.38 and 2.39, which gives us

$$\begin{aligned} x^2 + y^2 &= l_1^2\cos^2(\theta_1) + l_2^2\cos^2(\theta_1 + \theta_2) + 2l_1l_2\cos(\theta_1)\cos(\theta_1 + \theta_2) + l_1^2\sin^2(\theta_1) \\ &\quad + l_2^2\sin^2(\theta_1 + \theta_2) + 2l_1l_2\sin(\theta_1)\sin(\theta_1 + \theta_2) \\ &= l_1^2 + l_2^2 + 2l_1l_2[\cos(\theta_1)\cos(\theta_1 + \theta_2 + \sin(\theta_1)\sin(\theta_1 + \theta_2)] \end{aligned} \tag{2.40}$$

Next, consider the trigonometric identities

$$\sin(x \pm y) = \sin(x)\cos(y) \pm \cos(x)\sin(y) \tag{2.41}$$

$$\cos(x \pm y) = \cos(x)\cos(y) \pm \sin(x)\sin(y) \tag{2.42}$$

By applying these on Equation 2.40, it can be rewritten as

$$\begin{aligned} x^2 + y^2 &= l_1^2 + l_2^2 + 2l_1l_2[\cos(\theta_1)(\cos(\theta_1)\cos(\theta_2) - \sin(\theta_1)\sin(\theta_2)) \\ &\quad + \sin(\theta_1)(\sin(\theta_1)\cos(\theta_2) - \cos(\theta_1)\sin(\theta_2))] \\ &= l_1^2 + l_2^2 + 2l_1l_2[\cos^2(\theta_1)\cos(\theta_2) + \sin^2(\theta_2)\cos(\theta_2)] \\ &= l_1^2 + l_2^2 + 2l_1l_2\cos(\theta_2) \end{aligned} \tag{2.43}$$

Next, we can use Equation 2.44 to express θ_2 explicit

$$cos(\theta_2) = \frac{x^2 + y^2 - l_1^2 - l_2^2}{2l_1l_2} \tag{2.44}$$

$$\Rightarrow \theta_2 = \cos^{-1}(\frac{x^2 + y^2 - l_1^2 - l_2^2}{2l_1l_2}) \tag{2.45}$$

Our first step in finding the equation for θ_1 is to rewrite the forward kinematics equations with the basis of the definitions presented in Figure 2.6.

$$x = k_1\cos(\theta_1) - k_2\sin(\theta_1) \tag{2.46}$$

$$y = k_1\sin(\theta_1) + k_2\cos(\theta_1) where \tag{2.47}$$

where

$$k_1 = l_1 + l_2\cos(\theta_2) \tag{2.48}$$

$$k_2 = l_2\sin(\theta_2) \tag{2.49}$$

Further, we write

$$r = \sqrt{k_1^2 + k_2^2} \tag{2.50}$$

$$\gamma = atan2(k_2, k_1) \tag{2.51}$$

$$k_1 = r\cos\gamma \tag{2.52}$$

$$k_2 = r\sin\gamma \tag{2.53}$$

where $atan2$ is the four-quadrant inverse tangent of a coordinate. Based on the coordinate, the angle α between the coordinate and the positive defined horizontal axis within in the interval $-\pi < \alpha < \pi$ is returned. As opposed to the traditional $atan$, which returns an angle α in the interval $-\pi/2 < \alpha < \pi/2$.

Inserting Equation 2.52 and 2.53 into Equation 2.46 and 2.47 yields

$$\begin{aligned} x &= r\cos(\gamma)\cos(\theta_1) - r\sin(\gamma)\sin(\theta_1) && (2.54)\\ \Rightarrow \frac{x}{r} &= \cos(\gamma)\cos(\theta_1) - \sin(\gamma)\sin(\theta_1) \\ &= \cos(\gamma + \theta_1) && (2.55) \end{aligned}$$

$$\begin{aligned} y &= r\cos(\gamma)\sin(\theta_1) + r\sin(\gamma)\cos(\theta_1) && (2.56)\\ \Rightarrow \frac{y}{r} &= \cos(\gamma)\sin(\theta_1) + \sin(\gamma)\cos(\theta_1) \\ &= \sin(\gamma + \theta_1) && (2.57) \end{aligned}$$

Finally, applying the atan2 function

$$\begin{aligned} \gamma + \theta_1 \text{atan2}(\frac{y}{r}, \frac{y}{r}) &= \text{atan2}(y, x) && (2.58)\\ \Rightarrow \theta_1 &= \text{atan2}(y, x) - \text{atan2}(k_2, k_1) && (2.59) \end{aligned}$$

where

$$k_1 = l_1 + l_2\cos(\theta_2) \tag{2.60}$$

$$k_2 = l_2\sin(\theta_2) \tag{2.61}$$

The software used in this project for adjusting the cyclist posture, which is Blender, uses inverse kinematics to calculate corresponding joint angles between limbs when for example a hand is moved. The calculation is embedded in the software.

Chapter 3

Simulation of flow over a sphere

As part of the process of developing the computational setup, it was tested on a simpler geometry, for which information about physical experiments is available. Simulation of flow around a sphere challenges the computational setup, as well as being modelling-wise a simple geometry, with several publications on both physical experiments and numerical studies available. In this thesis, the sphere is simulated for Reynolds number equal to 10^4 and 10^6. By Equation 2.2, these Reynolds numbers corresponds to velocities of 0.15 and 15 m/s, where the latter is roughly the typical velocity for a professional cyclist by assuming the properties of air to be ρ=1 kg/m^3 and μ=1.5$\cdot$10^{-5} Pa$\cdot$s and L=1 m.

Research has been carried out on the flow around a sphere for almost a 100 years, with physical experiments of Wieselsberger dating back to 1922. Wieselsberger (1922) measured the drag force from $Re = 10$ through the critical flow regime, i.e. up to $Re = 10^6$, and observed the characteristic drop of C_D in the critical flow regime. The reported results of the drag coefficient at high Reynolds numbers, together with results from the researchers presented in the following, are plotted in Figure 3.1. Milikan & Klein (1933) measured in the range from $Re = 2 \cdot 10^5$ to $Re = 8 \cdot 10^5$, that is into the supercritical regime, and observed the characteristic drop of C_d, similar, although far from identical, to Wieselsberger. Achenbach (1972) extended the measurement range, and measured from $Re = 5 \cdot 10^4$ to $Re = 6 \cdot 10^6$, and obtained results quite similar to Milikan. The results obtained Achenbach are widely cited by later work performed in the recent years, for which the trends have shifted from physical experiments to computational experiments using CFD.

Constantinescu, Chapelet & Squires (2003) studied the turbulence modelling applied to flow over a sphere, and presented numerical simulations of the subcritical flow regime, with the aim of comparing the results from three different approaches to model turbulence; unsteady Reynolds-Averaged Navier-Stokes (URANS), detached eddy simulation(DES) and large eddy simulation (LES). They concluded that the URANS predictions, with $k-\omega$ turbulence modelling, of the pressure coefficient, skin friction, and (by association) the streamwise drag, were in reasonable agreement with measurements. Constantinescu & Squires (2004) performed a numerical investigation of flow over a sphere in the subcritical and supercritical regimes using DES simulations and were able to capture many of the features that characterise the subcritical and supercritical regimes, as revealed by experimental investigations. Jones & Clarke (2008) simulated the flow past a sphere using the commercial CFD Fluent code in multiple flow regimes and confirmed that the capabilities of Fluent to accurately reproduce typical flow structures observed for both time-independent/time-dependent and laminar/turbulent flow regimes.

3.1 Computational setup

The sphere, which has a diameter of 1 *m*, is modelled in a computer-assisted drawing (CAD) program, saved in STL file format, and imported and meshed in OpenFOAM using the two utilities; blockMesh

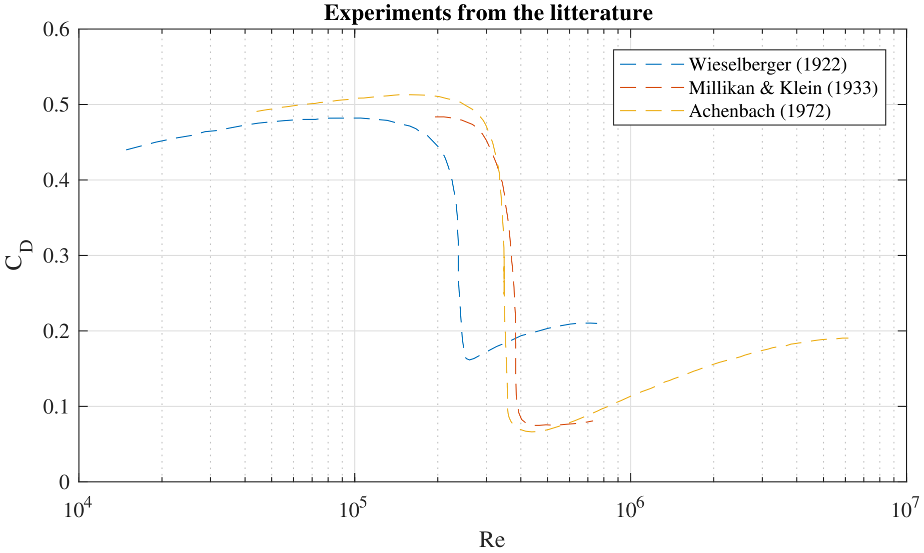

Figure 3.1: A comparison of the literature on the (experimental) drag coefficient of the sphere as a function of the Reynolds number

and snappyHexMesh. blockMesh is used to create what is known as the background mesh in the computational domain, while snappyHexMesh refines the mesh around the sphere according to the user's specifications.

The grid is generated based on the recommendations presented in Chapter 2.3, with y^+ set to 1, y is calculated by Equation 2.36, which is

$$y = \frac{1}{\sqrt{0.0135}} \frac{y^+ Re^{1/14} \mu}{U_\infty \rho} = \frac{1}{\sqrt{0.0135}} \frac{1 \cdot Re^{1/14} \cdot 1.5 \cdot 10^{-5} \text{ Pa} \cdot \text{s}}{U_\infty \cdot 1 \text{ kg/m}^3} \tag{3.1}$$

Inserting the Re corresponding to each simulation in the latter equation and the constants for air yields

$$y(Re = 10^4, U_\infty = 0.15 \text{ m/s}) = \frac{1}{\sqrt{0.0135}} \frac{1 \cdot 10^{4 \cdot 1/14} \cdot 1.5 \cdot 10^{-5} \text{ Pa} \cdot \text{s}}{0.15 \text{ m/s} \cdot 1 \text{ kg/m}^3} = 1.7 \cdot 10^{-3} \text{ m} \tag{3.2}$$

$$y(Re = 10^6, U_\infty = 15 \text{ m/s}) = \frac{1}{\sqrt{0.0135}} \frac{1 \cdot 10^{6 \cdot 1/14} \cdot 1.5 \cdot 10^{-5} \text{ Pa} \cdot \text{s}}{15 \text{ m/s} \cdot 1 \text{ kg/m}^3} = 2.4 \cdot 10^{-5} \text{ m} \tag{3.3}$$

Further, n_{ce} is calculated by Equation 2.37, which is

$$n_{ce} = \frac{\ln y_{cl} - \ln y}{\ln e_{ra}} = \frac{\ln y_{cl} - \ln y}{\ln (1.2)} \tag{3.4}$$

y_{cl} is set equal to the uniform grid which is surrounding the sphere, which is treated as a parameter to determine a sufficient grid size. As we will see in the results, a grid consisting of $5.13 \cdot 10^5$ and $6.55 \cdot 10^6$ cells are sufficient to reach convergence with Re equal to 10^4 and 10^6, respectively. These meshes are constructed by setting the sides of the cubic grid cells to be $2.27 \cdot 10^{-2}\ m$ and $6.25 \cdot 10^{-3}\ m$, respectively. Thus, by setting y_{cl} equal to these values, n_{ce} can be calculated for each mesh

$$Re = 10^4, \ \ n_{ce} = \frac{\ln(2.27 \cdot 10^{-2}) - \ln(1.7 \cdot 10^{-3})}{\ln(1.2)} \approx 14 \tag{3.5}$$

$$Re = 10^6,\ n_{ce} = \frac{\ln(6.25 \cdot 10^{-3}) - \ln(2.4 \cdot 10^{-5})}{\ln(1.2)} \approx 30 \tag{3.6}$$

An overview of the meshes used with $Re = 10^4$ and $Re = 10^6$, which had sufficient number of cells, are presented in Figure 3.2 and 3.4, with additional zoom on the viscous mesh in Figure 3.3 and 3.5, respectively.

The fluid flow surrounding the sphere is simulated in steady-state as an incompressible Newtonian turbulent fluid, which by Chapter 2.2 leave us with the obvious solver choice of *simpleFoam*. The governing equations presented in Chapter 2.1 applies to these simulations together with the with the turbulence model $SST\ k - \omega$. The convergence criteria are based on the residuals for pressure and velocity in the x-, y- and z-direction, which are to be smaller than 10^{-5} before the simulation converges. A uniform constant horizontal velocity of 0.15 m/s and 15 m/s and zero gradient for pressure are imposed at the inlet of the fluid domain, which corresponds to the left vertical edge of the meshes presented in Figure 3.2 and 3.4, respectively. At the outlet, i.e. the right vertical edge of the mesh in the two latter figures, a pressure outlet condition with ambient static pressure is imposed. A zero gradient for pressure is imposed on the other sides of the domain, together with slip for velocity. Finally, for the sphere, a no-slip for velocity- and a zero gradient for pressure boundary condition is imposed. Additionally, the turbulent boundary conditions described in Chapter 2.3 are embedded in the software, except for k and ω at the inlet. Their numerical value are approximated by Equation (2.23) and (2.24), which are

$$k = \frac{3}{2}(U_\infty T_i)^2 \tag{3.7}$$

$$\omega = \frac{\sqrt{k}}{C_\mu L} \tag{3.8}$$

Since we are to compare the simulation results with wind tunnel experiments performed in the literature, a low T_i is expected. Hence, it's set equal to 0.5%. As opposed to engineering flows which typically have a T_i between 2 and 5%(Versteeg & Malalasekera, 2007). By inserting the velocity, the corresponding k and ω can be calculated for both simulations

$$k(U_\infty = 0.15\ \mathrm{m/s}) = \frac{3}{2}(U_\infty T_i)^2 = \frac{3}{2}(0.15\ \mathrm{m/s} \cdot 0.005)^2 = 8.4375 \cdot 10^{-7}\ \mathrm{m^2/s^2} \tag{3.9}$$

$$\omega(U_\infty = 0.15\ \mathrm{m/s}) = \frac{\sqrt{k}}{C_\mu L} = \frac{\sqrt{8.4375 \cdot 10^{-7}\ \mathrm{m^2/s^2}}}{0.09 \cdot 1\ \mathrm{m}} \approx 1.0206 \cdot 10^{-2}\ \mathrm{s^{-1}} \tag{3.10}$$

$$k(U_\infty = 15\ \mathrm{m/s}) = \frac{3}{2}(U_\infty T_i)^2 = \frac{3}{2}(15\ \mathrm{m/s} \cdot 0.005)^2 = 8.4375 \cdot 10^{-3}\ \mathrm{m^2/s^2} \tag{3.11}$$

$$\omega(U_\infty = 15\ \mathrm{m/s}) = \frac{\sqrt{k}}{C_\mu L} = \frac{\sqrt{8.4375 \cdot 10^{-3}\ \mathrm{m^2/s^2}}}{0.09 \cdot 1\ \mathrm{m}} \approx 1.0206\ \mathrm{s^{-1}} \tag{3.12}$$

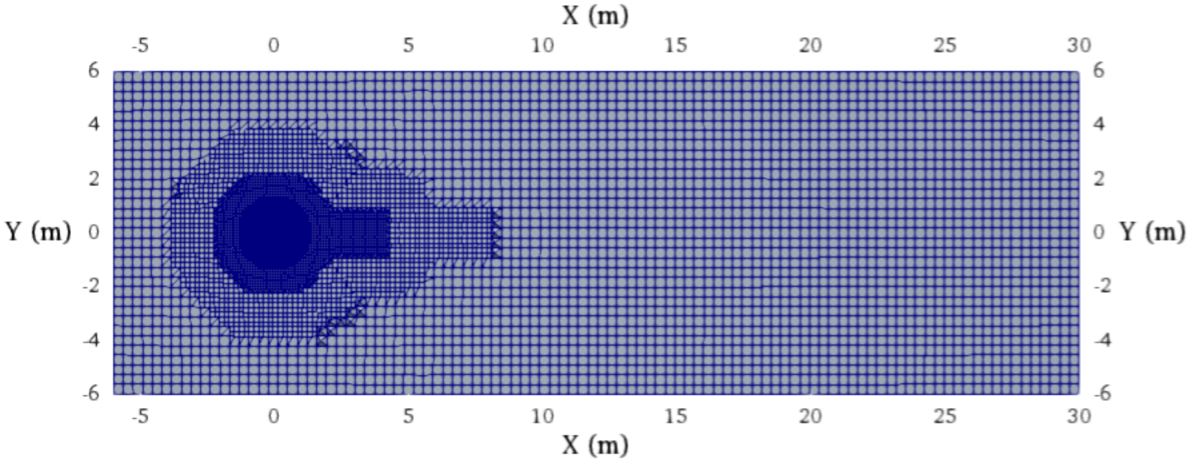

Figure 3.2: Overview of the converging mesh at $Re = 10^4$ in the computational domain, its is refined in areas of particular interest

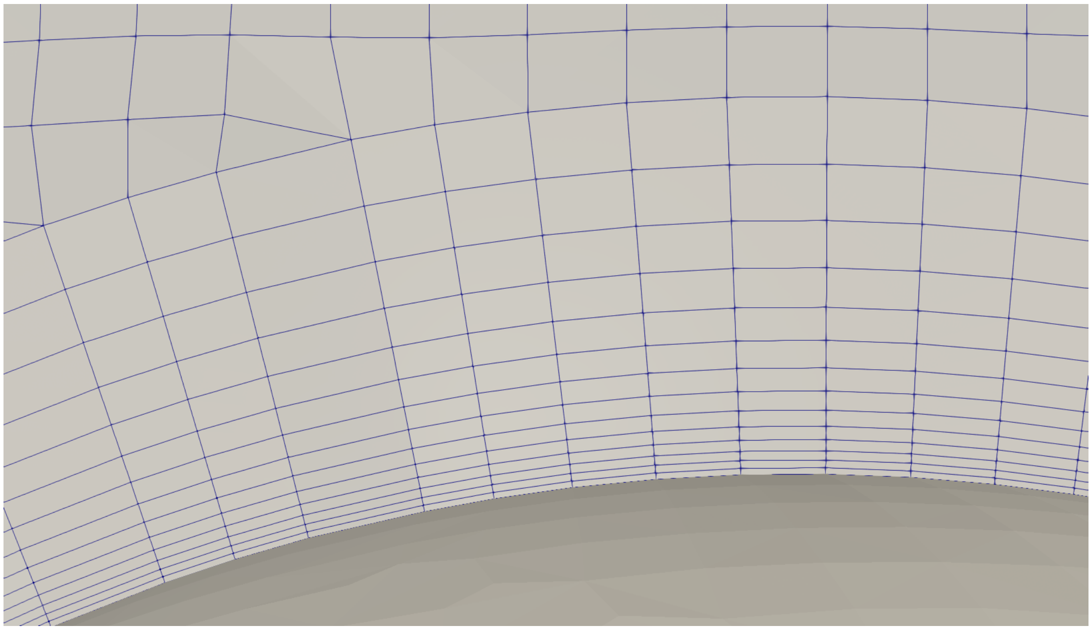

Figure 3.3: Figure 3.2 with additional zoom on the viscous mesh on the sphere

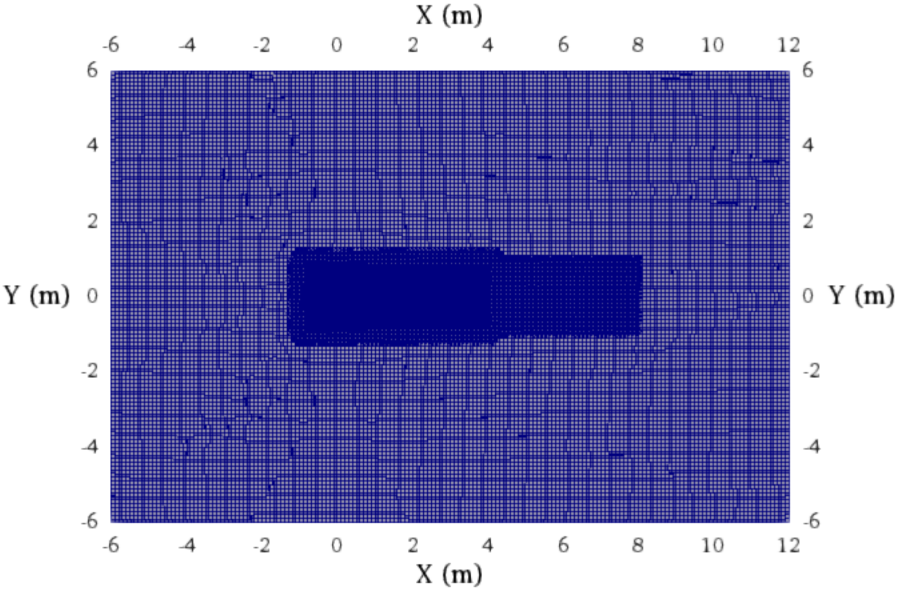

Figure 3.4: Overview of the converging mesh at $Re = 10^6$ in the computational domain, its is refined in areas of particular interest, similar to the converging mesh at $Re = 10^4$

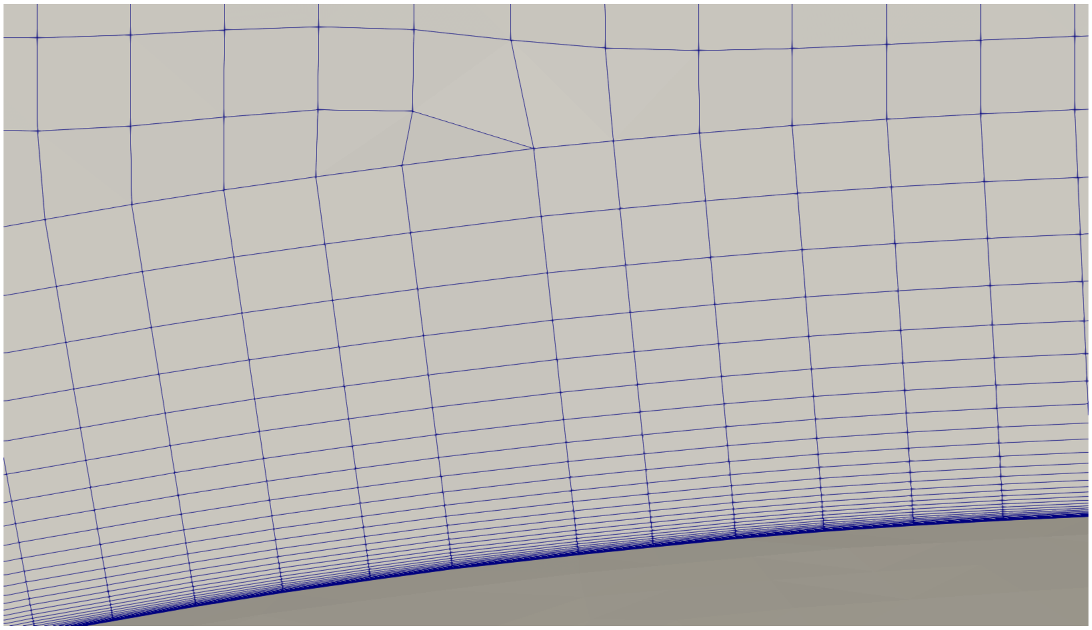

Figure 3.5: Figure 3.4 with additional zoom on the viscous mesh on the sphere

3.2 Results, Validation and Discussion

3.2.1 $Re = 10^4$

The drag coefficient as a function of the number of cells are presented in Figure 3.6. Based on this figure, it seems like $5.13 \cdot 10^5$ cells are sufficient, as the difference in the results of the finer meshes is minor. As seen in Figure 3.6, the result regarding drag coefficient, is in excellent agreement with the experimental results from Achenbach (1974). Achenbach (1974) reports $C_D = 0.4$ and the present results convergence towards $C_D = 0.401$. For the mesh with $5.13 \cdot 10^5$ cells, contour plots for the velocity and pressure are presented in Figures 3.7-3.8 and 3.9-3.10, which shows a symmetrical flow. As seen in the velocity plots, the wake of the sphere covers almost its entire backside. As seen in the pressure plots, the pressure is much larger in the area facing the flow than that facing the wake. This large pressure difference on the sphere results in a high drag force. A streamline plot is presented in Figure 3.11, for which vortices are displayed. A convergence plot is presented in Figure 3.12 which shows the solution converging after 600 iterations. As previously mentioned, the convergence criteria are set when the residuals for pressure and velocities in all directions are less than 10^{-5}. A plot of y^+ is shown in Figure 3.13, which shows that the sphere has an acceptable y^+ value, i.e. less than five. The average y^+ on the sphere is calculated to be 0.64. Finally, the separation point is presented in Table 3.1 and compared with the literature. As seen in this table, the present results have excellent compliance with those obtained by researchers using other simulation software. The mesh itself is already presented in Figures 3.2 and 3.3.

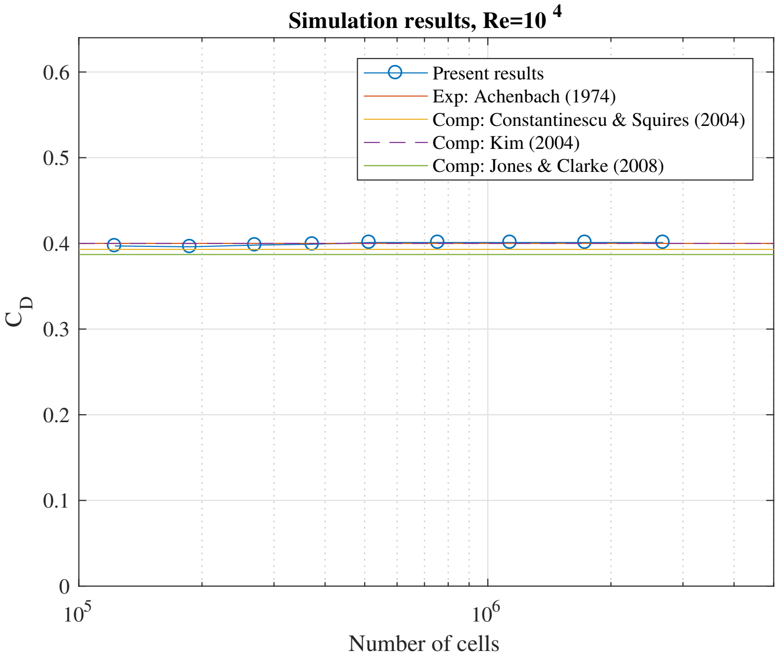

Figure 3.6: Grid sensitivity study with the Reynolds number equal to 10^4, results are compared with the literature. 'Exp' and 'Comp' denotes experimental- and computational study, respectively

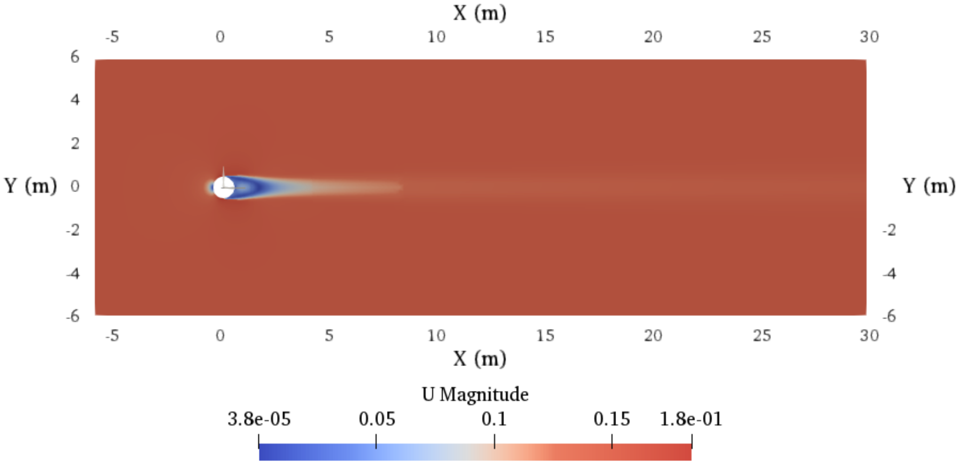

Figure 3.7: Contour plot of the velocity with Reynolds number equal to 10^4. The unit is m/s

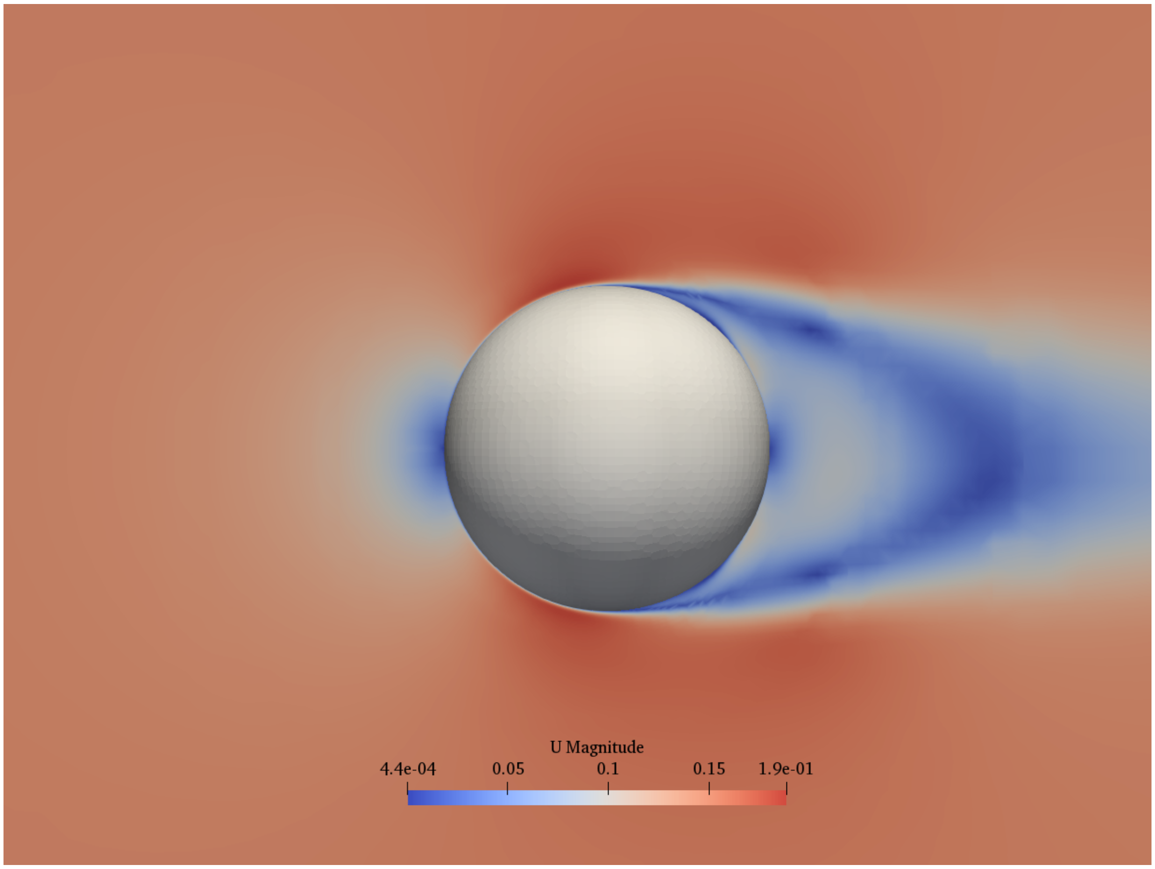

Figure 3.8: Figure 3.7 with additional zoom around the sphere. The unit is m/s

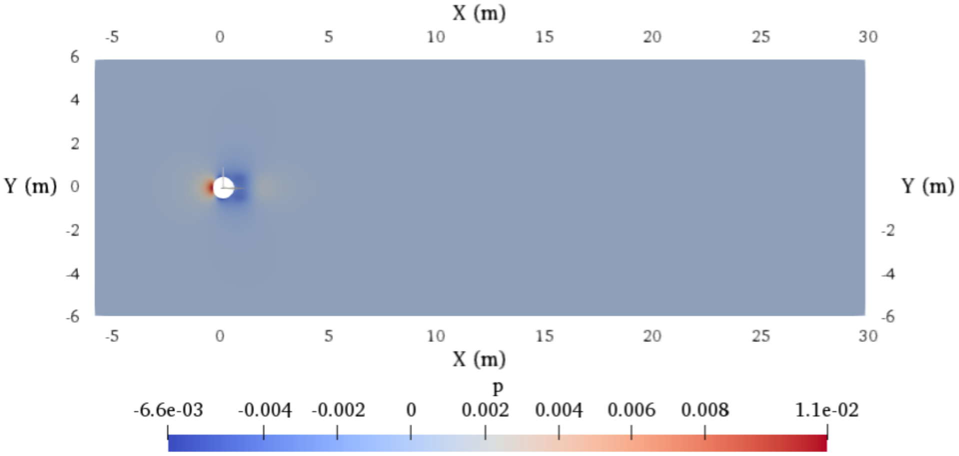

Figure 3.9: Contour plot of the pressure with Reynolds number equal to 10^4. The unit is Pa relative to an atmospheric pressure

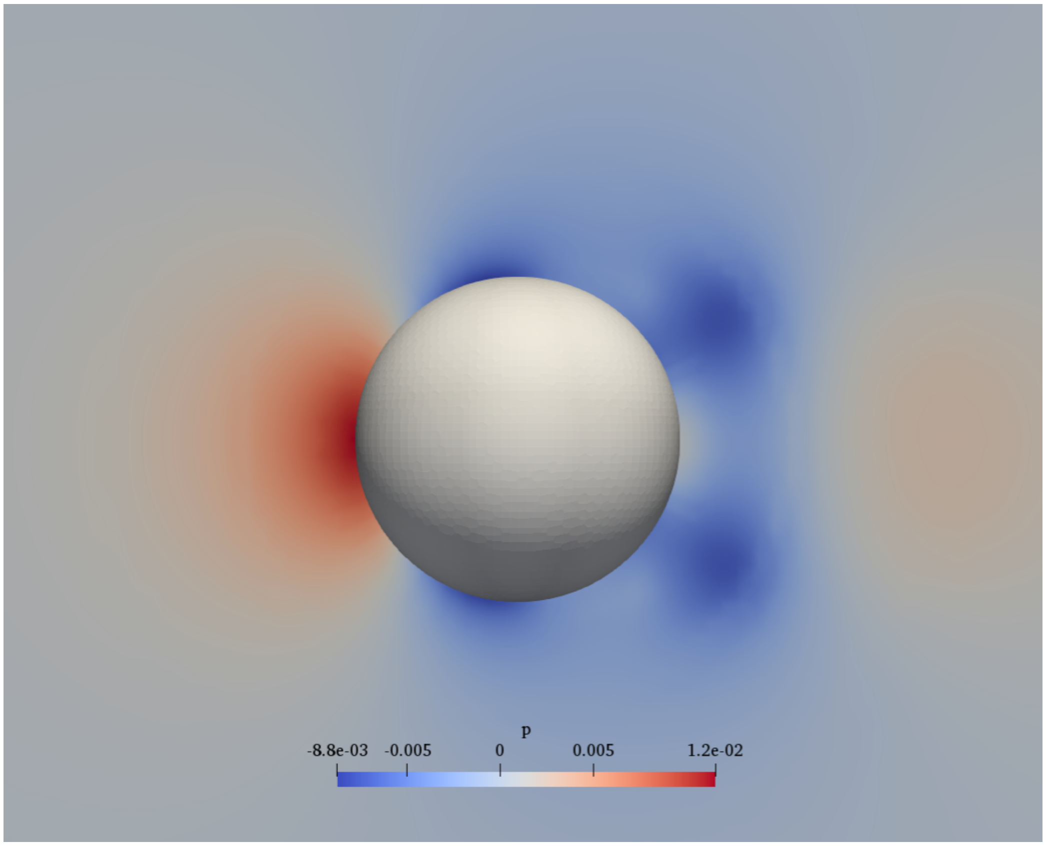

Figure 3.10: Figure 3.9 with additional zoom around the sphere. The unit is Pa relative to an atmospheric pressure

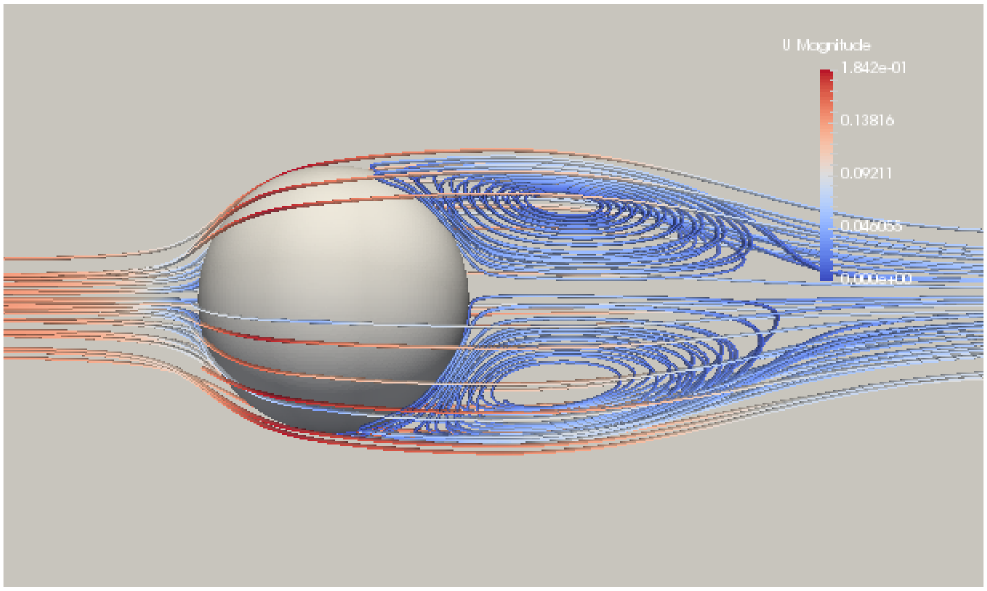

Figure 3.11: Streamline plot with the Reynolds number equal to 10^4. The unit is m/s

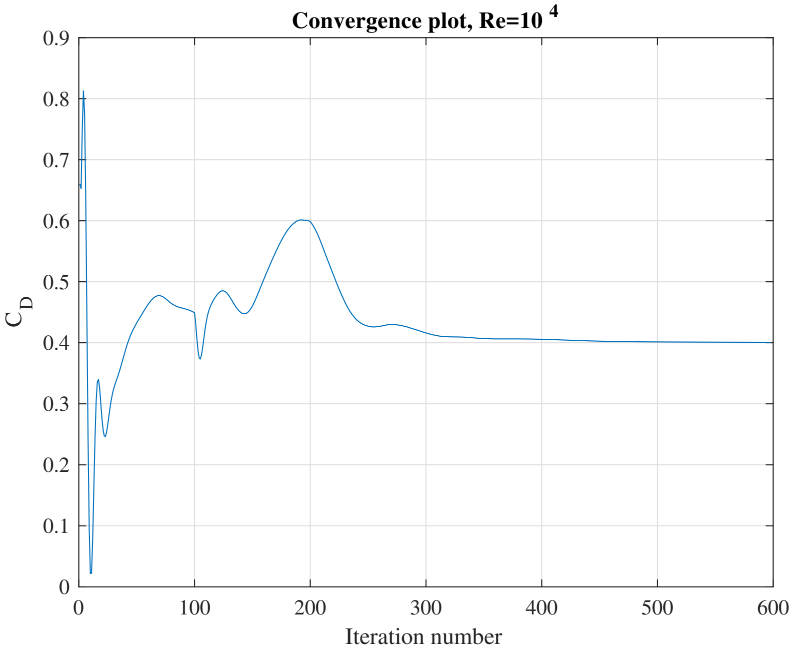

Figure 3.12: Convergence plot with the Reynolds number equal to 10^4

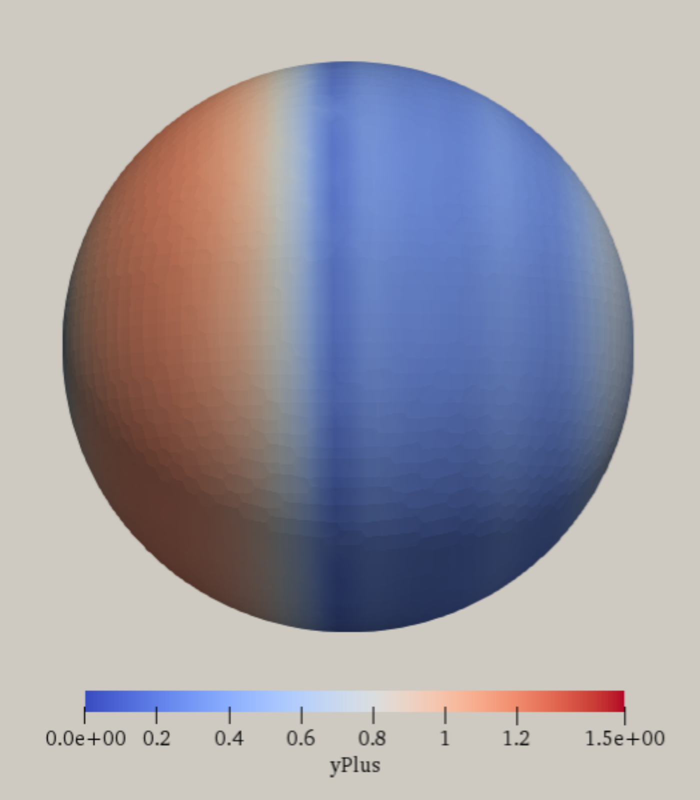

Figure 3.13: y^+ plot with the Reynolds number equal to 10^4

Author	Separation point
Present result	$88 \pm 1\ ^o$
Comp: Jones & Clarke (2008)	$88 \pm 1\ ^o$
Comp: Constantinescu et al. (2003) (LES)	$85 \pm 1\ ^o$
Comp: Constantinescu et al. (2003) ($k-\omega$)	$86.5 \pm 0.5\ ^o$

Table 3.1: The seperation point of the sphere simulated at $Re = 10^4$ compared with literature. 'Comp' denots computational study

3.2.2 $Re = 10^6$

The grid sensitivity study is presented in Figure 3.14 and based on this figure it seems like $6.55 \cdot 10^6$ cells are sufficient to reach convergence. This is noticeably different from the number of cells needed with the $Re = 10^4$ case, as seen by comparing Figures 3.6 and 3.14. By the latter figure, the result, concerning drag coefficient(s), has reasonable compliance with experimental results from Achenbach (1974). For the mesh with $6.55 \cdot 10^6$ cells, contour plots for the velocity and pressure are presented in Figures 3.15-3.16 and 3.17-3.18. These plots show an asymmetrical flow, despite symmetrical flow conditions and geometry. Constantinescu et al. (2003) also report this abnormality with the four different RANS model they applied for turbulence modelling, and, as mentioned in Chapter 3, further reports that the results of drag with the $k-\omega$ turbulence modelling were in reasonable agreement with measurements. This is also the case the with the current results for drag force. As seen in the velocity plots, the wake of the sphere is much narrower than that of the sphere simulated at $Re = 10^4$. The pressure plot of the sphere simulated at $Re = 10^6$ shows that the relative difference between the pressure acting on the area facing the flow and the pressure acting on the area facing the wake, is smaller than that of the sphere simulated at $Re = 10^4$. Thus, the pressure acting on the area facing the flow is counteracted by the pressure acting on the area facing the wake, and as a result, the drag force is reduced.

A convergence plot is presented in Figure 3.19 which shows that convergence is reached after approximately 1000 iterations. A plot of y^+ is shown in Figure 3.20, which shows that the sphere has an acceptable y^+ value. The average y^+ on the sphere is calculated to be 0.53. The separation point is presented in Table 3.2 and compared with the literature. As seen in the latter table, the separation point has reasonable agreement with results of Achenbach (1972). As seen the velocity contour plot presented in Figure 3.16, the separation on the top and bottom side of the sphere is asymmetrical. Hence, the separation point presented in Table 3.2 is the average separation point of the top- and the bottom of the sphere. Similar to the simulation at $Re = 10^4$, the mesh itself is already presented in Figures 3.4 and 3.5.

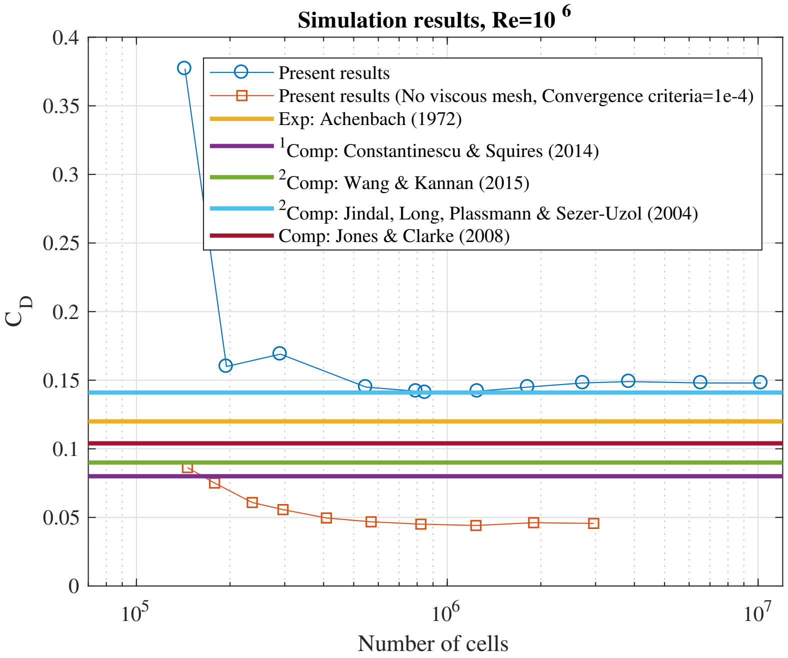

Figure 3.14: Grid sensitivity study with Reynolds number equal to 10^6, results are compared with the literature. 'Exp' and 'Comp' denotes experimental- and computational study, respectively
$^1 Re = 1.14 \cdot 10^6$
$^2 Re = 1.1 \cdot 10^6$

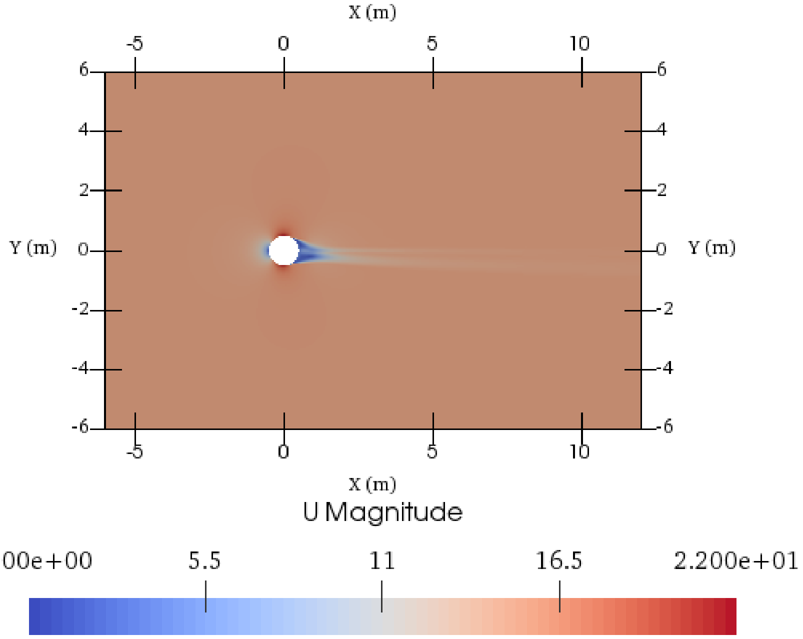

Figure 3.15: Contour plot of the velocity with Reynolds number equal to 10^6, for the mesh with $6.55 \cdot 10^6$ cells. The unit is m/s

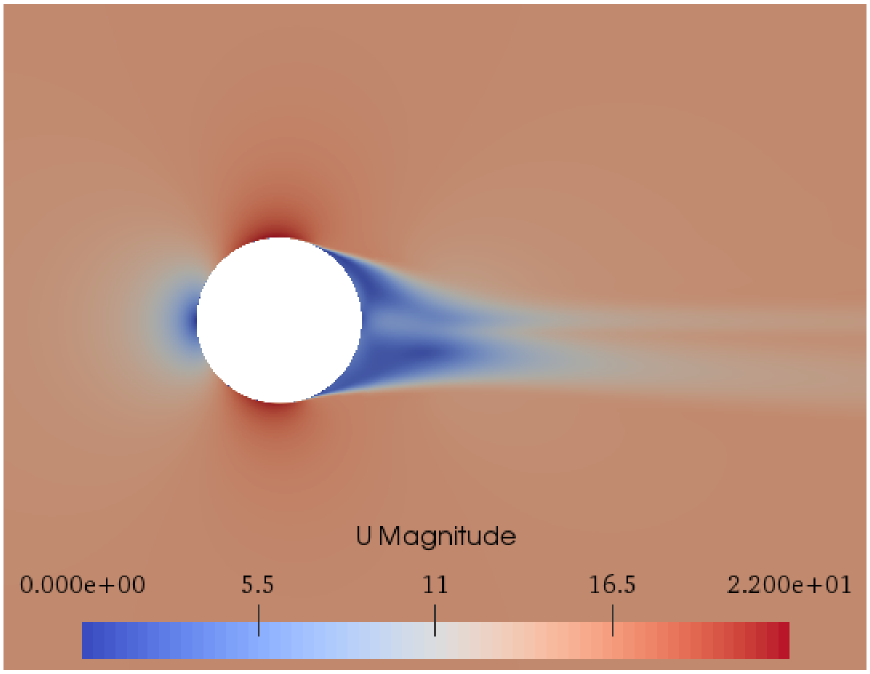

Figure 3.16: Figure 3.15 with additional zoom around the sphere. The unit is m/s

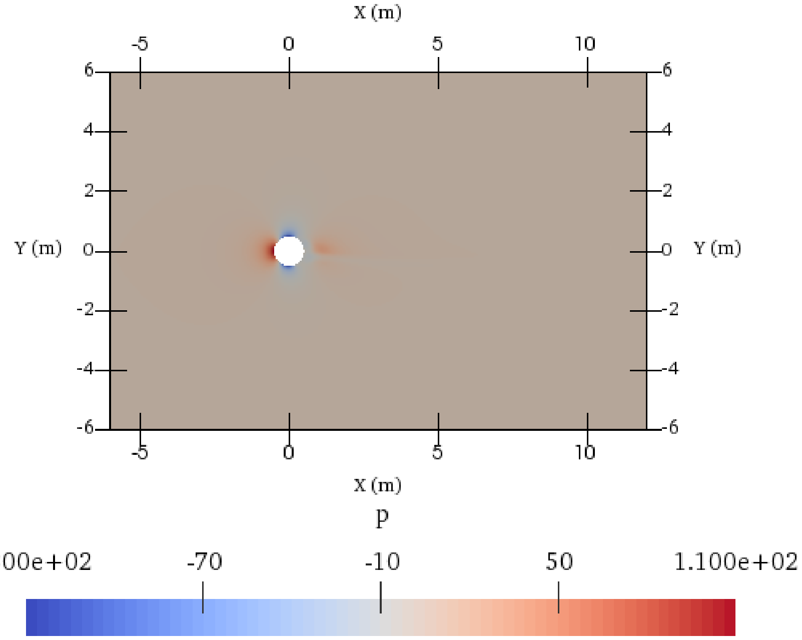

Figure 3.17: Contour plot of the pressure with Reynolds number equal to 10^6, for the mesh with $6.55 \cdot 10^6$ cells. The unit is Pa relative to an atmospheric pressure

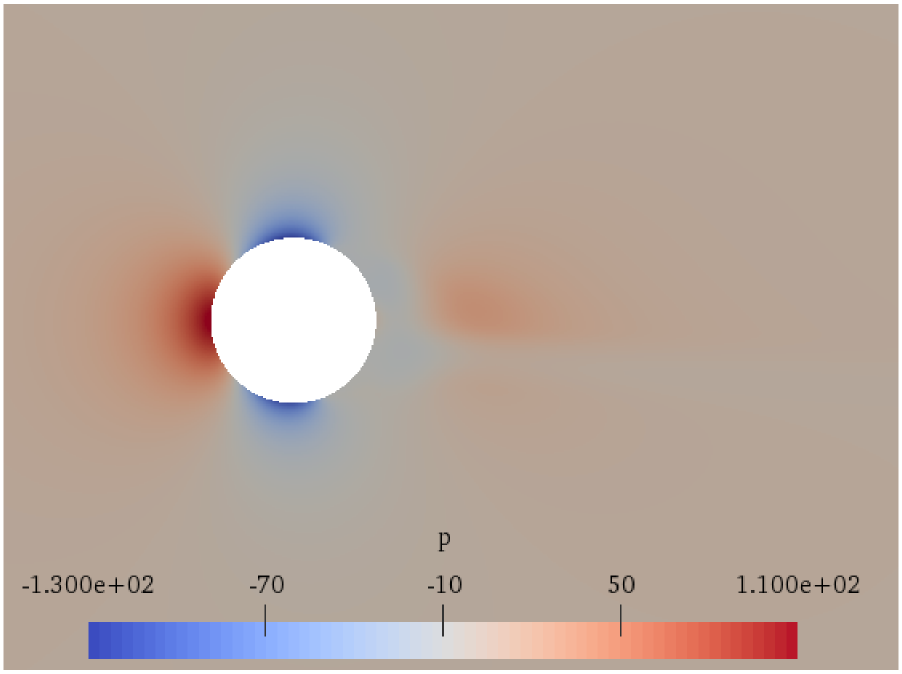

Figure 3.18: Figure 3.17 with additional zoom around the sphere. The unit is Pa relative to an atmospheric pressure

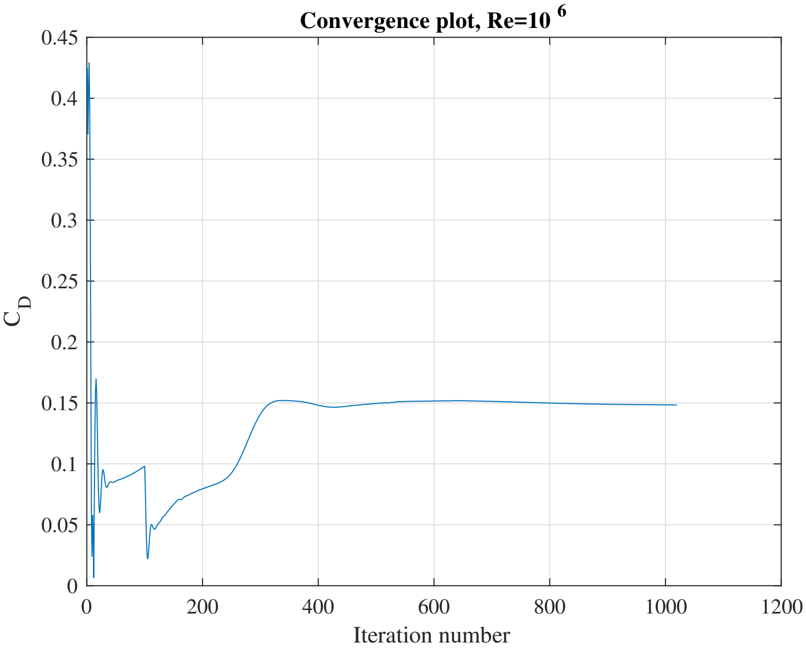

Figure 3.19: Convergence plot with the Reynolds number equal to 10^6, for the mesh with $6.55 \cdot 10^6$ cells

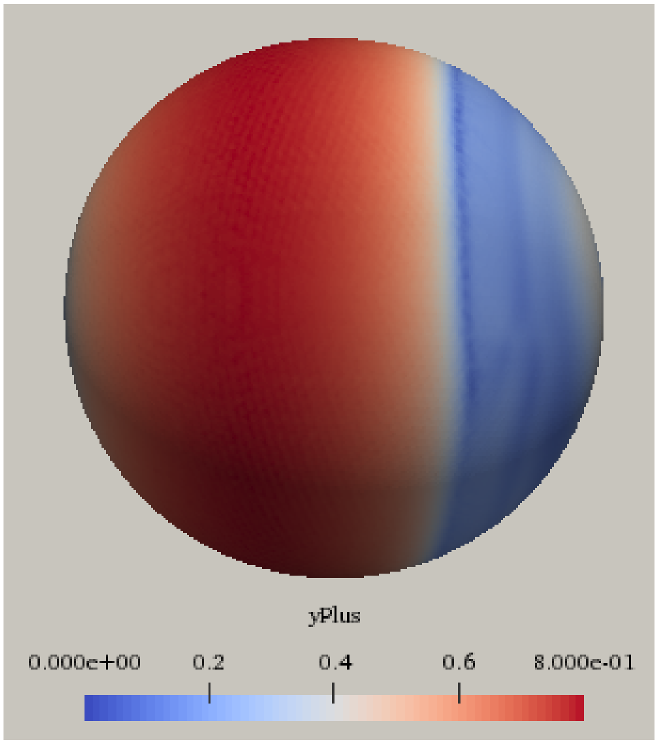

Figure 3.20: y^+ plot with the Reynolds number equal to 10^6

Author	Separation point
Present result	$117^{o} \pm 3^{o}$
Jones & Clarke (2008)	$121^{o} \pm 2^{o}$
Constantinescu & Squires (2004)	$120^{o} \pm 2^{o}$
Achenbach (1972)	120^{o}

Table 3.2: The seperation point of the sphere simulated at $Re = 10^6$ compared with literature

Chapter 4

Simulation of flow over a cyclist

Cycling science has undergone considerable development in the recent years, with several studies on cyclist's riding position alone. The drag force on a cyclist can be investigated by field tests, wind tunnel measurements and numerical simulation by CFD (Blocken & Toparlar, 2015). Defraeye, Blocken, Koninckx, Hespel & Carmeliet (2010) investigated the drag on a cyclist for three different positions using both wind tunnel experiments and CFD with steady RANS and LES turbulence modelling. They report agreement between the experimental and computational results with either turbulence modelling, and states that "CFD is found to be a valuable tool to evaluate the drag of different cyclist positions and to investigate the influence of small adjustments in the cyclist's position". García-López et. al. (2008) studied the aerodynamic drag of five professional cyclists in four postures using wind tunnel experiments. They aimed to reduce the drag by modifying their posture and cycle equipment and the significance of these modifications and reports a 14% reduction in drag by adjusting the posture alone. Beaumont, Taiar, Polidori, Trenchard & Grappe (2018) investigated the aerodynamic effect of helmet shape and head positioning on cyclist drag using CFD and reports the maximum difference of 6.4% by adjusting the head position alone, and only a difference of 1.5% by changing helmet shape for a fixed head position. Blocken, Defraeye, Koninckx, Carmeliet & Hespel (2013) analysed the drag of drafting cyclist, i.e. one cyclist riding behind another, in different postures using both CFD and wind tunnel experiments. They found that both the lead and trailing cyclist experience reduced drag from such a formation, with a maximal drag reduction of 2.6% and 27%, respectively, although not for the same posture. Further, Blocken & Toparlar (2015) analysed the how following a car influences drag, using both CFD and wind tunnel experiments, and reports a drag reduction of 3.7% and 0.2% for a distance of 3.5 and 10 m, respectively. These results are interesting when considering that the International Cycling Union (UCI) only specify a minimum distance between rider and car of 10 m because of safety reasons. According to Blocken & Toparlar (2015), during actual races, the minimum distance is often neither kept and strictly enforced.

4.1 Computational setup

A non-pedalling cyclist model is used with the assumption that the flow past a static leg is similar to the flow past a cyclist's rotating leg at the appropriate phase of leg rotation, and that rotating legs do not influence the relative difference of the upper body postures. A study of Croucha, Burtona, Venninga, Thompsona, Brown & Sheridan (2016) confirmed this assumption and evidenced minor variation between the instantaneous drag and primary vortical structures of a pedaling cyclist compared to a stationary cyclist with the pedals in the same position.

High-quality cell layers are an essential feature of a mesh when investigating drag and can with specific software's be challenging to obtain with complex geometries. In this thesis, the mesh generator implemented in OpenFOAM was utilised, which is known to struggle with generating high-quality cell layer on complex geometries, such as a cyclist model. Researchers may be tempted to accept meshes with questionable y^+ values. Fintelman, Hemida, Sterling & Li (2015) performed simulations of flow around a cyclist subjected to crosswinds, using OpenFOAM, with three meshes having a y^+ value of 82, 60 and 43, which is considerably more than what is usually regarded as acceptable. In OpenFOAM the grid is generated by using blockMesh and snappyHexMesh, where the first creates the background mesh, and the latter refines and possibly modifies the mesh around inserted geometries, such as a sphere or a cyclist, through an iterative process. snappyHexMesh offers a wide range of adjustments for mesh generation, some of them are in this thesis treated as parameters to generate the best mesh possible. These are located under either snapControls, addLayersControls, or meshQualityControls, and are

snapControls

- *nSolverIter*: The maximum number of iterations for the mesh generation

addLayersControls

- *nRelaxIter*: The maximum number of snapping relaxation iterations
- *featureAngle*: The angle above which surface is not extruded
- *maxFaceThicknessRatio*: Stop layer growth on highly warped cells
- *maxThicknessToMedialRatio*: Reduce layer growth where ratio thickness to medial distance is large
- *nLayerIter*: The maximum number of iterations of the layer generation for which default quality constraints are utilised
- *nRelaxedIter*: The maximum number of iterations of the layer generation for which relaxed quality constraints are utilised

meshQualityControls

- *maxNonOrtho*: The maximum non-orthogonality allowed
- *maxBoundarySkewness*: The maximum boundary face skewness allowed
- *maxInternalSkewness*: The maximum internal face skewness allowed
- *maxConcave*: The maximum concaveness allowed

The parameters effect on cell layer generation are observed by changing them individually, to a somewhat extreme value, and observe the result. Parameters with significant effect are further investigated and combined, through this process, *nRelaxIter* and *nSolverIter* both under addLayersControls and *maxNonOrtho* under meshQualityControls were been found to have a positive effect on cell layer generation. However, as a high value of *maxNonOrtho* results in reduced quality cells, it is expected that its negative effects outweigh the positive effects on cell layer generation. Hence, only *nRelaxIter* and *nSolverIter* are modified, with their numerical values set to 50 and 100, respectively. For reference, (CFD Direct, n.d.) claims that typically values for *nRelaxIter* and *nSolverIter* is 5 and 30-100, respectively. The effect on the described changes in *nRelaxIter* and *nSolverIter* are presented in Figure 4.1. Notice that the mesh transition in the latter figure is not according to the guidelines presented in Section 2.3. With the chosen mesh generator, a compromise must be made with having a coarse mesh transition and having reduced cell layer generation at troubled locations on the model. Hence, a course mesh transition is assumed to be more appropriate than a having no viscous mesh at troubled locations of the cyclist model.

Five different 3D scans and postures of the same cyclist, i.e. Tao Geoghegan Hart a professional cyclist and member of Team Sky, are simulated using the same computational setup as for the sphere with Reynolds number equal to 10^6, except for the previously mentioned changes in mesh settings and convergence criteria. The convergence criteria remains unspecified and the simulations are set run for 5,000 iterations. An overview of the Hart models is presented in Figure 4.2. With reference to the naming presented in the latter figure, an overview the mesh and computational domain of *HorizontalCrank* is shown in Figure 4.3, while details of the mesh are presented in Figure 4.4. Several problematic areas of cell layer generation are shown in the latter figure, including the fingers and the back of the helmet in Figures 4.4b and 4.4d, respectively.

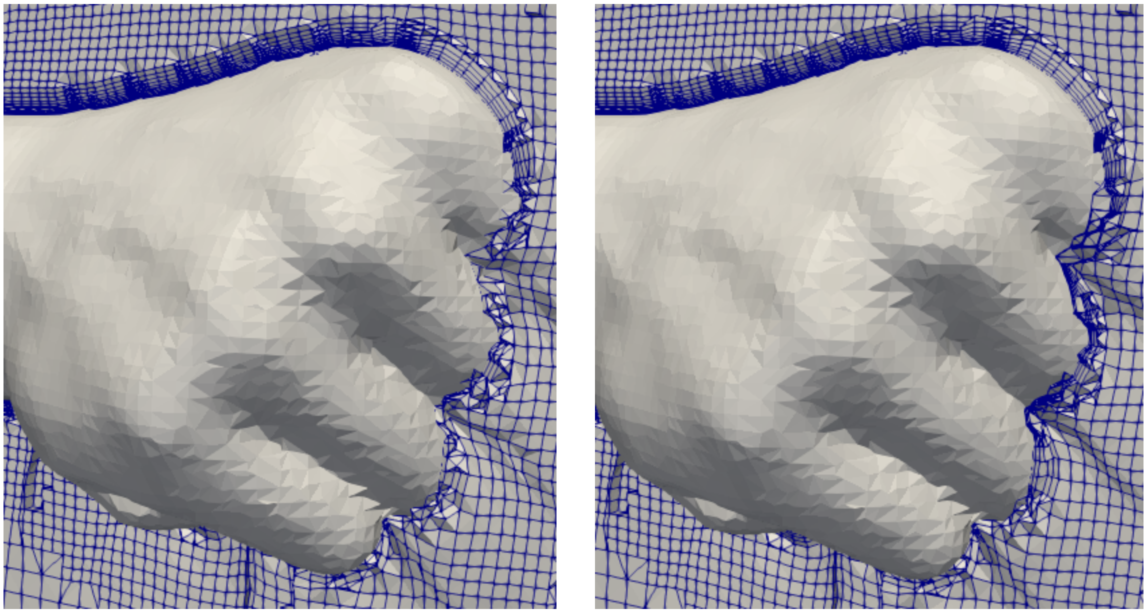

(a) Original settings

(b) Modified settings

Figure 4.1: The effect of changing *nRelaxIter* under addLayersControls and *maxNonOrtho* under meshQualityControls on cell layer generation, with original settings in 4.1a and modified settings in 4.1b. The difference is particularly visible in the region around the fingers

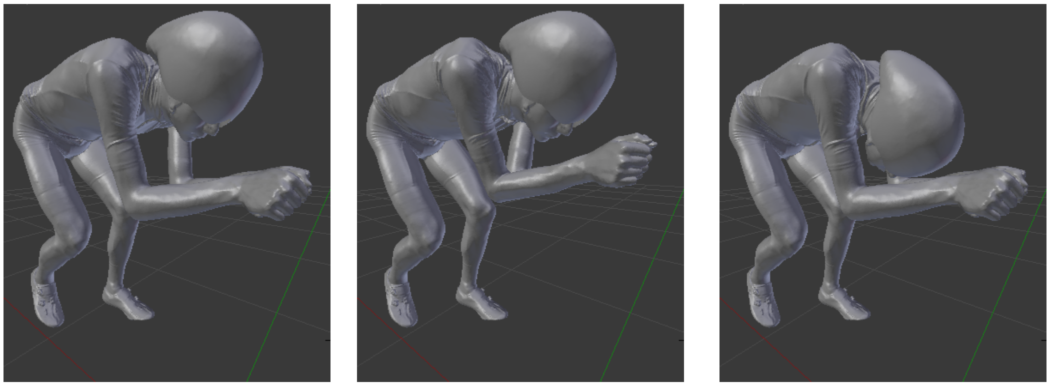

(a) HorizontalCrank (b) HandsCloseTogether (c) HeadDown

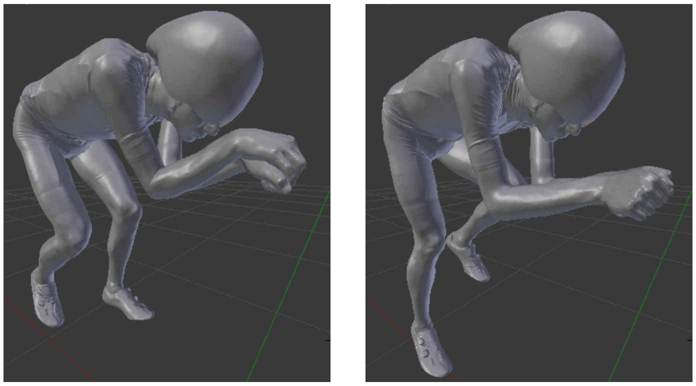

(d) HandsOnTop (e) VerticalCrank

Figure 4.2: Overview of the Hart models simulated in this thesis, together with corresponding name referencing

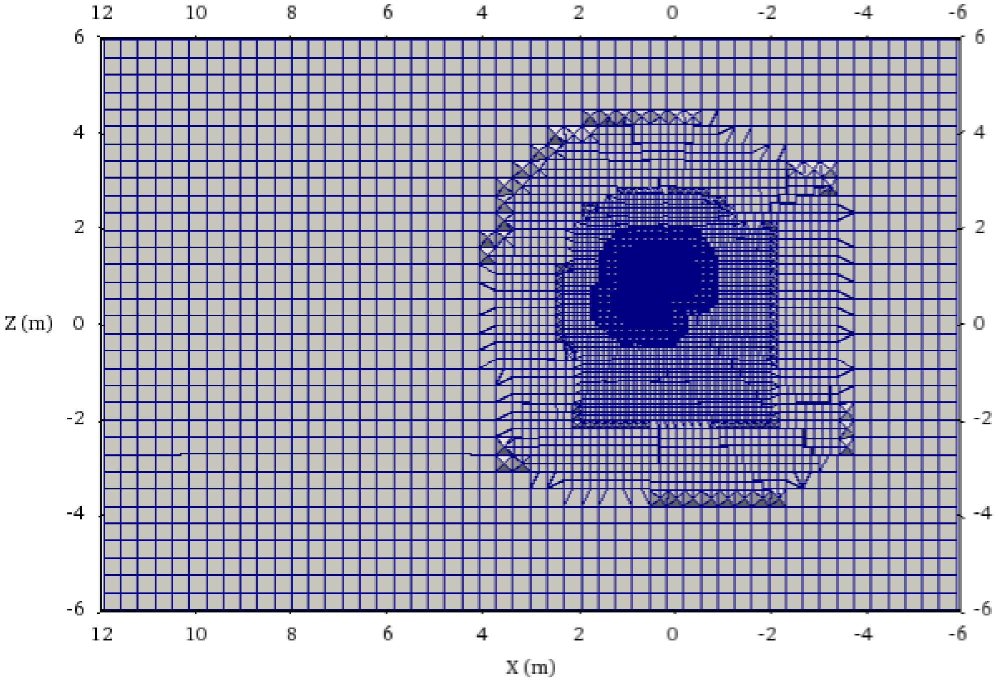

Figure 4.3: An overview of the mesh and the computational domain of the Hart HorizontalCrank simulation. The inlet is along the right vertical edge, and the outlet is along the left vertical edge

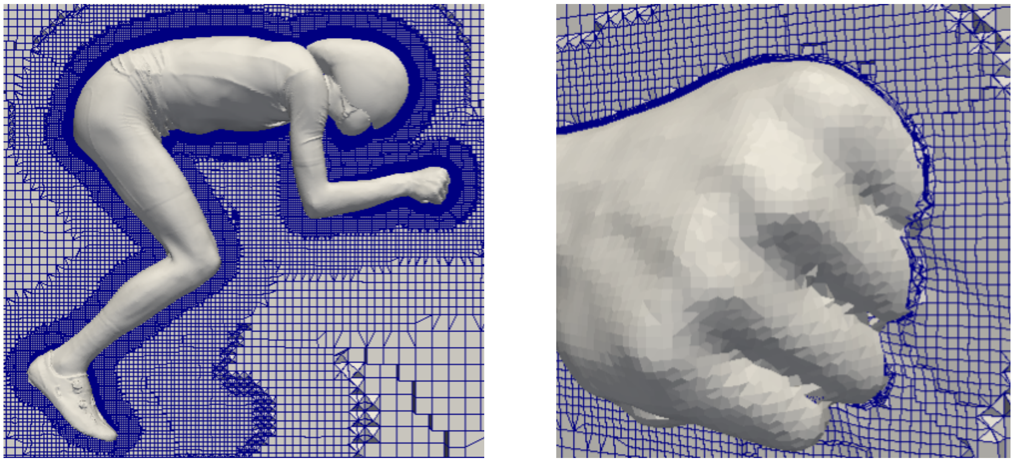

(a) Figure 4.3 with additional zoom

(b) Cell generation around the hand

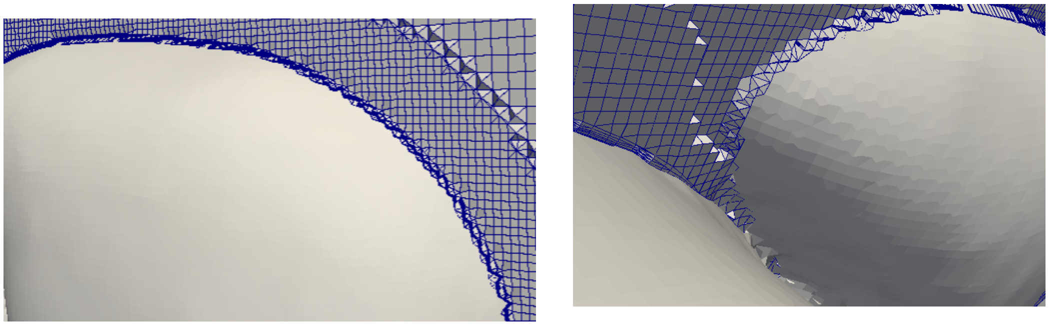

(c) Cell layer generation on the top of the helmet

(d) Cell layer generation between the back of the helmet and the upper back

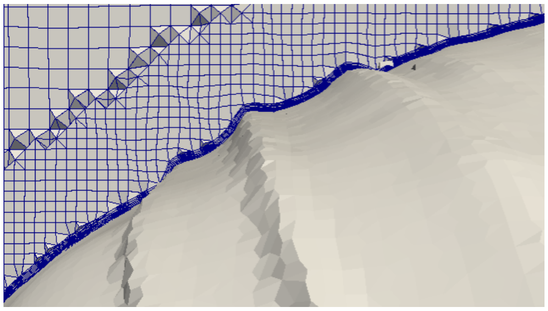

(e) Cell layer generation on wrinkled clothing at the lower back

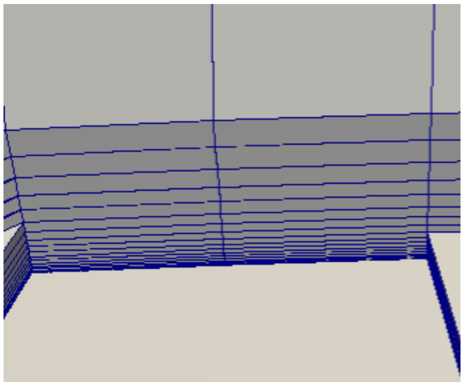

(f) Zoom on a sucessful cell layer generation

Figure 4.4: Details of the mesh utilised for the Hart HorizontalCrank simulation

4.2 Results and discussion

A convergence plot of the HorizontalCrank model is presented in Figure 4.5. Based on this figure, it seems that the two finer meshes with $10.1 \cdot 10^6$ and $21.4 \cdot 10^6$ cells convergence towards a drag force of 22 N, except for the instability issues which the mesh with $21.4 \cdot 10^6$ cells encounter at iteration 3,700. The meshes with $4.8 \cdot 10^6$ and $6.7 \cdot 10^6$ cells seem to convergence towards a drag force value of 22 N. Due to the instability issues encountered with finer meshes, the remaining Hart models are simulated with the mesh settings that correspond to the mesh with $6.7 \cdot 10^6$ cells. Thus, achieving approximately the same number of cells. A convergence plot of all the Hart models with approximately $6.7 \cdot 10^6$ cells are shown in Figure 4.6 and the simulation results are summarised in Table 4.1. As seen this table, despite unsuccessful cell layer generation in these among other areas, acceptable average values of y^+ are obtained for all the different Hart models, as seen in Table 4.1. The HandsOnTop model is rotated 2 ^{o} around the axis which is normal to the ground to cope with instability issues. This rotation corresponds to a 2 ^{o} crosswind. In Table 4.2, the results are compared with results of Dr Luca Oggiano for which the commercial meshing software STAR-CCM+ is utilised. As seen in this table, the results of Dr Luca Oggiano have a higher F_D than the present results. However, the relative differences compared to HorizontalCrank, also seen in the latter table, have reasonable compliance. The results are furthered compared with the literature in Table 4.3. The models of the literature not are identical to those simulated in this thesis. However, the comparison shows that the present results are roughly in the same range as the computational and experimental studies of the literature.

The VerticalCrank and HandsCloseTogether are the models with greatest and least drag, respectively, as seen in Table 4.1. However, as the VerticalCrank model has a different leg position, the HandsCloseTogether model is instead compared with HorizontalCrank, i.e. the model with next greatest drag. Contour velocity plots for the HorizontalCrank and HandsCloseTogether model are presented in Figures 4.7 and 4.9. As seen in Figure 4.7a, the hand, arm and leg position of HorizontalCrank seem to generate two dominant low-velocity zones behind the cyclist, as opposed to only one behind the cyclist in the HandsCloseTogheter model in Figure 4.9a. As identified in the simulation of flow around a sphere, a small wake is beneficial with regards to minimise drag. However, the major difference in terms of flow structure between the two models is identified when comparing 4.7b and 4.9b. In the latter figure, the flow travels relatively smoothly past the cyclist and is almost symmetrical. In Figure 4.7b however, the flow is much more chaotic and far less symmetrical. Pressure contour plots for the same models are presented in Figures 4.8 and 4.10. By comparing these figures, we see that that the HandsCloseTogether model has a reduced pressure in front of the thighs compared to the HorizontalCrank model. Additionally, the pressure at the backside of the thighs is increased in HandsCloseTogether model compared to the HorizontalCrank model. Decreased pressure in front of the thighs and increased pressure in the back of the thighs is beneficial with regards to minimise drag. Hence, this at least partly explains the reduced drag.

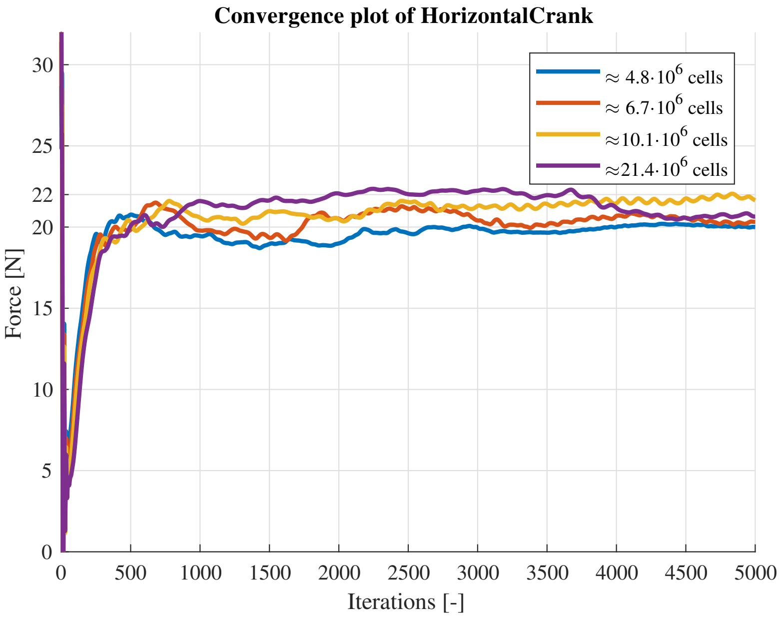

Figure 4.5: Convergence plot of Hart HorizontalCrank

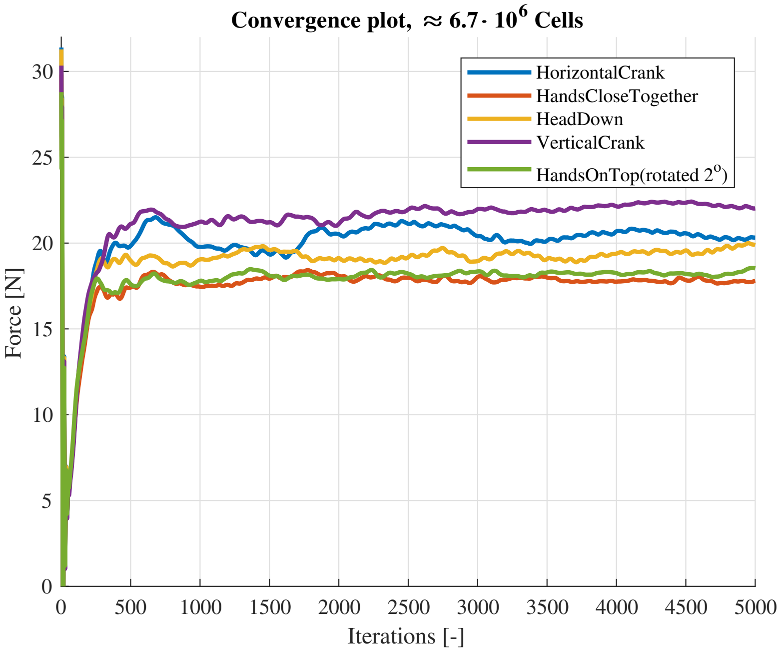

Figure 4.6: Convergence plot of all of the Hart models

Model	Average F_D $[N]$	σ_{std} of drag	Average y^+	A $[m^2]$	$C_D A$
HorizontalCrank	20.48	0.0998	2.36	0.282	0.182
HandsCloseTogether	17.80	0.0977	2.31	0.279	0.158
HeadDown	19.42	0.2059	2.38	0.272	0.173
VerticalCrank	22.19	0.1120	2.31	0.281	0.197
HandsOnTop (rotated 2^o)	18.24	0.1463	2.52	0.277	0.162

Table 4.1: Simulations results of the Hart models summarised. The Average F_D is calculated based on the average value between iteration 3,500 and 5,000, while the δ_{std} is the standard deviation calculated between iteration 4,500 and 5,000

Model	Present results		Results using STAR-CCM+	
	Average F_D $[N]$	$\frac{Avg.\ F_D - 20.48}{20.48}$ [%]	F_D $[N]$	$\frac{F_D - 26.53}{26.53}$ [%]
HorizontalCrank	20.48	0	26.53	0
HandsCloseTogether	17.80	-13.1	23.1	-12.9
HeadDown	19.42	-5.2	24.61	-7.2
VerticalCrank	22.19	8.3	27.46	3.5
HandsOnTop (rotated 2^o)	18.24	-11		
HandsOnTop			23.54	-11.3

Table 4.2: Present results compared with result of Dr. Luca Oggiano for which the commercial meshing software STAR-CCM+ is utilised

Author	AC_D [m^2]
Exp: Blocken et al. (2013)	0.134
Comp: Blocken et al. (2013)	0.135
Exp: Defraeye et al. (2010)	0.134
Comp: Defraeye et al. (2010)	0.150
Comp: Beaumont et al. (2018)	0.138-0.149
Present results	0.162-0.197

Table 4.3: Present results compared with the literature. All numerical values apply for a cyclist without a bike. 'Exp' and 'Comp' denotes experimental- and computational study, respectively

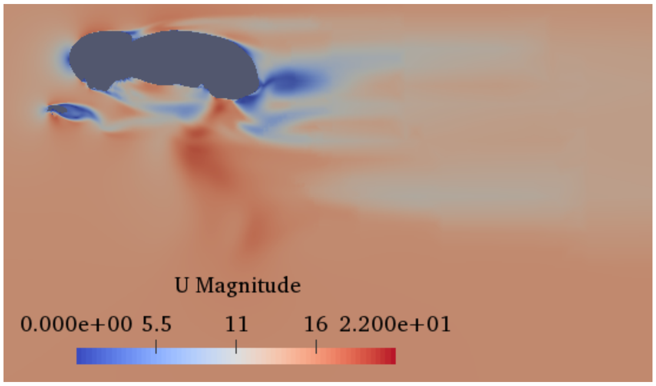

(a) Section view from the side

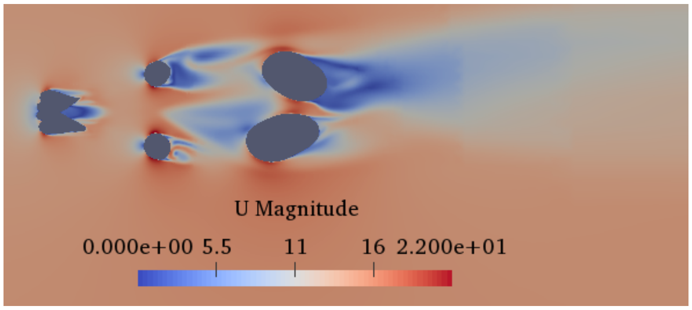

(b) Section view from the top

Figure 4.7: Velocity contour plots for the HorizontalCrank model, i.e. the 3D scanned cyclist model with the greatest drag force except for VerticalCrank. The unit is m/s

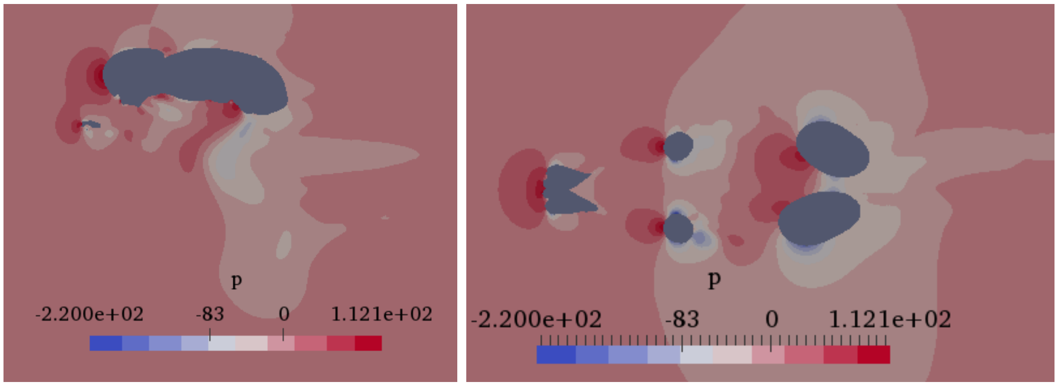

(a) Section view from the side (b) Section view from the top

Figure 4.8: Pressure contour plots for the HorizontalCrank model, i.e. the 3D scanned cyclist model with the greatest drag force except for VerticalCrank. The unit is Pa relative to an atmospheric pressure

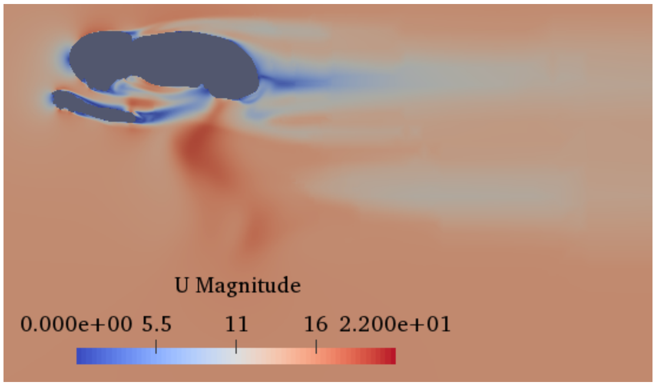

(a) Section view from the side

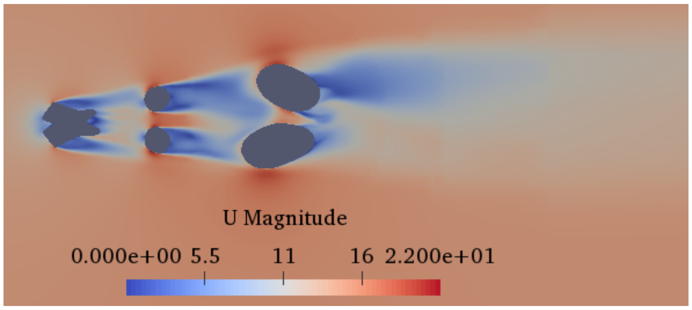

(b) Section view from the top

Figure 4.9: Velocity contour plots for the HandsCloseTogether model, i.e. the 3D scanned cyclist model with the least drag force. The unit is m/s

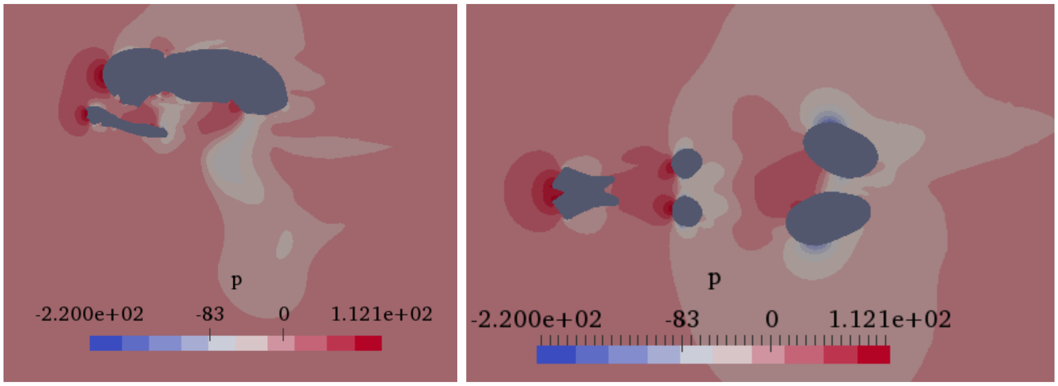

(a) Section view from the side

(b) Section view from the top

Figure 4.10: Pressure contour plots for the HandsCloseTogether model, i.e. the 3D scanned cyclist model with the least drag force. The unit is Pa relative to an atmospheric pressure

Chapter 5

Optimisation of cyclist posture

According to studies performed by Grappe et. al. (1997), the drag force is 90% of the total resistance which a cyclist experience while travelling on a horizontal hard-ground in windless conditions at cyclic race speeds. Grappe et. al. (1997) measured the total resistance of opposing the motion, i.e. a force, of a cyclist in different positions using a mechanism for measuring mechanical power. Grappe et. al. (1997) reports that 90% of this force depends on the aerodynamic drag of air, further, a 27.8% reduction in AC_D by changing the posture of the cyclist is reported. Garcia (2008) studied the aerodynamic drag force on five individual professional cyclists by using a wind tunnel, with the aim for reducing the aerodynamic drag by modifying the cyclist's posture and cyclic equipment, and reports a 14% decrease in drag by adjusting (only) the cyclist's posture. Thus, based on these studies, the potential gain of cycling with the optimal posture is tremendous. In this chapter, we shall consider a validation of the method of skeleton rigging and parameter study of the cyclist simulated in Chapter 4.

5.1 Validation of method of skeleton rigging

To validate the method of skeleton rigging, a 3D scanned model of an existing model of a cyclist, i.e. HoriozontalCrank of Tao Geoghegan Hart, is modified to another existing position of the same cyclist, i.e. HandsCloseTogether, by the use of skeleton rigging. Thus, the results can be compared and the method of skeleton rigging validated. The initial models are shown inside one another in Figure 5.1. The first step of the process is to create the bones necessary to moves the limbs as desired. As seen in Figures 5.1a-5.1c, the legs and helmet are overlapping. Hence, there is no need for skeleton rigging the legs and neck. Also, as seen in the same figures, the hands have some need of modification, and the shoulders even more, while the largest need for modification is seen in the arms. The more limbs that are to be moved, the more bones are needed. Creating and fitting a lot of bones can be a tedious process, this gave the motivation to use three different approaches to skeleton rigging, to find out really how much effort that is needed to obtain a reasonable result.

The least effort which is believed to return a reasonable model is obtained by only modifying the position of the arms. Hence this is the first approach. The second approach involves modifying the arms and shoulders, and the third approach involves modifying the same as in the second approach in addition to the hands. The models constructed using the first, second and third approach corresponds to a coarse, medium and fine model, respectively. Hence, they are renamed so. The skeletons of the different models are presented in Figure 5.2. The resulting coarse model is presented in Figures 5.3a-5.3c, the medium model in Figures 5.3d-5.3f, and the fine model in Figures 5.4a-5.4c. The computational setup described in Chapter 4 are applied to these models, and corresponding simulation results are presented graphically in Figure 5.5, and numerically in Table 5.1.

As seen in table 5.1, the avg. F_D of the coarse, medium and fine model is 5.2, 3.4 and 3.5 %

greater than that of the goal model HandsCloseTogether. Hence, for this case, little improvement was achieved by advancing the skeleton rigging. A negative improvement was even achieved by comparing the medium and fine model. However, a change of 0.1% is considered negligible. Further, a relative difference of 3.4 % is considered acceptable, and the method of skeleton rigging is thereby validated. By comparing the contour plots presented in Figures 5.6-5.8, minor differences are seen between the section views from the side. The perhaps largest difference is in the area beneath the torso as seen by comparing Figures 5.6a and 5.7a or Figures 5.6a and 5.8a. By comparing the section views from the top, i.e. Figures 5.6b, 5.7b and 5.8b, small changes are identified between the elbows and thighs. Additionally, the area behind the right thigh of Figure 5.8b seem to have lower velocities compared to the others. By comparing the contour velocity plots of the fine model and the goal model, HandsCloseTogether, i.e Figures 5.8 and 4.9, a small difference is visible in the area behind the left elbow, while the larger difference is between the area behind the thighs. The difference behind the thighs may raise the question if one of the models have a slight rotation compared to the other, based on the authors best judgement this is not the case. Pressure contour plots for the coarse, medium and fine models are presented in Figures 5.9-5.11 and shows relatively little difference between one another. Further, the pressure plots for the coarse and medium model seem to match well with those of the goal model, as seen by comparing Figures 5.9 and 5.10 to Figure 4.10.

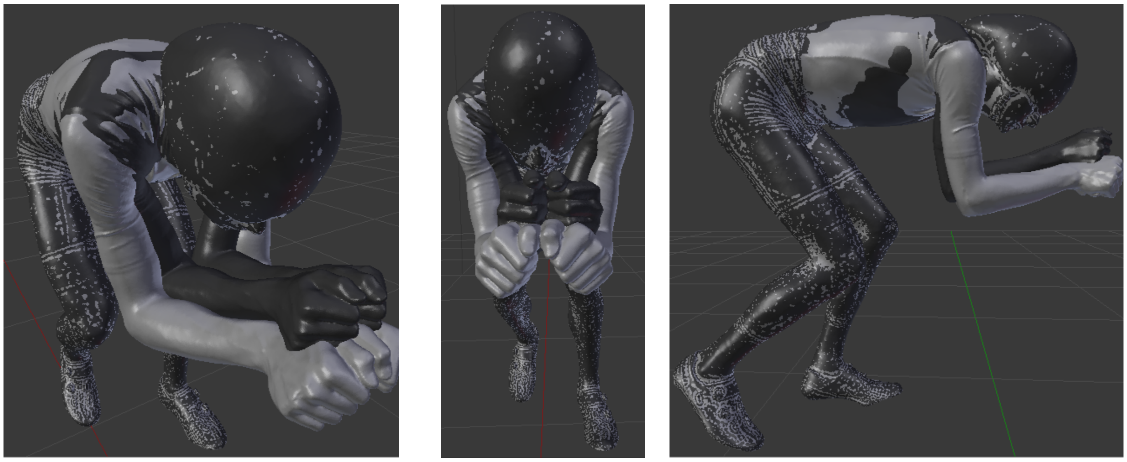
(a) Base- and goal model, overview (b) Base- and goal model, front view (c) Base- and goal model, side view

Figure 5.1: Comparison of the base-, goal- and digitised model. The light grey model, i.e. Hart HorizontalCrank, is to be digitised and modified to the same posture as the dark grey model, i.e. Hart HandsCloseTogether

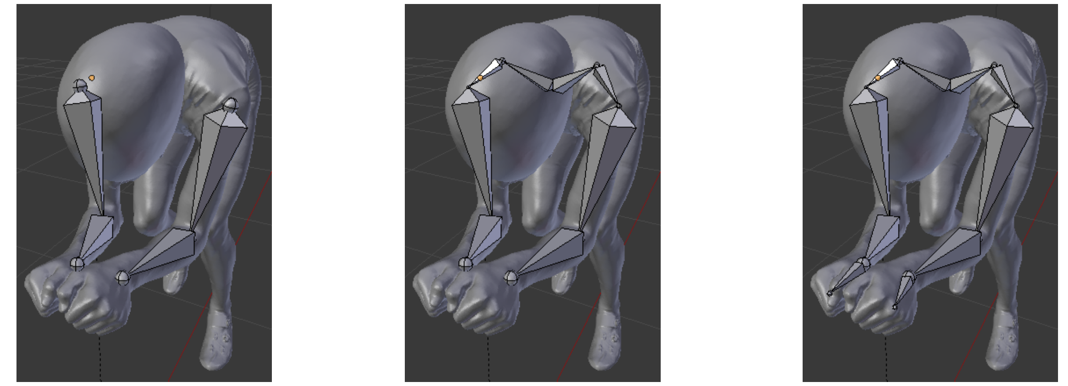

(a) Skeleton of coarse model (b) Skeleton of medium model (c) Skeleton of fine model

Figure 5.2: The skeletons of the different models

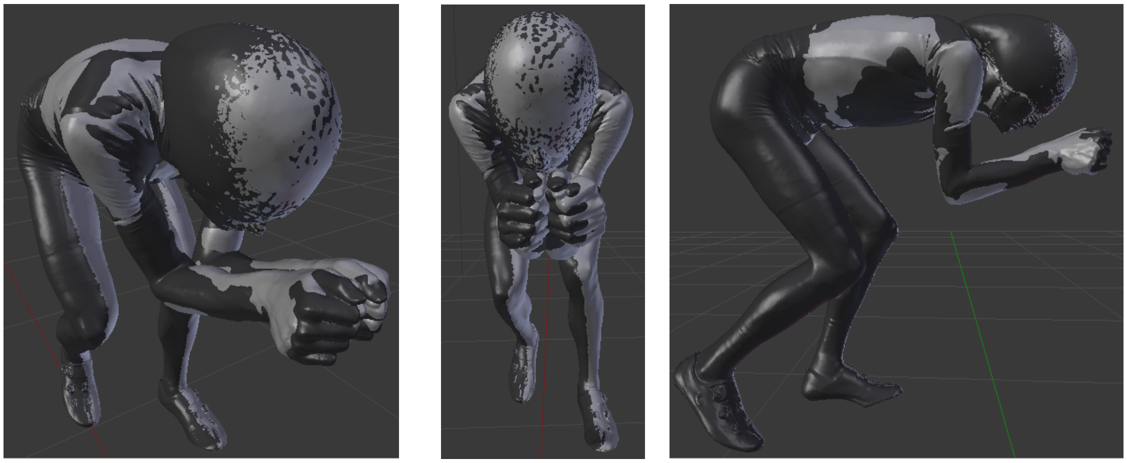

(a) Coarse approach, overview (b) Coarse approach, front view (c) Coarse approach, side view

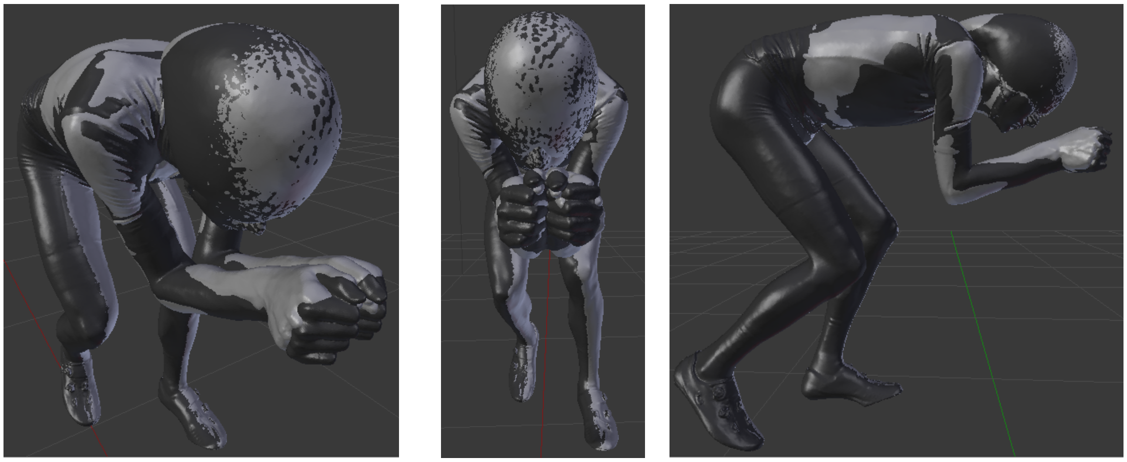

(d) Medium approach, overview (e) Medium approach, front view (f) Medium approach, side view

Figure 5.3: Comparison of the two original models, the dark grey model, i.e. Hart HorizontalCrank, is to be digitised and modified to the same posture as the light grey model, i.e. Hart HandsCloseTogether

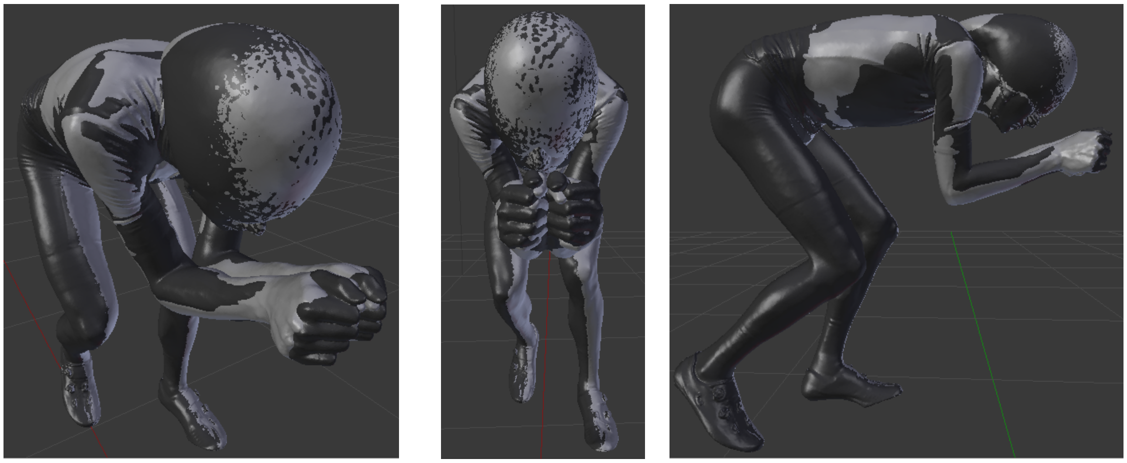

(a) Fine approach, overview

(b) Fine approach, front view

(c) Fine approach, side view

Figure 5.4: Comparison of the two original models, the dark grey model, i.e. Hart HorizontalCrank, is to be digitised and modified to the same posture as the light grey model, i.e. Hart HandsCloseTogether

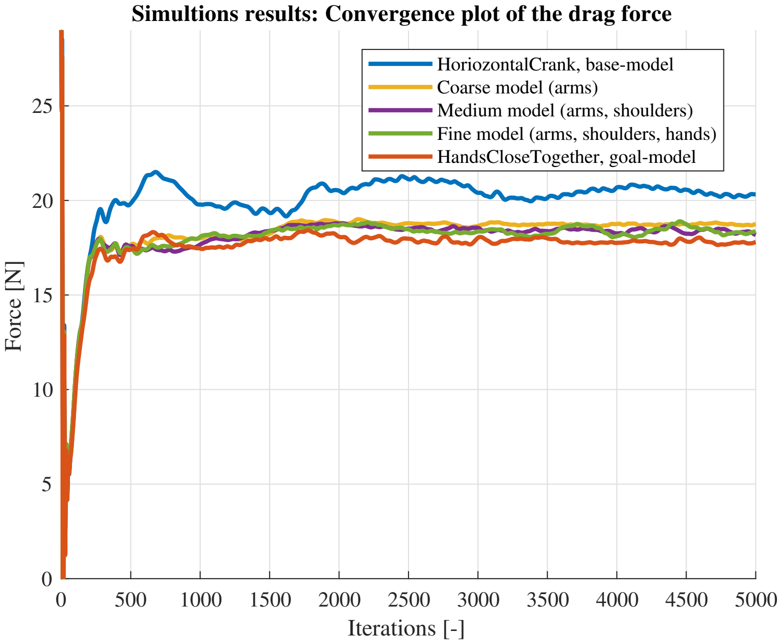

Figure 5.5: Results for the validation of skeleton rigging, convergence plot of the drag force for each model created with corresponding approach, compared with the base model, and goal model

Model	Avg. F_D [N]	(Avg. F_D-17.8)/17.8 [%]	σ_{std}
HorizontalCrank (base model)	20.48	15	0.0998
Coarse model	18.73	5.2	0.0394
Medium model	18.41	3.4	0.0962
Fine model	18.42	3.5	0.143
HandsCloseTogether (goal model)	17.8	0	0.0977

Table 5.1: Numerical results of drag force for the validation of skeleton rigging. The avg. F_D is calculated for the drag force between iteration 3500 and 5000, as displayed in Figure 5.5, while the standard deviation σ_{std} is calculated based on the drag force between iteration 4500 and 5000.

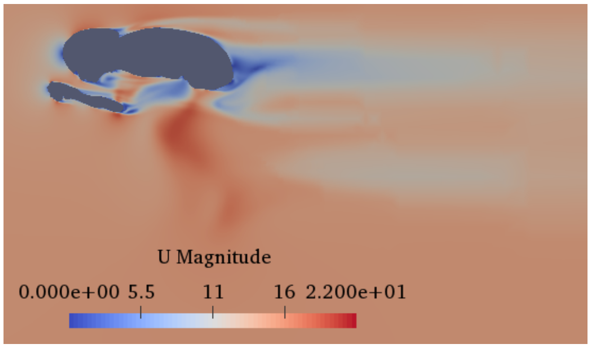

(a) Section view from the side

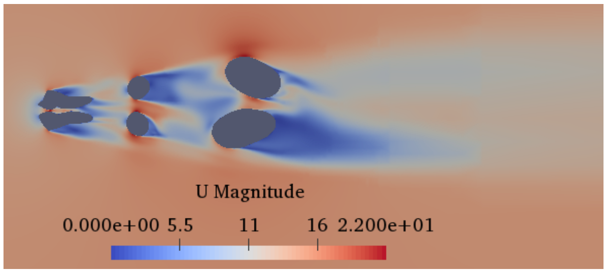

(b) Section view from the top

Figure 5.6: Velocity contour plots for the coarse model. The unit is m/s

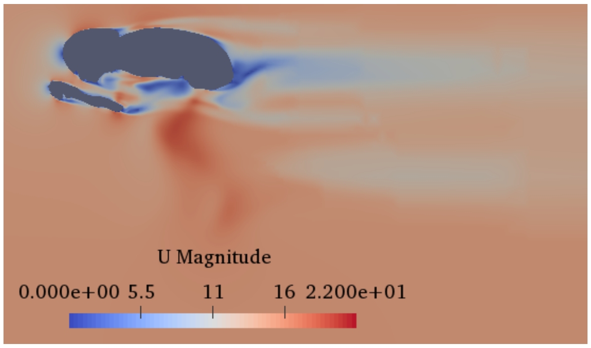

(a) Section view from the side

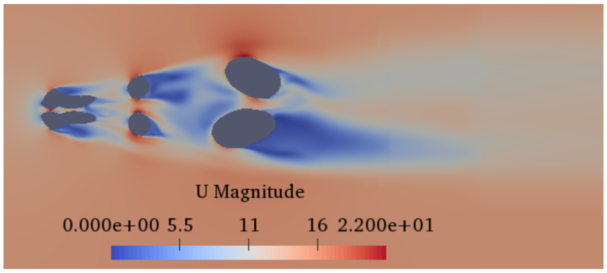

(b) Section view from the top

Figure 5.7: Velocity contour plots for the medium model. The unit is m/s

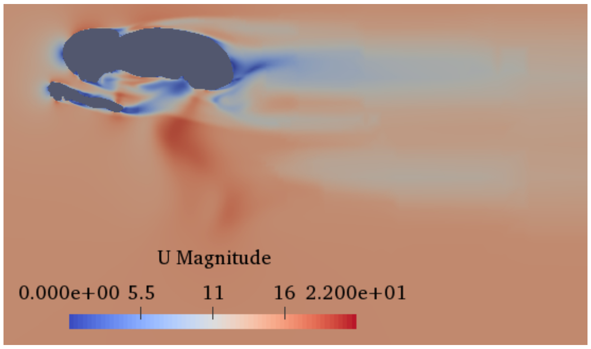

(a) Section view from the side

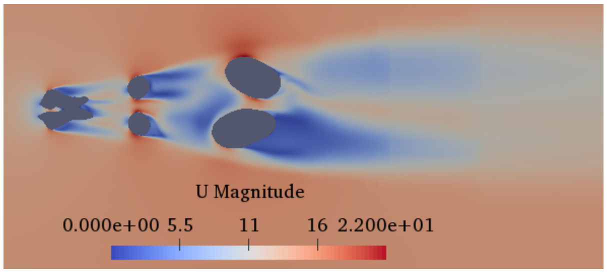

(b) Section view from the top

Figure 5.8: Velocity contour plots for the fine model. The unit is m/s

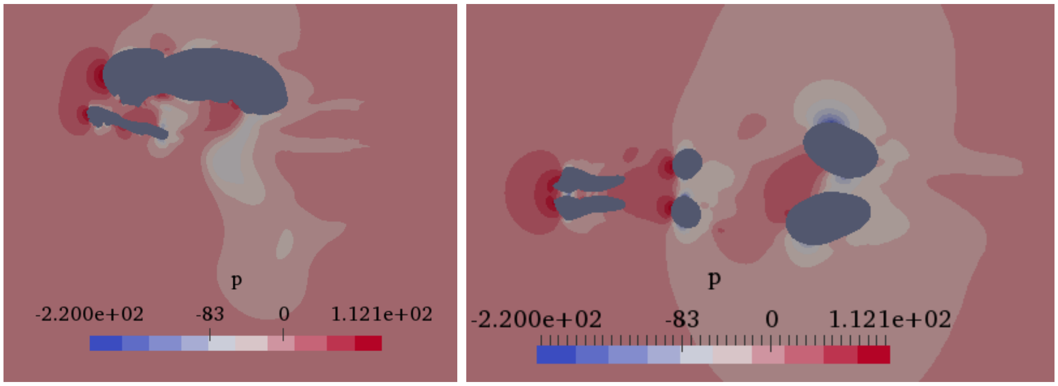

(a) Section view from the side

(b) Section view from the top

Figure 5.9: Pressure contour plots for the coarse model. The unit is Pa relative to an atmospheric pressure

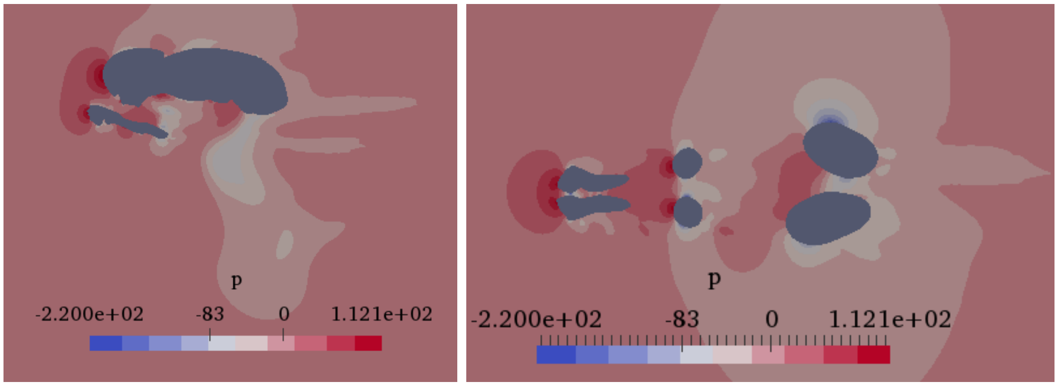

(a) Section view from the side

(b) Section view from the top

Figure 5.10: Pressure contour plots for the medium model. The unit is Pa relative to an atmospheric pressure

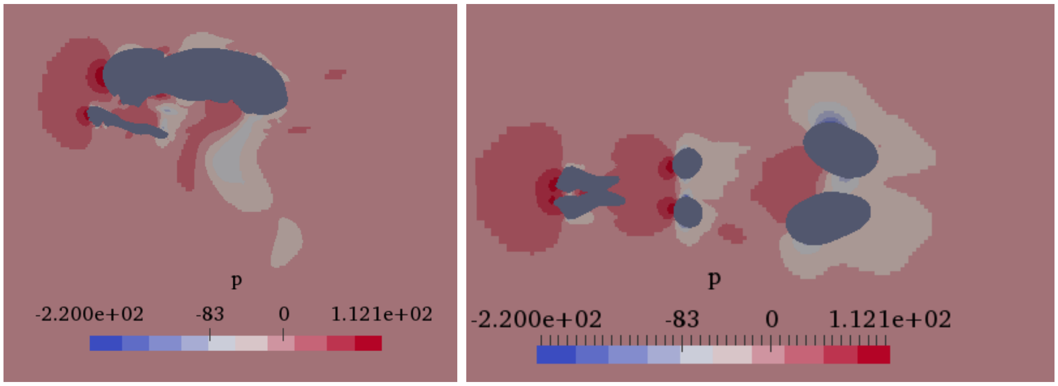

(a) Section view from the side

(b) Section view from the top

Figure 5.11: Pressure contour plots for the fine model. The unit is Pa relative to an atmospheric pressure

5.2 Parameter study

The chosen method of finding the optimal posture is known as a Parameter study, and the parameters of the study, also known as design variables concerning optimisation terminology, is the elbow extension, shoulder abduction and external shoulder rotation, which are all illustrated in Figure 5.12. A discrete number of models with varying values of the design variables are modelled in Blender using skeleton rigging. Further, a regression model is fitted to the simulation results, thus, creating a continuous function describing the drag force as a function of the design variables. The parameters are renamed based on their resulting position changes. Thus, we will refer to shoulder abduction as the distance between elbows, and external shoulder rotation as the distance between hands, while elbow extension keeps its original name.

Our first step in the parameter study is to identify the boundaries, i.e. the maximum and minimum values of the parameters we are studying, inside the domain containing the feasible postures, i.e. the postures which satisfies the regulations as defined by the International Cycling Union (UCI). As we consider the cyclist seat in a fixed position, the only limitation of the cyclist posture is the position of the handlebars. According to UCI regulations (Clarification Guide of the UCI Technical Regulation, 2007, p. 31), the handlebars must be within the area defined by the lines A, B, C and D presented in Figure 5.13. The maximum distance between the hands is set equal to the width of the handlebars of an example cycle, which for the Hart cyclist model is just outside of shoulder width, while the minimum distance between the hands is set to the hands touching each other. The same maximum and minimum values are also set for the distance between elbows. As for the elbow extension, the maximum value is set to when the hand is in contact with line C, as defined in Figure 5.13 and the minimum value is set to when the hands are in contact with line B, also defined in Figure 5.13. Based on the author's best judgement, four modifications of each parameter is sufficient to discover the trends of drag in posture modifications. Hence, four parameter values are modelled, with equal distance between each parameter value, and half of that distance between the boundaries of the domain, as shown in Figure 5.14. For the sake of simplicity, the minimum and maximum value of each parameter are set equal to zero and one, respectively. By having three different parameters, which each being modelled for four different values, a total of $4 \cdot 4 \cdot 4 = 64$ models are modelled. These models were modelled using a script, ensuring a consistent parameter change, and, of course, visually inspected to ensure a satisfying result. The hands have a neutral position, which remains constant relative to the corresponding forearm, for all 64 models. The models are generated using the first approach described in Section 5.1, i.e. with only four bones, and they are simulated using the computational setup presented in Chapter 4. An overview of each of these models are presented in Appendix A, and corresponding simulation results are presented numerically in Table 5.2.

Our next step in the parameter study is to construct a regression model for the simulation results of drag, and thus, create a continuous function describing the drag force as a function of our design variables. Since we base the regression model on the simulations results of the 64 cyclist-models, and these models are constructed by having four modifications of three parameters, it makes sense to base the regression model on a fourth order polynomial of three variables. Thus, it takes the following general form

$$
\begin{aligned}
D_F(E_p, E_e, H_p) = a_1 &+ a_2 E_p + a_3 E_e + a_4 H_p + a_5 E_p E_e + a_6 E_e H_p + a_7 E_p H_p + a_8 E_p^2 \\
&+ a_9 E_e^2 + a_{10} H_p^2 + a_{11} E_p^3 + a_{12} E_e^3 + a_{13} H_p^3 + a_{14} E_p^2 E_e + a_{15} E_p E_e^2 \\
&+ a_{16} E_p^2 H_p + a_{17} H_p^2 E_p + a_{18} E_e^2 H_p + a_{19} H_p^2 E_e + a_{20} E_p E_e H_p + a_{21} E_p^4 \\
&+ a_{22} E_e^4 + a_{23} H_p^4 + a_{24} E_p^2 E_e H_p + a_{25} E_p E_e^2 H_p + a_{26} E_p E_e H_p^2 \\
&+ a_{27} E_p^3 E_e + a_{28} E_p^3 H_p + a_{29} E_e^3 E_p + a_{30} E_e^3 H_p + a_{31} H_p^3 E_p + a_{32} H_p^3 E_e \\
&+ a_{33} E_p^2 E_e^2 + a_{34} E_e^2 H_p^2 + a_{35} E_p^2 H_p^2
\end{aligned}
\tag{5.1}
$$

where D_F is the drag force, E_p is the distance between the elbows, E_e is the elbow extension, H_p is the distance between the hands, and $a_i,\ i = 1:35$ are coefficients.

The coefficients of Equation (5.1) are determined by multiple linear regression to be

$$\begin{bmatrix} a_1 & a_2 & a_3 & a_4 & a_5 & a_6 & a_7 \\ a_8 & a_9 & a_{10} & a_{11} & a_{12} & a_{13} & a_{14} \\ a_{15} & a_{16} & a_{17} & a_{18} & a_{19} & a_{20} & a_{21} \\ a_{22} & a_{23} & a_{24} & a_{25} & a_{26} & a_{27} & a_{28} \\ a_{29} & a_{30} & a_{31} & a_{32} & a_{33} & a_{34} & a_{35} \end{bmatrix} = \begin{bmatrix} 18.46 & -3.47 & 12.57 & -3.69 & -20.80 & 1.66 & 42.29 \\ 12.94 & -11.59 & 5.10 & 0 & 0 & 0 & 14.31 \\ 13.62 & -68.74 & -31.46 & -1.19 & -2.44 & -15.05 & -6.42 \\ 1.00 & -4.14 & 19.27 & 10.14 & -13.56 & 7.03 & 24.25 \\ 9.31 & 5.47 & 10.93 & 14.24 & -25.46 & -11.94 & 24.26 \end{bmatrix}$$

Equation (5.1) with the numerical values for the corresponding coefficients are plotted and compared with the data its fitted to in Figures 5.15 and 5.16. Additionally, contour plots of the same equation for a total of 11 different distances between elbows E_p are presented in Figures 5.17-5.19, revealing much of the three dimensional (3D) trends of the regression model. As seen in these figures, the regression model is highly non-linear. Based on the regression model, the following observations are made regarding postures

- When the distance between elbows is in the range of 0.125-0.5625, the preferred elbow extension and distance between hands is 0.125
- When the distance between elbows is in the range of 0.5625-0.6875, the preferred elbow extension and distance between hands is either 0.875 and 0.125 or in the range of ≈0.56-0.76 and ≈0.68-0.875, respectively
- When the distance between elbows is in the range of 0.75-0.875, the preferred elbow extension and distance between hands is 0.125 and ≈0.625-0.875, respectively

The simulation results support the observations made based on the regression model. However, making the observations just based on the simulations results would be considered much more challenging than of making them based on the regression model. Hence, the regression model is confirmed to be useful.

In principle, the global minimum of the regression model corresponds to the optimal cyclist posture. Several advanced approaches can be utilised to obtain the global minimum. However, as we are discussing the posture of a human cyclist, we have to recognise that accuracy of a posture is limited. Hence, the drag force is calculated for a discrete number of positions. By dividing each parameter into eight equally distanced modifications, the drag force for a total of $8^3 = 512$ postures are calculated. The postures with the lowest drag force and corresponding position are presented in Table 5.3 both according to the simulations results and the regression model. As seen in this table, the combination of minimum distance between elbows, -elbow extension, and -hands seem to be favourable posture both according to the simulations results and the regression model. The regression model was unable to detect a global minimum for which the simulations results had not revealed in advance. However, it did identify several local minimums. Based on results presented in the latter table, a small elbow extension E_e seem to be the most dominant parameter value.

Velocity contour plots of the four simulated postures that experience the least drag and the posture which suffers the greatest drag force are presented in Figures 5.20-5.24. The corresponding pressure contour plots are presented in Figures 5.25-5.29. By comparing the velocity- and pressure contour plots of the three models with the least drag, i.e. Figures 5.20, 5.21, 5.22, 5.25, 5.26 and 5.27, it is seen that the corresponding differences are negligible, except for the size of the wake in Figure 5.20a being slightly reduced. As is not the case by including the model with the fourth least drag in the comparison, i.e. Figures 5.23 and 5.28. The flow characteristics in terms of velocity and pressure of the latter model is noticeable different from that of the models with the least, second- and third least drag. The largest differences in the velocity contour plots are seen in the wake and the zone between the elbows and thighs, and the largest difference in the pressure contour plots are seen in the zone between the hands and the elbows. Further, by including the posture which suffered the greatest drag force, i.e. Figures 5.24 and 5.29, much bigger differences are seen. Most notable is perhaps the enlarged wake seen in the velocity contour plot of Figure 5.24. Additionally, streamline- and surface

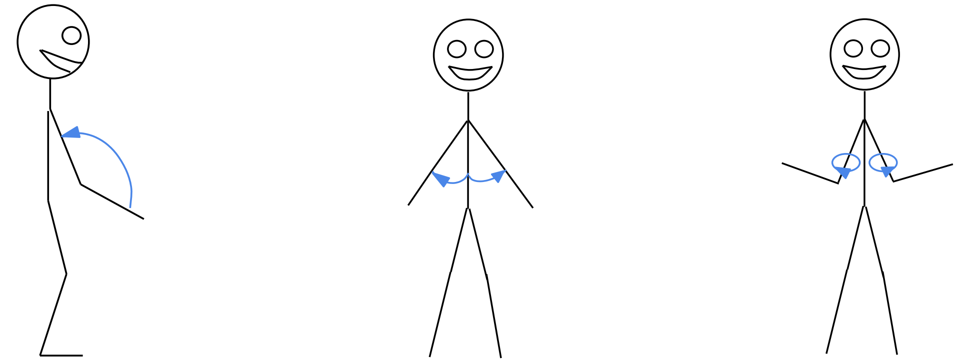

(a) Illustration of elbow extension (b) Illustration of shoulder abduction (c) Illustration of external shoulder rotation

Figure 5.12: Illustrations of the design variables

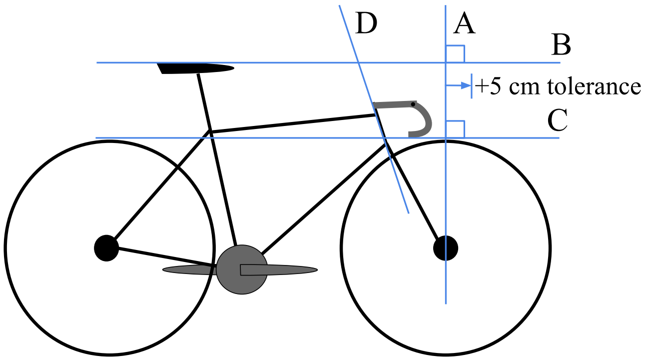

Figure 5.13: UCI regulations on cycle handlebar position

pressure plots for the model with the least and greatest drag are presented in Figures 5.30 and 5.31, respectively. By comparing the streamline plots, i.e. Figures 5.30a and 5.31a, it is shown that the wake of the model with least drag stabilises much sooner than that of the model with the greatest drag. Additionally, the model with the least drag is much more streamlined than that of the model with the greatest drag. Further, by comparing the surface pressure plots of the same models, i.e. Figures 5.30b and 5.31b, it is seen that the model with the greatest drag force have a higher magnitude of pressure on the visible part of the fingers and the front side of the thighs. The model with the least drag, has a lower magnitude of pressure at the outer side of the thigh, compared to the model with greatest drag.

Figure 5.14: This figure shows the numerical values of the four modelled positions $p_i, \ i = 1 : 4$ for each parameter, as well as the minimum (min.) and maximum (max.) position with corresponding numerical values

$E_p = 0.125$

E_e	H_p							
	0.125		0.375		0.625		0.875	
	avg. F_D	σ_{std}	*avg.* F_D	σ_{std}	*avg.* F_D	σ_{std}	*avg.* F_D	σ_{std}
0.125	19.59	0.0201	19.44	0.0574	20.70	0.1983	20.07	0.1214
0.375	20.44	0.0855	21.31	0.1690	21.52	0.1337	22.02	0.1596
0.625	21.58	0.0733	21.36	0.1573	21.44	0.1940	23.06	0.2785
0.875	20.77	0.0569	21.45	0.0954	22.12	0.1166	22.61	0.0758

$E_p = 0.375$

E_e	H_p							
	0.125		0.375		0.625		0.875	
	avg. F_D	σ_{std}	*avg.* F_D	σ_{std}	*avg.* F_D	σ_{std}	*avg.* F_D	σ_{std}
0.125	19.86	0.2061	20.58	0.2859	20.33	0.0518	20.98	0.1125
0.375	20.78	0.1501	21.37	0.0643	21.85	0.0757	22.15	0.0777
0.625	21.05	0.1012	20.89	0.0367	21.36	0.0782	21.63	0.2066
0.875	21.41	0.0773	21.41	0.1070	21.00	0.0389	21.82	0.1957

$E_p = 0.625$

E_e	H_p							
	0.125		0.375		0.625		0.875	
	avg. F_D	σ_{std}	*avg.* F_D	σ_{std}	*avg.* F_D	σ_{std}	*avg.* F_D	σ_{std}
0.125	21.24	0.1166	21.89	0.1673	21.06	0.1345	20.88	0.1800
0.375	21.35	0.1157	21.07	0.0312	20.81	0.1134	21.22	0.1050
0.625	21.64	0.0417	21.40	0.0585	21.17	0.0766	20.89	0.1491
0.875	21.30	0.0377	22.31	0.2511	22.06	0.1596	20.97	0.0960

$E_p = 0.875$

E_e	H_p							
	0.125		0.375		0.625		0.875	
	avg. F_D	σ_{std}	*avg.* F_D	σ_{std}	*avg.* F_D	σ_{std}	*avg.* F_D	σ_{std}
0.125	22.02	0.1203	20.99	0.0827	20.86	0.1157	21.17	0.0918
0.375	23.44	0.1864	22.00	0.0850	21.56	0.0496	21.72	0.1126
0.625	22.12	0.0527	22.26	0.1772	22.27	0.1286	21.68	0.0731
0.875	22.84	0.0548	22.63	0.0716	21.60	0.0719	23.04	0.0793

Table 5.2: The simulation results for drag and the corresponding standard deviation. E_p is the distance between the elbows, E_e the elbow extension, and H_p is the distance between the hands. *avg.* F_D is the average drag force between iteration 3500 and 5000 in unit N, and σ_{std} is the standard deviation of the drag force between iteration 4500 and 5000

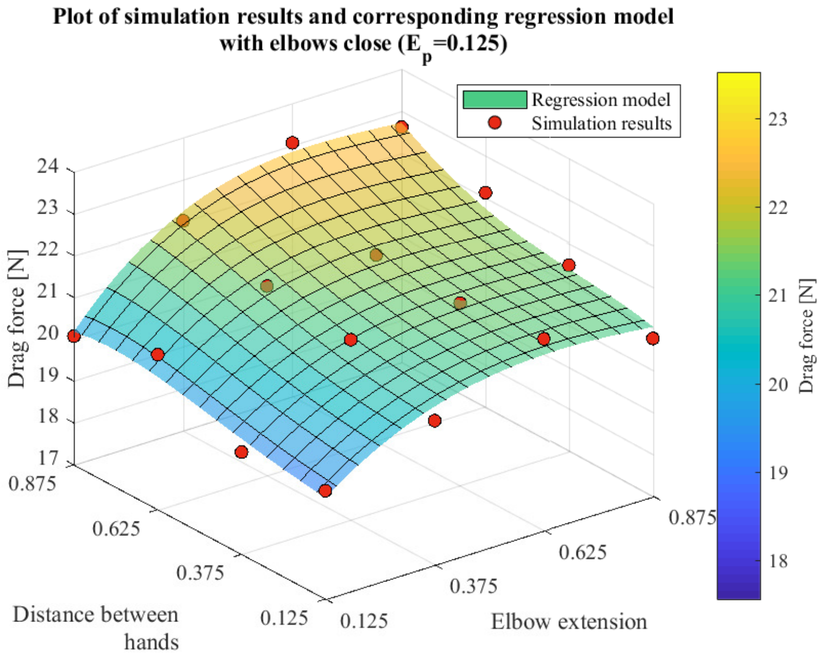

(a) With elbows close, $E_p = 0.125$

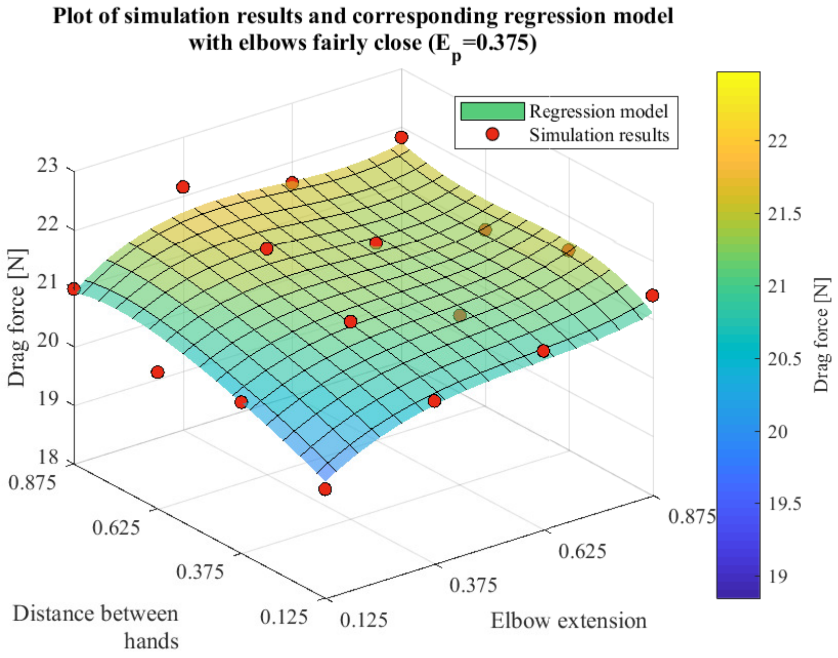

(b) With elbows fairly close, $E_p = 0.375$

Figure 5.15: Selected simulation results of the drag from Table 5.2 compared with the regression model at the corresponding distance between elbows E_p

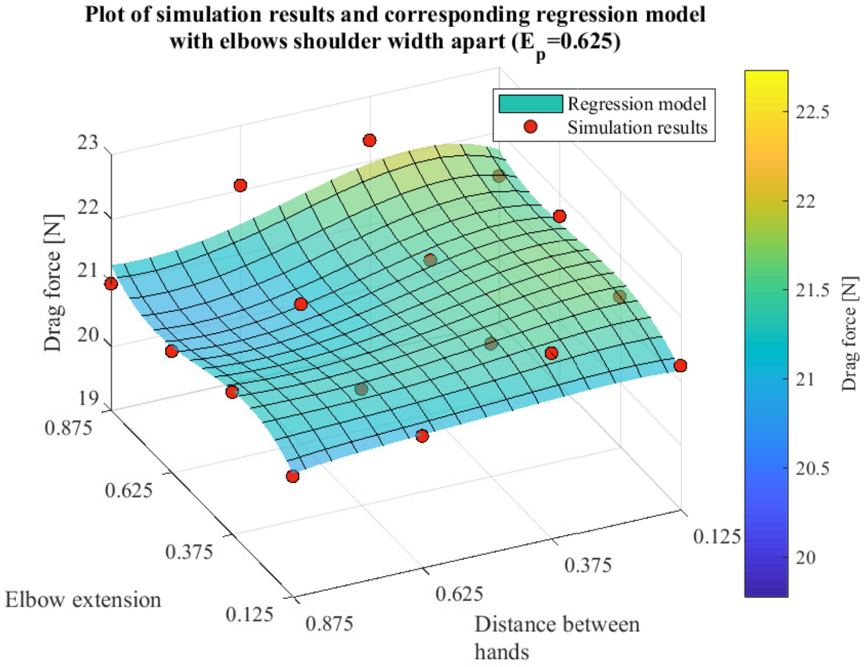

(a) With elbows shoulder width apart, $E_p = 0.625$

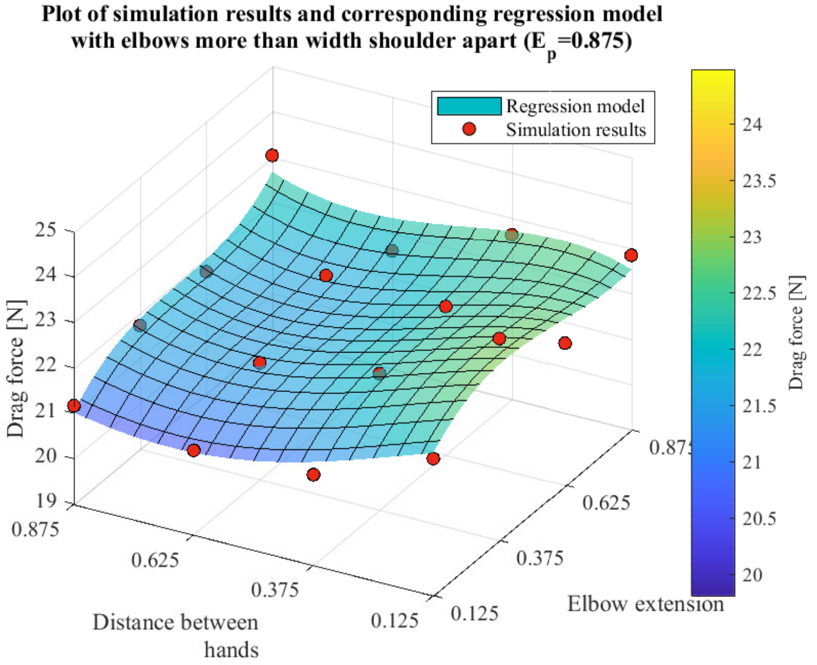

(b) With elbows more than shoulder width apart, $E_p = 0.875$

Figure 5.16: Selected simulation results of the drag from Table 5.2 compared with the regression model at the corresponding distance between elbows E_p

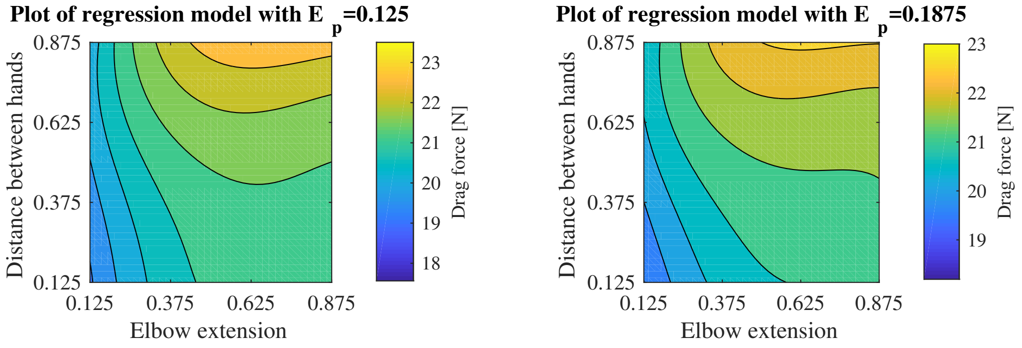
Plot of regression model with E p=0.125

Plot of regression model with E p=0.1875

(a) Distance between elbows $E_p = 0.125$ (b) Distance between elbows $E_p = 0.1875$

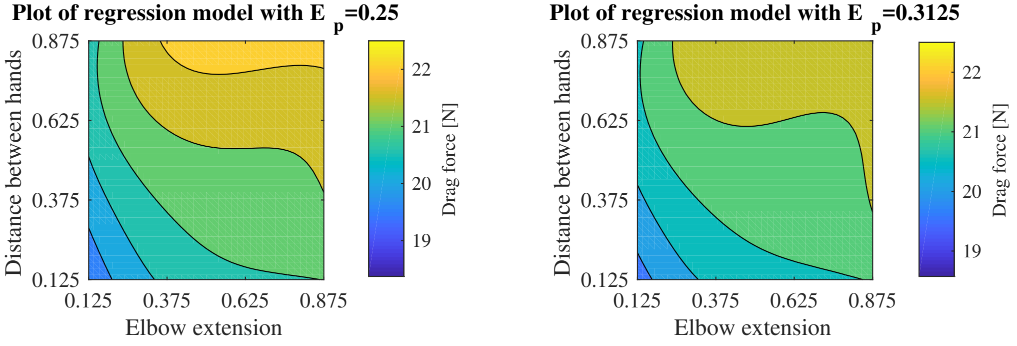
Plot of regression model with E p=0.25

Plot of regression model with E p=0.3125

(c) Distance between elbows $E_p = 0.25$ (d) Distance between elbows $E_p = 0.3125$

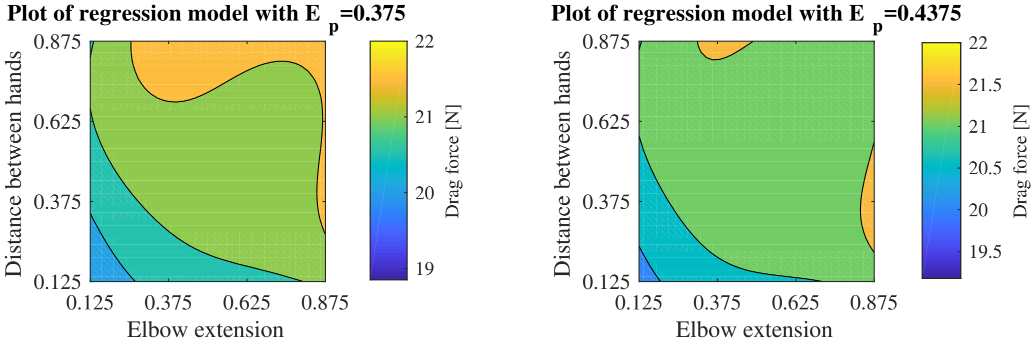
Plot of regression model with E p=0.375

Plot of regression model with E p=0.4375

(e) Distance between elbows $E_p = 0.375$ (f) Distance between elbows $E_p = 0.4375$

Figure 5.17: Contour plots of the regression model for a discrete number of distances between elbows E_p

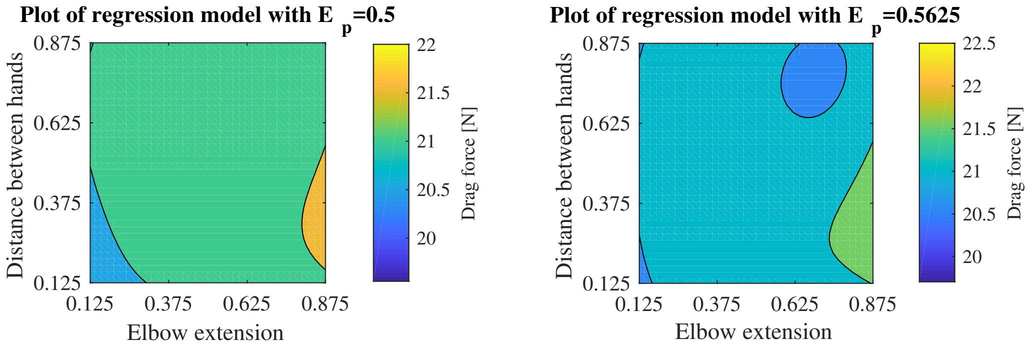

(a) Distance between elbows $E_p = 0.5$

(b) Distance between elbows $E_p = 0.5625$

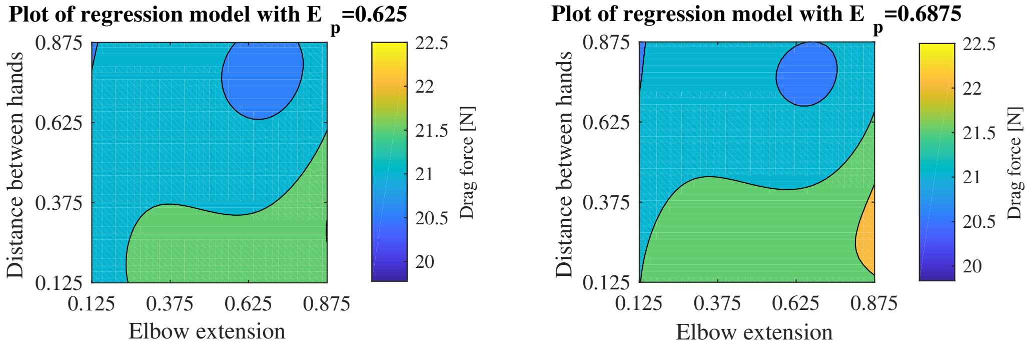

(c) Distance between elbows $E_p = 0.625$

(d) Distance between elbows $E_p = 0.6875$

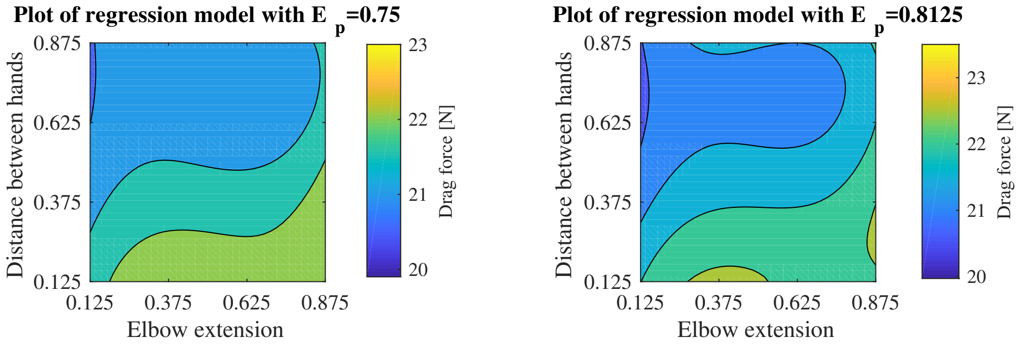

(e) Distance between elbows $E_p = 0.75$

(f) Distance between elbows $E_p = 0.8125$

Figure 5.18: Contour plots of the regression model for a discrete number of distances between elbows E_p

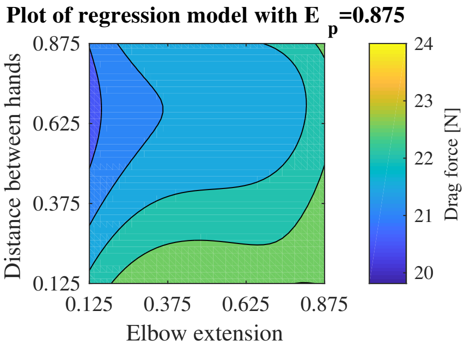

Figure 5.19: Contour plots of the regression model with distance between elbows $E_p = 0.875$

According to the simulation results				According to the regression model			
F_D	E_p	E_e	H_p	F_D	E_p	E_e	H_p
19.442	0.125	0.125	0.375	19.434	0.125	0.125	0.125
19.589	0.125	0.125	0.125	19.439	0.135	0.125	0.125
19.858	0.375	0.125	0.125	19.443	0.125	0.125	0.135
20.075	0.125	0.125	0.875	19.446	0.145	0.125	0.125
20.326	0.375	0.125	0.625	19.451	0.135	0.125	0.135
20.441	0.125	0.375	0.125	19.453	0.125	0.125	0.145
20.579	0.375	0.125	0.375	19.455	0.155	0.125	0.125
20.7	0.125	0.125	0.625	19.459	0.145	0.125	0.135
20.765	0.125	0.875	0.125	19.462	0.135	0.125	0.145
20.777	0.375	0.375	0.125	19.463	0.125	0.125	0.155

Table 5.3: The ten postures with least drag according to the simulation results and the regression model

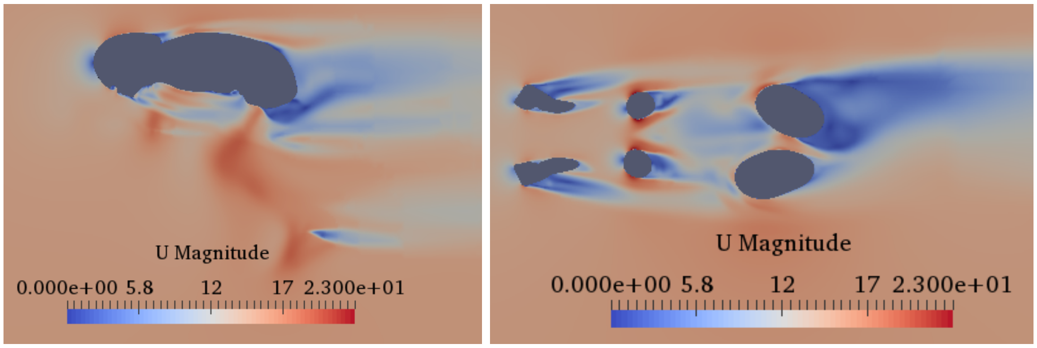

(a) Section view from the side (b) Section view from the top

Figure 5.20: Velocity contour plots for the posture with the least drag, i.e. $E_p = 0.125$, $E_e = 0.125$ and $H_p = 0.375$. The unit is m/s

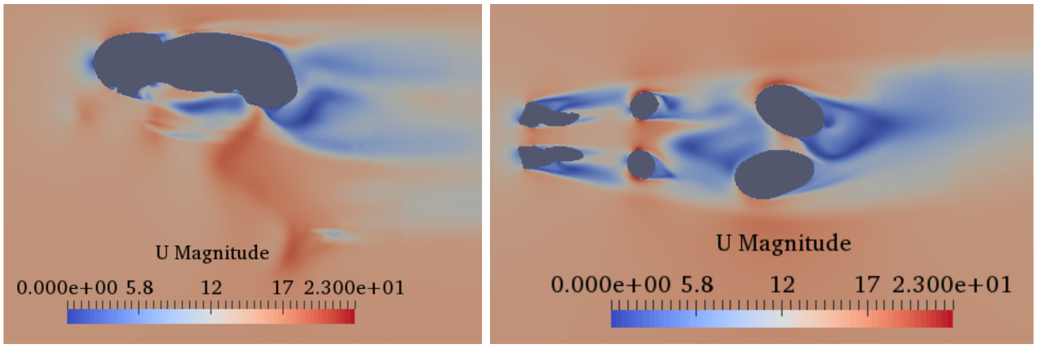

(a) Section view from the side (b) Section view from the top

Figure 5.21: Velocity contour plots for the posture with the second least drag, i.e. $E_p = 0.125$, $E_e = 0.125$ and $H_p = 0.125$. The unit is m/s

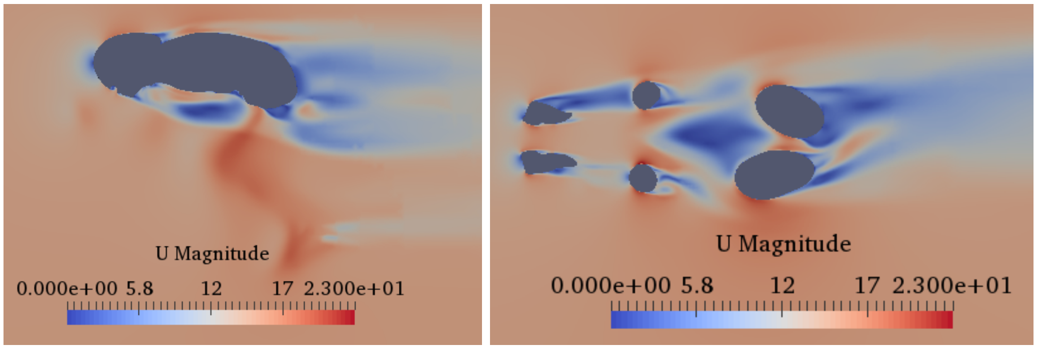

(a) Section view from the side (b) Section view from the top

Figure 5.22: Velocity contour plots for the posture with the third least drag, i.e. $E_p = 0.375$, $E_e = 0.125$ and $H_p = 0.125$. The unit is m/s

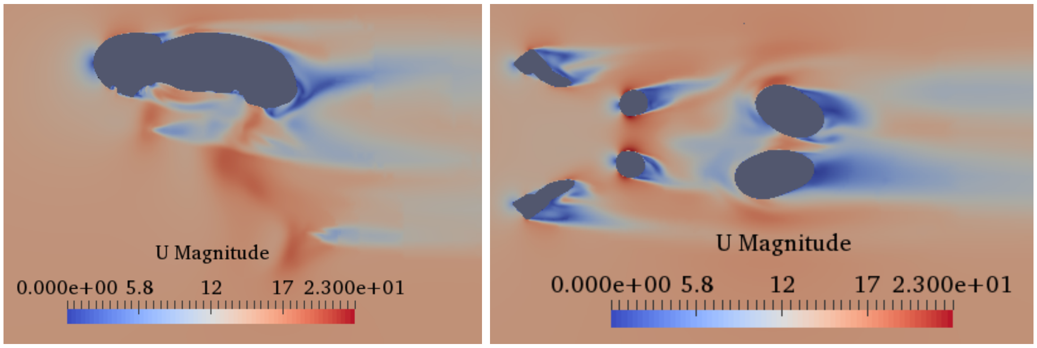

(a) Section view from the side (b) Section view from the top

Figure 5.23: Velocity contour plots for the posture with the fourth least drag, i.e. $E_p = 0.125$, $E_e = 0.125$ and $H_p = 0.875$. The unit is m/s

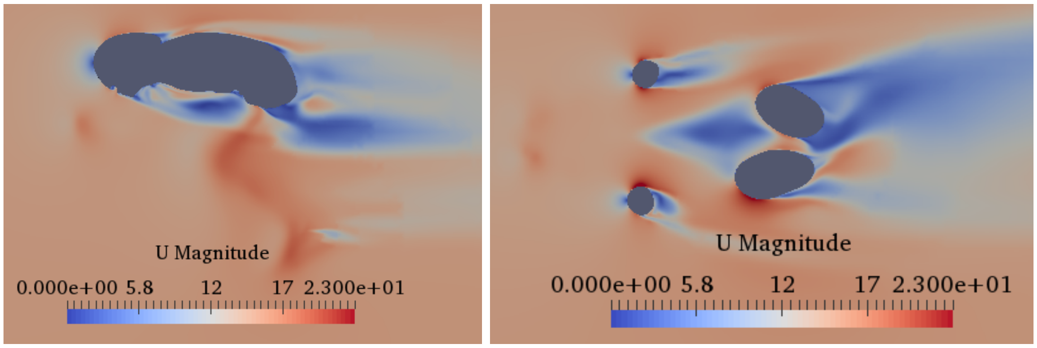

(a) Section view from the side (b) Section view from the top

Figure 5.24: Velocity contour plots for the posture with the greatest drag, i.e. $E_p = 0.875$, $E_e = 0.375$ and $H_p = 0.125$. The unit is m/s

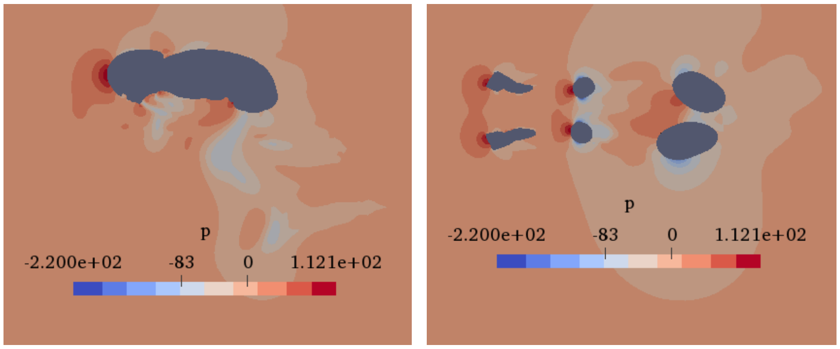

(a) Section view from the side (b) Section view from the top

Figure 5.25: Pressure contour plots for the posture with the least drag, i.e. $E_p = 0.125$, $E_e = 0.125$ and $H_p = 0.375$. The unit is Pa relative to an atmospheric pressure

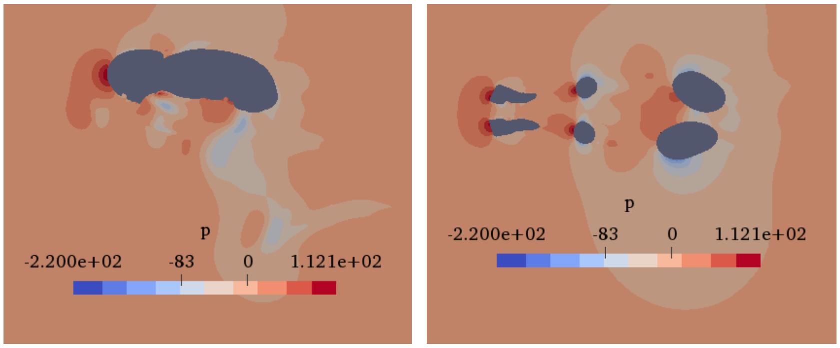

(a) Section view from the side (b) Section view from the top

Figure 5.26: Pressure contour plots for the posture with the second least drag, i.e. $E_p = 0.125$, $E_e = 0.125$ and $H_p = 0.125$. The unit is Pa relative to an atmospheric pressure

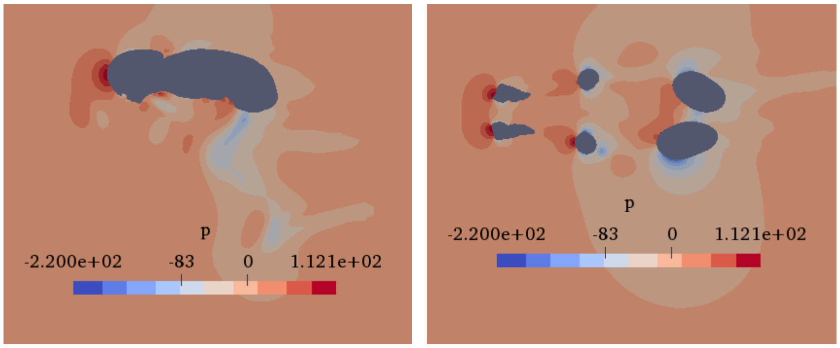

(a) Section view from the side (b) Section view from the top

Figure 5.27: Pressure contour plots for the posture with the third least drag, i.e. $E_p = 0.375$, $E_e = 0.125$ and $H_p = 0.125$. The unit is Pa relative to an atmospheric pressure

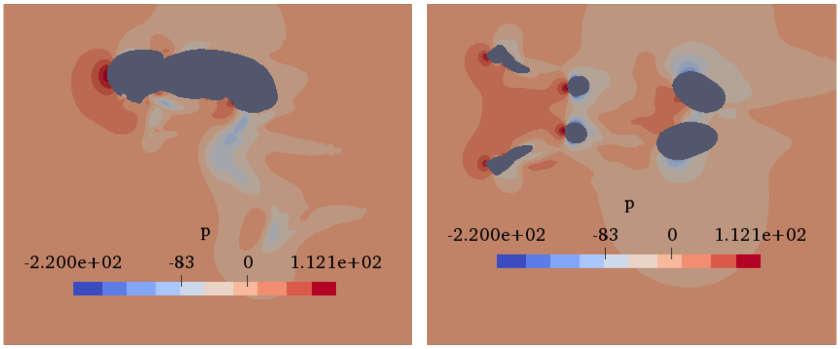

(a) Section view from the side (b) Section view from the top

Figure 5.28: Pressure contour plots for the posture with the fourth least drag, i.e. $E_p = 0.125$, $E_e = 0.125$ and $H_p = 0.875$. The unit is Pa relative to an atmospheric pressure

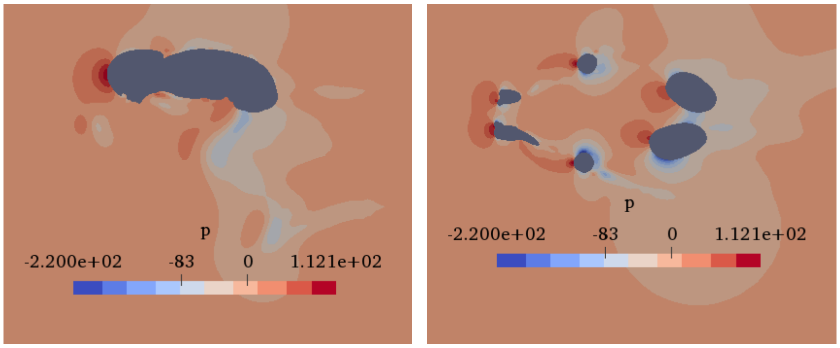

(a) Section view from the side (b) Section view from the top

Figure 5.29: Pressure contour plots for the posture with the greatest drag, i.e. $E_p = 0.875$, $E_e = 0.375$ and $H_p = 0.125$. The unit is Pa relative to an atmospheric pressure

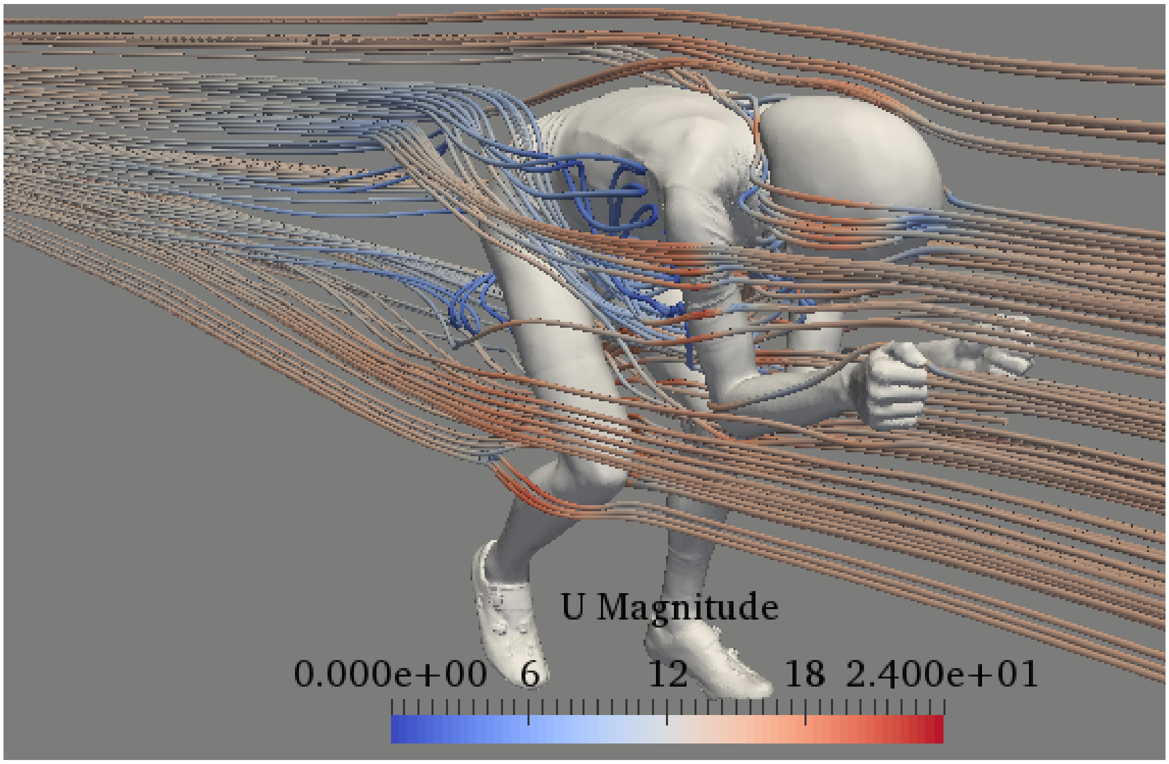

(a) Streamline plot. The unit is m/s

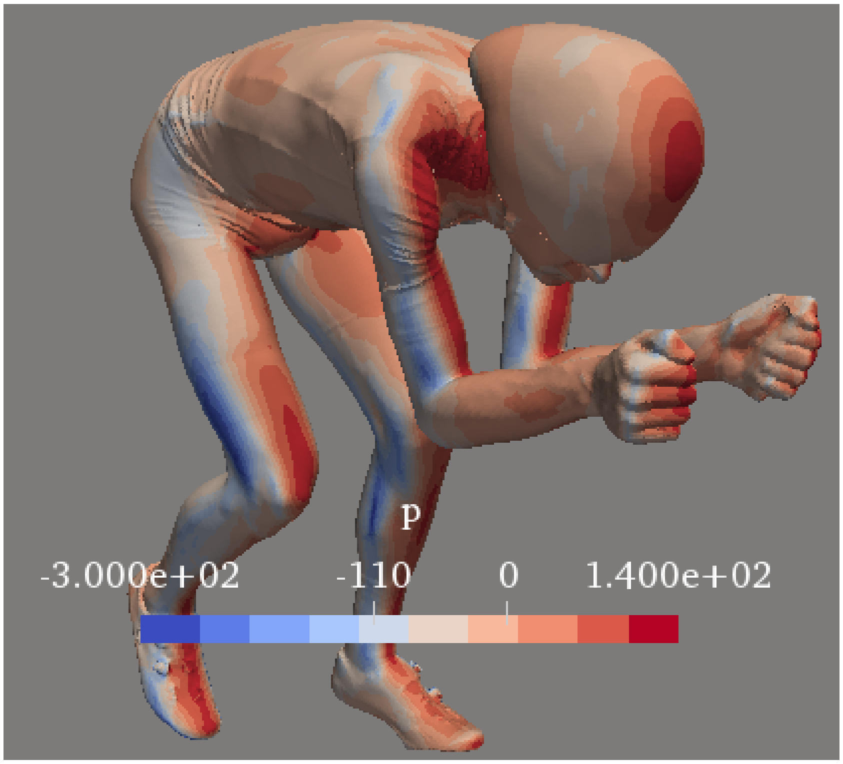

(b) Surface pressure plot. The unit is Pa relative to an atmospheric pressure

Figure 5.30: **Streamline- and surface pressure plot for the posture with the greatest drag, i.e.** $E_p = 0.875$**,** $E_e = 0.375$ **and** $H_p = 0.125$

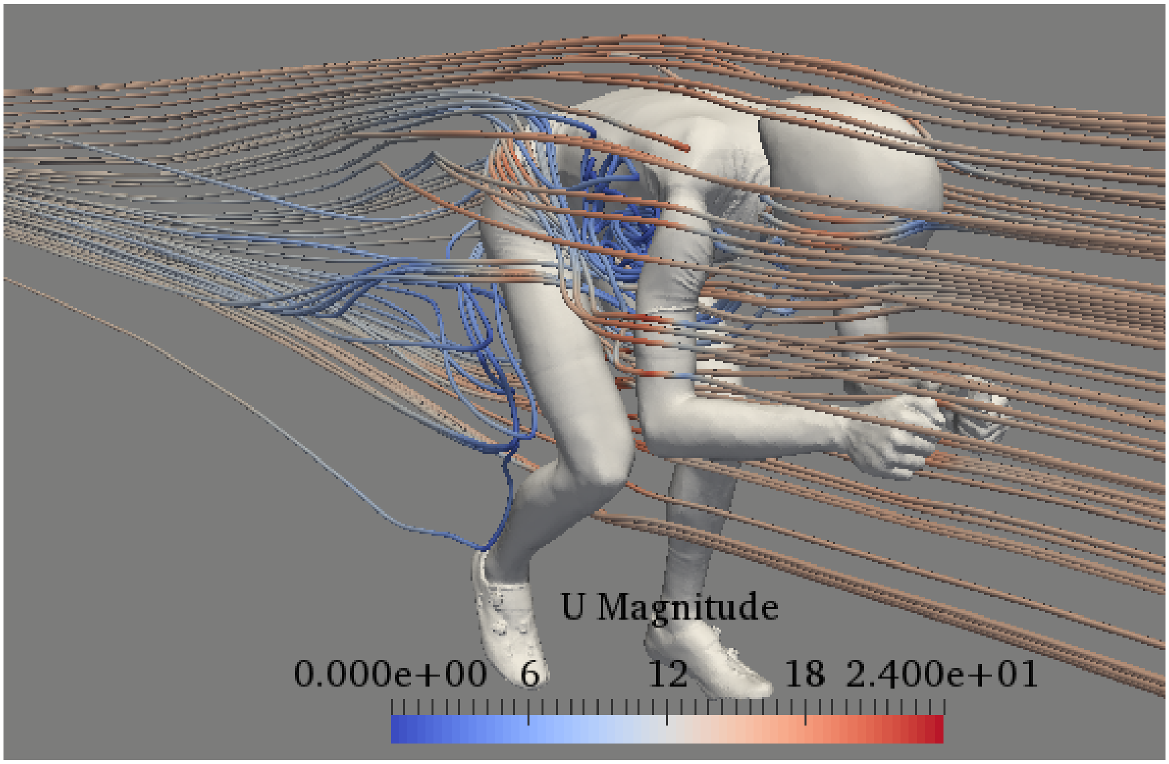

(a) Streamline plot. The unit is m/s

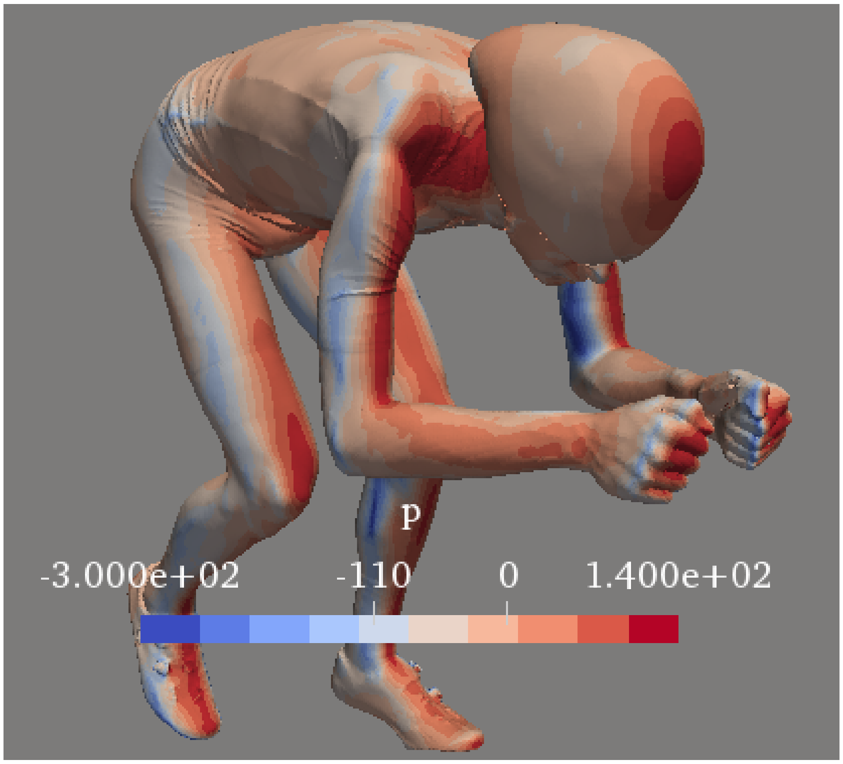

(b) Surface pressure plot. The unit is Pa relative to an atmospheric pressure

Figure 5.31: Streamline- and surface pressure plot for the posture with the greatest drag, i.e. $E_p = 0.875$, $E_e = 0.375$ and $H_p = 0.125$

Chapter 6

Conclusions and recommendations

In this thesis, a procedure of optimising the posture of a cyclist based on a single 3D scanning is developed and executed. The entire procedure can and is executed using open-source software only.

The computational setup is validated by testing it on simpler geometry, a sphere, for which extensive experimental studies are available for. The sphere was simulated at $Re = 10^4$ and $Re = 10^6$. The simulation for $Re = 10^4$ concerning drag shows excellent agreement with experimental studies performed by Achenbach (1974). Additionally, the separation point has excellent compliance with results obtained by Jones & Clarke (2008) which used commercial simulation software. The simulation results for $Re = 10^6$ have reasonable agreement with experimental studies performed by Achenbach (1972) concerning the drag force and the separation point.

Five 3D scanned postures of the Team Sky athlete Tao Geoghegan Hart are simulated, and by comparing AC_D of the result with similar models simulated in the literature, the AC_D of present results are confirmed to be realistic. By comparing the relative change in drag of the five scanned postures, the results are confirmed to have reasonable compliance with those simulated by Dr Luca Oggiano which used a commercial meshing and -simulation software.

For the optimisation procedure, the posture modifications are made using skeleton rigging and include the distance between elbows, elbow extension and distance between hands. The corresponding minimum and maximum values of these modifications are set according to regulations of UCI. Simulation results show that a small distance between elbows, minimum elbow extension and any distance between hands, is the favourable combination for reducing the drag force. The elbow extension seems to be the most crucial parameter, secondly the distance between elbows, and then, the distance between the hands. Additionally, a cyclist posture which experiences a small drag force is also characterised by a narrow wake, a small A and a streamlined flow.

A regression model is constructed based on the simulation results of optimisation. This regression model did not reveal any global minimums for which the simulation results had not revealed in advance, yet, proved itself useful when analysing the trends of between posture and drag. These trends were supported by the simulations results and are

- When the distance between elbows is in the range of 0.125-0.5625, the preferred elbow extension and distance between hands is 0.125
- When the distance between elbows is in the range of 0.5625-0.6875, the preferred elbow extension and distance between hands is 0.875 and 0.125, or ≈0.56-0.76 and ≈0.68-0.875, respectively
- When the distance between elbows is in the range of 0.75-0.875, the preferred elbow extension and distance between hands is 0.125 and ≈0.625-0.875, respectively

6.1 Recommendations

In future executions of the procedure developed in this thesis, the author recommends modelling the postures of which parameters are at the boundaries of the domain defined by UCI. Thus, increasing the domain of the regression model without utilising extrapolation. Further, if the cyclist model is similar to the one optimised in this theses, a higher density of postures within the region with minimal elbow extension is recommended, as this is confirmed to be the region with favourable postures in this thesis.

Further work of this research is to validate the postures which by CFD experienced the least drag force in either wind-tunnel or time-trial experiments.

Bibliography

[1] Achenbach, E. (1972). “Experiments on the flow past spheres at very high Reynolds numbers” , J. *Fluid Mech.*, 54, pp. 565-575.

[2] Achenbach, E. (1974). “Vortex Shedding from Spheres”. *Journal of Fluid Mechanics*, 62, 209-221.

[3] Alam, F., Chowdhury, H., Wei, H.Z., Mustary, I. & Zimmer, G. (2014). “Aerodynamics of ribbed bicycle racing helmets”. *Procedia Eng., Eng. Sport 10 (72)*, pp. 691–696.

[4] Barry, N., Burton, D., Sheridan, J., Thompson, M. & Brown, N.A. (2014). “Aerodynamic performance and riding posture in road cycling and triathlon”. *Proc. Instit. Mech. Eng., Part P: J. Sports Eng. Technol.*

[5] Beaumont, F., Taiar, R., Polidori, G., Trenchard, H. & Grappe, F. (2018). “Aerodynamic study of time-trial helmets in cycling racing using CFD analysis”. *Journal of Biomechanics*. 67, pp. 1–8.

[6] Blocken, B., Defraeye, T., Koninckx, E., Carmeliet, J. & Hespel, P. (2013). “CFD simulations of the aerodynamic drag of two drafting cyclists”. *Computers* & *Fluids*. 71, pp. 435–445.

[7] Blocken, B. & Toparlar, Y. (2015). “A following car influences cyclist drag: CFD simulations and wind tunnel measurements”. *J. Wind Eng. Ind. Aerodyn.* 145 (July 2015) pp. 178–186.

[8] Brownlie, L., Ostafichuk, P., Tews, E., Muller, H., Briggs, E. & Franks, K. (2010). “The wind-averaged aerodynamic drag of competitive time trial cycling helmets”. *Procedia Eng., Eng. Sport 8 – Eng. Emotion 2*, pp. 2419–2424.

[9] CFD Direct. (n.d.). “OpenFOAM v5 User Guide: 5.4 Mesh generation with snappyHexMesh”. Accessed at 20.3.2018 through: *https://cfd.direct/openfoam/user-guide/snappyhexmesh/*

[10] Chabroux, V., Barelle, C. & Favier, D. (2008). “Aerodynamics of time trial bicycle helmets (P226)”. *In: The Engineering of Sport 7. Springer Paris*, pp. 401–410.

[11] Chowdhury, H., Alam, F. & Subic, A. (2010). “Aerodynamic performance evaluation of sports textile”. *Eng. Sport 8 – Eng. Emotion* 2, pp. 2517–2522.

[12] Chowdhury, H., Alam, F. & Khan, K. (2011). “An experimental study of bicycle aerodynamics”. *Int. J. Mech. Mater. Eng.* 6, pp. 269–274.

[13] Constantinescu, G., Chapelet, M. & Squires, K. (2003). “Turbulence Modeling Applied to Flow over a Sphere”. *AIAA Journal*. Vol. 41, No. 9, September 2003.

[14] Constantinescua, G. & Squires, K. (2004). “Numerical investigations of flow over a sphere in the subcritical and supercritical regimes ”. *Physics of Fluids*. vol. 16, no. 5, May 2004.

[15] Croucha, T.N., Burtona, D., Venninga, J.A., Thompsona, M.C., Brown, N.A.T. & Sheridan, J. (2016). “A Comparison of the Wake Structures of Scale and Full-scale Pedalling Cycling Models”. *Procedia Engineering*. Vol. 147, (July 2016), pp. 13-19.

[16] Defraeye, T., Blocken, B., Koninckx, E., Hespel, P. & Carmeliet, J. (2010). "Aerodynamic study of different cyclist positions: CFD analysis and full-scale wind-tunnel tests". *Journal of Biomechanics.* 43, (January 2010), pp. 1262–1268.

[17] Ertesvåg, I. S. (2000). *Turbulent Strøyming og Forbrenning.* Trondheim: Tapir Akademisk Forlag.

[18] Fintelman, D.M., Hemida, H., Sterling, M. & Li, F.-X. (2015). "CFD simulations of the flow around a cyclist subjected to crosswinds". *J. Wind Eng. Ind. Aerodyn.* 144 (2015) pp. 31–41.

[19] García-López, J., Rodríguez-Marroyo, J. A, , Juneau C. E., Peleteiro, J., Martínez, A. C, & Villa, J. G. (2008). "Reference values and improvement of aerodynamic drag in professional cyclists". *Journal of Sports Sciences.* 26:3, pp .277-286.

[20] Grappe, F., Candau, R., Belli, A. & Rouillon, J.D. (1997). "Aerodynamic drag in field cycling with special reference to the Obree's position". *Ergonomics* 40, pp. 1299– 1311.

[21] Jeukendrup, A.E. & Martin, J. (2001). "Improving Cycling Performance". *Sports Med.* 31, pp. 559–569.

[22] Jones, D.A. & Clarke, D.B. (2008). "Simulation of Flow Past a Sphere using the Fluent Code". Australian Government, Deparment of Defence. Defence Science and Technology Organisation. DSTO-TR-2232.

[23] Kim, S.E. (2004). "Large Eddy Simulation Using Unstructured Meshes and Dynamic SubgridScale Turbulence Models", *34th AIAA Fluid Dynamics Conference and Exhibit*, Portland, Oregon, AIAA paper number 2004-2548.

[24] Lukes, R.A., Chin, S.B. & Haake, S.J. (2005). "The understanding and development of cycling aerodynamics". *Sports Eng.* 8, pp. 59–74.

[25] Millikan, C. B. & Klein, A. L. (1933). "The effect of turbulence. An investigation of maximum lift coefficient and turbulence in wind tunnels and in flight". *Aircraft Eng.* 5,169-174.

[26] Mustary, I., Chowdhury, H., Loganathan, B., Alharthi, M. & Alam, F. (2014). "Aerodynamic Efficiency and Thermal Comfort of Road Racing Bicycle Helmets", *19th Australasian Fluid Mechanics Conference*

[27] Oggiano, L., Troynikov, O., Konopov, I., Subic, A. & Alam, F. (2009). "Aerodynamic behaviour of single sport Jersey fabrics with different roughness and cover factors". *Sports Eng.* 12, 1–12.

[28] OpenFOAM a. (n.d.), *Standard solvers*, Accessed at 20.3.2018 through: *https://www.openfoam.com/documentation/user-guide/standard-solvers.php*

[29] OpenFOAM b. (n.d.), *k-omega Shear Stress Transport (SST)*, Accessed at 24.3.2018 through: *https://www.openfoam.com/documentation/cpp-guide/html/guide-turbulence-ras-k-omega-sst.html*

[30] Robertson, E. D. (2015). *Verification, validation, and implementation of numerical methods and models for OpenFOAM 2.0 for incompressible flow.* (Masters thesis). Mississippi, Mississippi State University.

[31] Versteeg, H. K. & Malalasekera W. (2007). *An Introduction to CFD Finite volume method.* 2nd ed. Glasgow: Pearson Education.

[32] von Kármán, Th. (1931), "Mechanische Ähnlichkeit und Turbulenz", *Nachrichten von der Gesellschaft der Wissenschaften zu Göttingen, Fachgruppe 1 (Mathematik)*, 5: 58–76 (also as: "Mechanical Similitude and Turbulence", *Tech. Mem. NACA*, no. 611, 1931).

[33] White, F. M. (2011). *Fluid Mechanics.* 7th ed. New York: McGraw Hill Higher Education.

[34] Wieselberger, C. (1922). "Weitere Feststellungen iiber die Gesetze des Flussigkeits- und Luftwiderstandes". *Phys.* 2. 23, 219-224.

Appendix

Contents of Appendix

A: The models of optimisation pictured

Models with elbows close
(elbow position = 0.125)

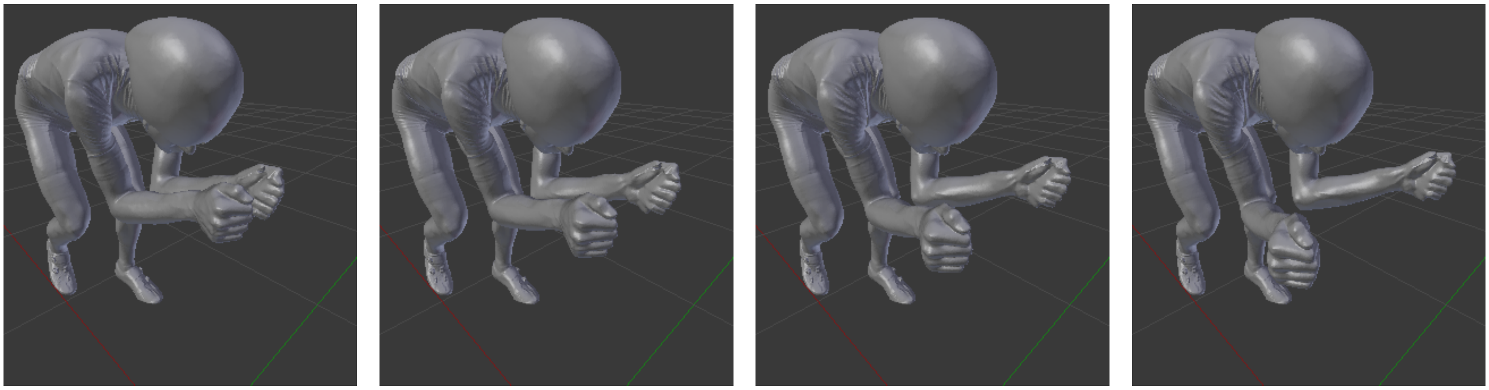

(a) Elbow extension = 0.125
Distance between hands = 0.125

(b) Elbow extension = 0.125
Distance between hands = 0.375

(c) Elbow extension = 0.125
Distance between hands = 0.625

(d) Elbow extension = 0.125
Distance between hands = 0.875

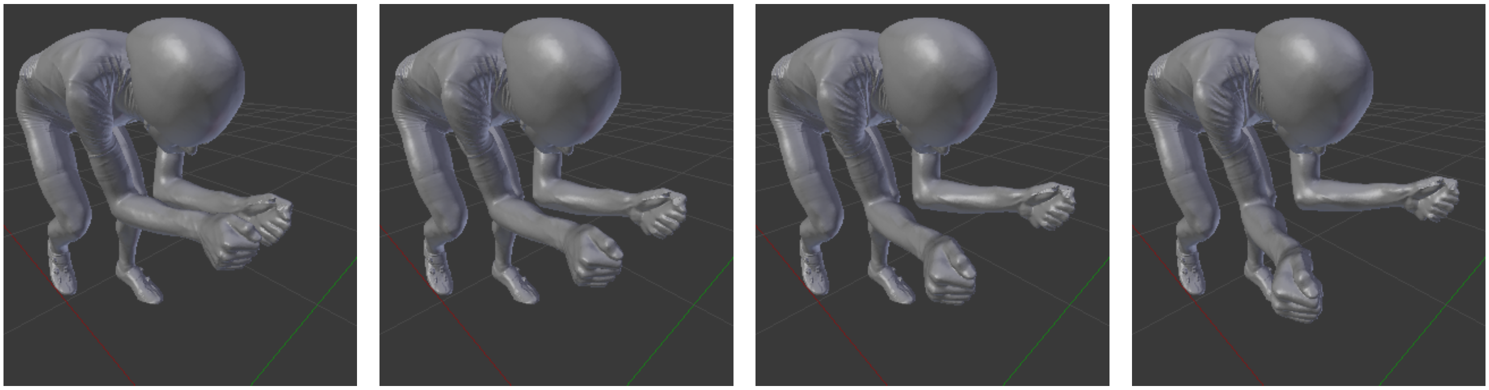

(e) Elbow extension = 0.375
Distance between hands = 0.125

(f) Elbow extension = 0.375
Distance between hands = 0.375

(g) Elbow extension = 0.375
Distance between hands = 0.625

(h) Elbow extension = 0.375
Distance between hands = 0.875

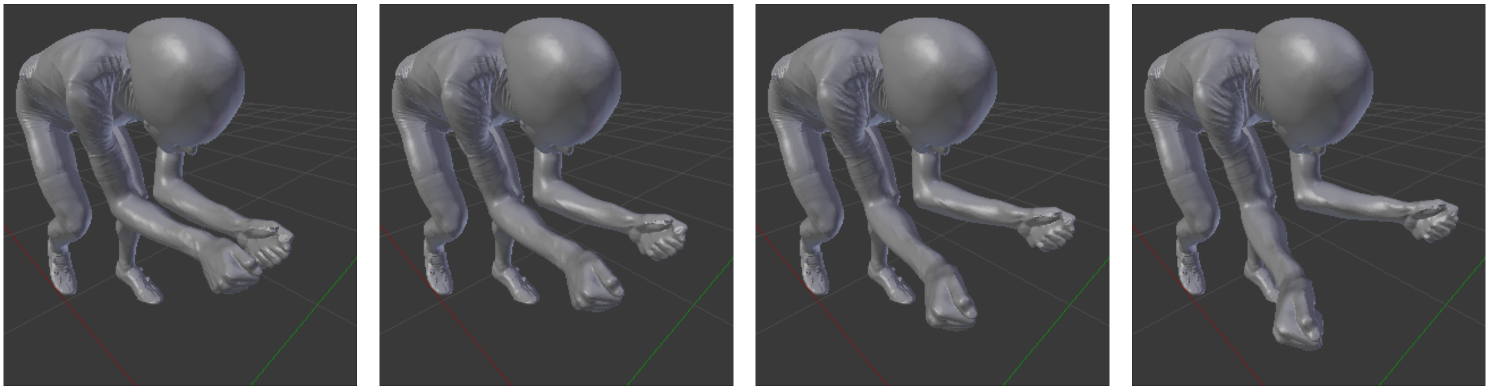

(i) Elbow extension = 0.625
Distance between hands = 0.125

(j) Elbow extension = 0.625
Distance between hands = 0.375

(k) Elbow extension = 0.625
Distance between hands = 0.625

(l) Elbow extension = 0.625
Distance between hands = 0.875

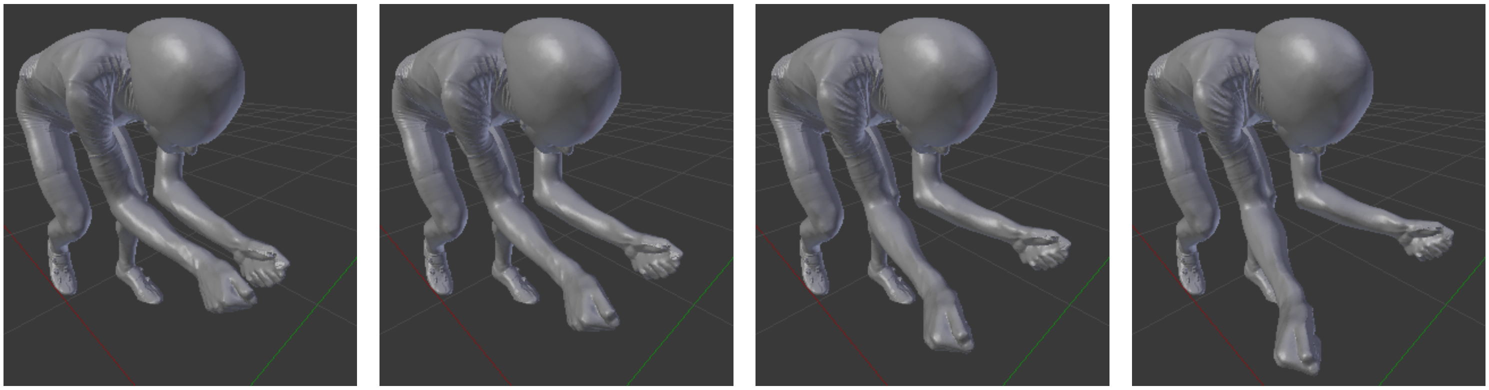

(m) Elbow extension = 0.875
Distance between hands = 0.125

(n) Elbow extension = 0.875
Distance between hands = 0.375

(o) Elbow extension = 0.875
Distance between hands = 0.625

(p) Elbow extension = 0.875
Distance between hands = 0.875

Models with elbows fairly close (elbow position = 0.375)

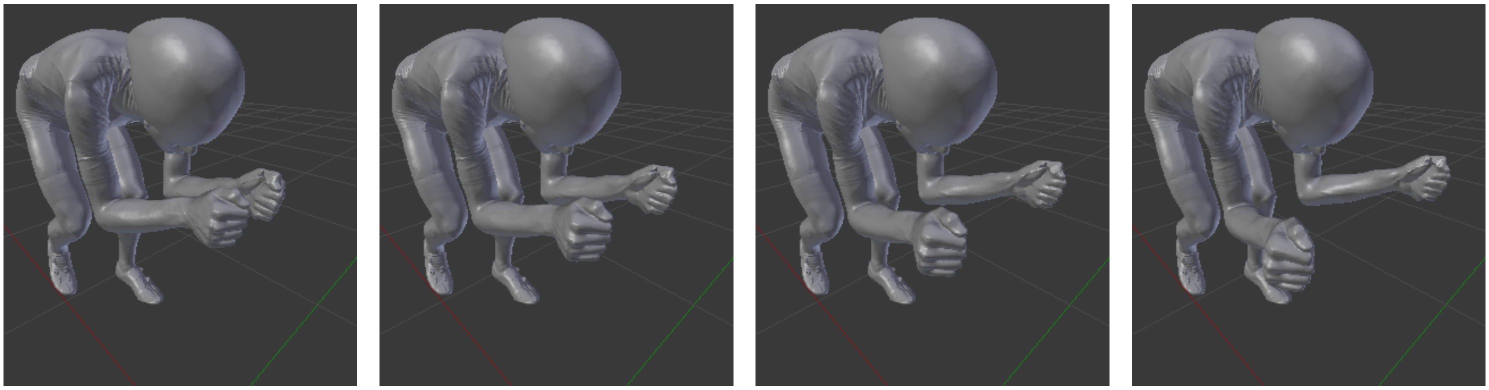

(a) Elbow extension = 0.125
Distance between hands = 0.125

(b) Elbow extension = 0.125
Distance between hands = 0.375

(c) Elbow extension = 0.125
Distance between hands = 0.625

(d) Elbow extension = 0.125
Distance between hands = 0.875

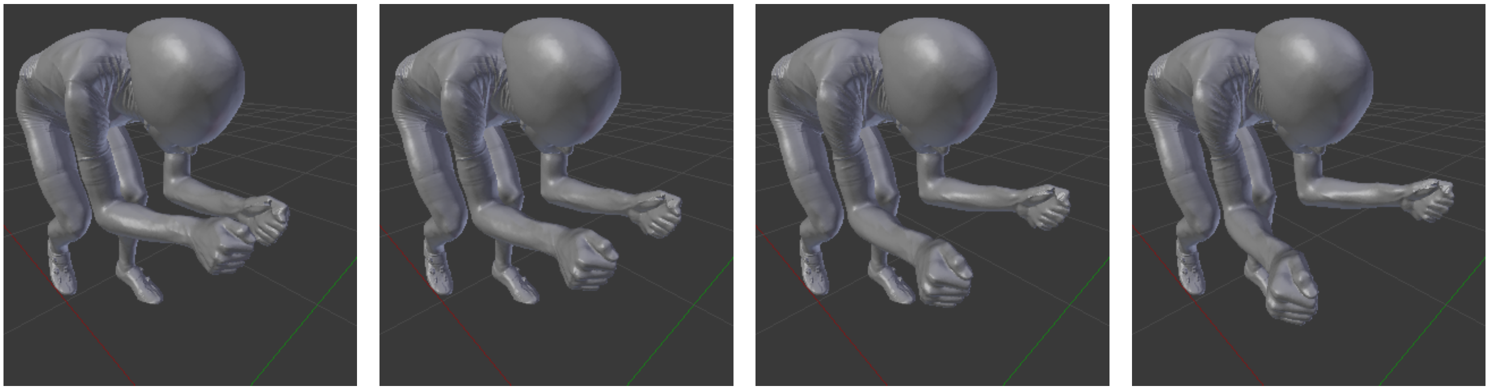

(e) Elbow extension = 0.375
Distance between hands = 0.125

(f) Elbow extension = 0.375
Distance between hands = 0.375

(g) Elbow extension = 0.375
Distance between hands = 0.625

(h) Elbow extension = 0.375
Distance between hands = 0.875

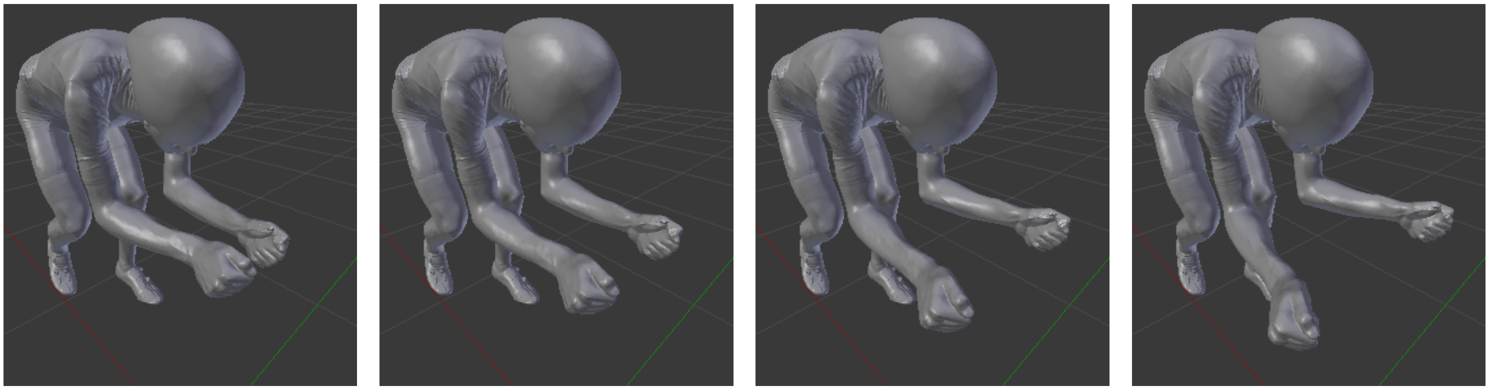

(i) Elbow extension = 0.625
Distance between hands = 0.125

(j) Elbow extension = 0.625
Distance between hands = 0.375

(k) Elbow extension = 0.625
Distance between hands = 0.625

(l) Elbow extension = 0.625
Distance between hands = 0.875

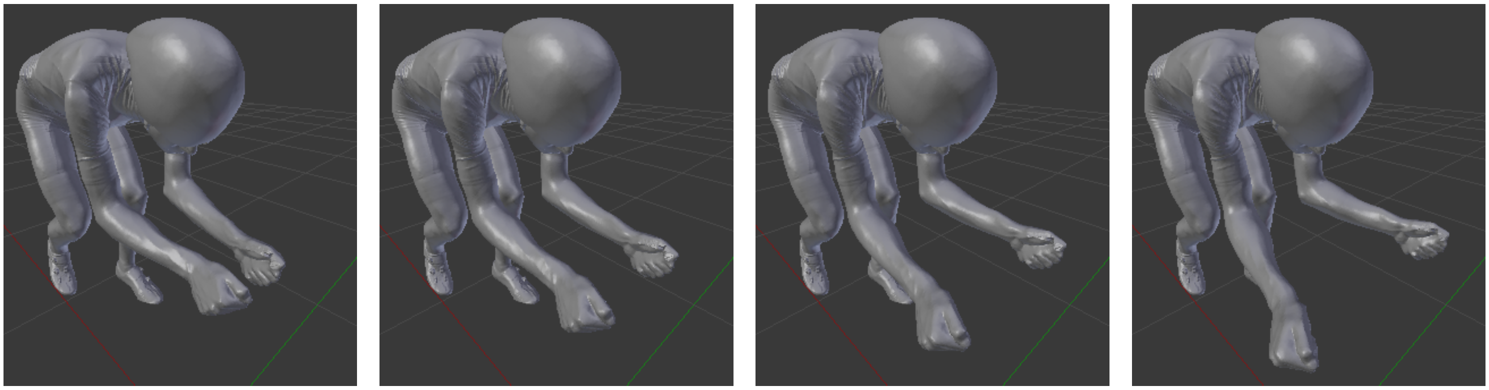

(m) Elbow extension = 0.875
Distance between hands = 0.125

(n) Elbow extension = 0.875
Distance between hands = 0.375

(o) Elbow extension = 0.875
Distance between hands = 0.625

(p) Elbow extension = 0.875
Distance between hands = 0.875

Models with elbows shoulder width apart (elbow position = 0.625)

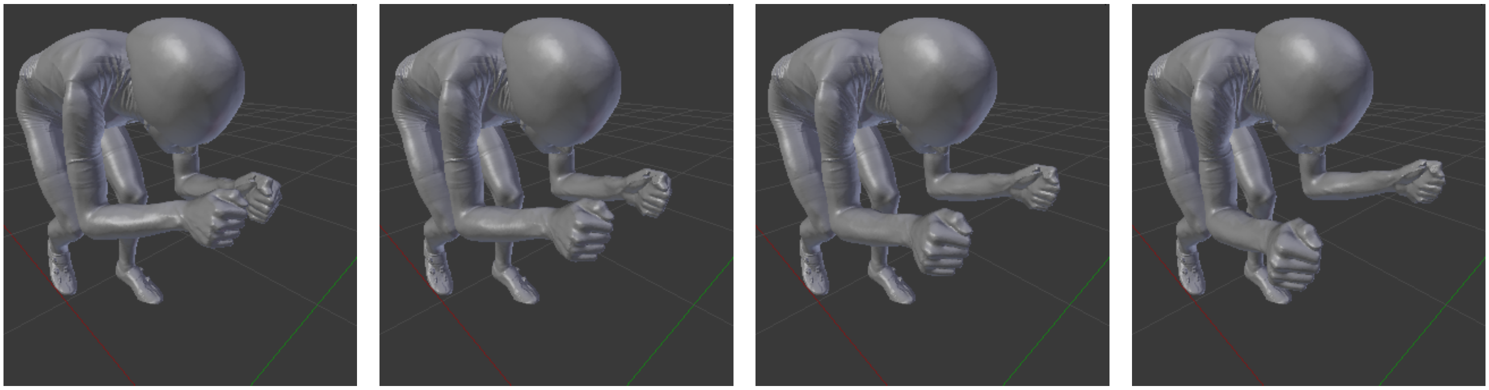

(a) Elbow extension = 0.125
Distance between hands = 0.125

(b) Elbow extension = 0.125
Distance between hands = 0.375

(c) Elbow extension = 0.125
Distance between hands = 0.625

(d) Elbow extension = 0.125
Distance between hands = 0.875

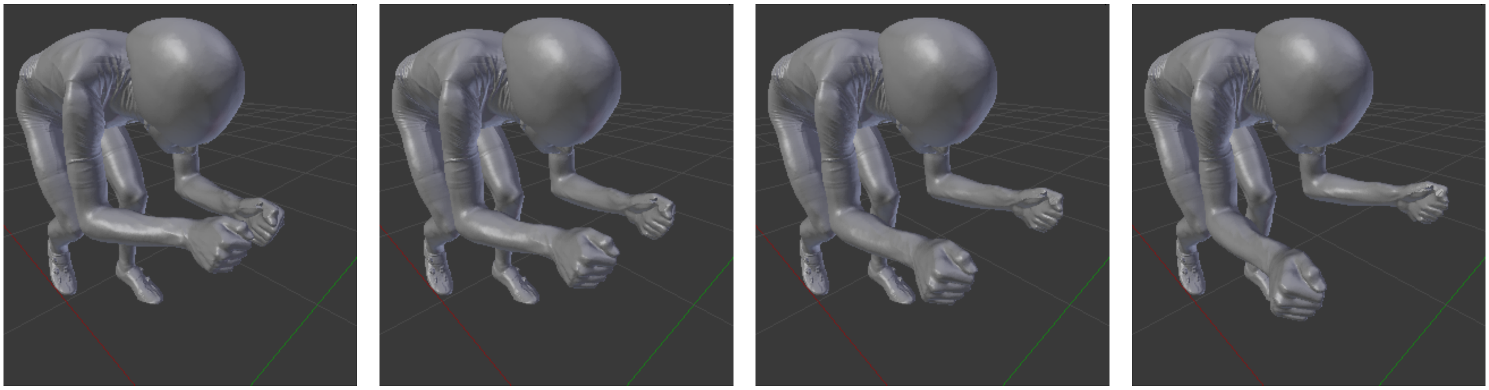

(e) Elbow extension = 0.375
Distance between hands = 0.125

(f) Elbow extension = 0.375
Distance between hands = 0.375

(g) Elbow extension = 0.375
Distance between hands = 0.625

(h) Elbow extension = 0.375
Distance between hands = 0.875

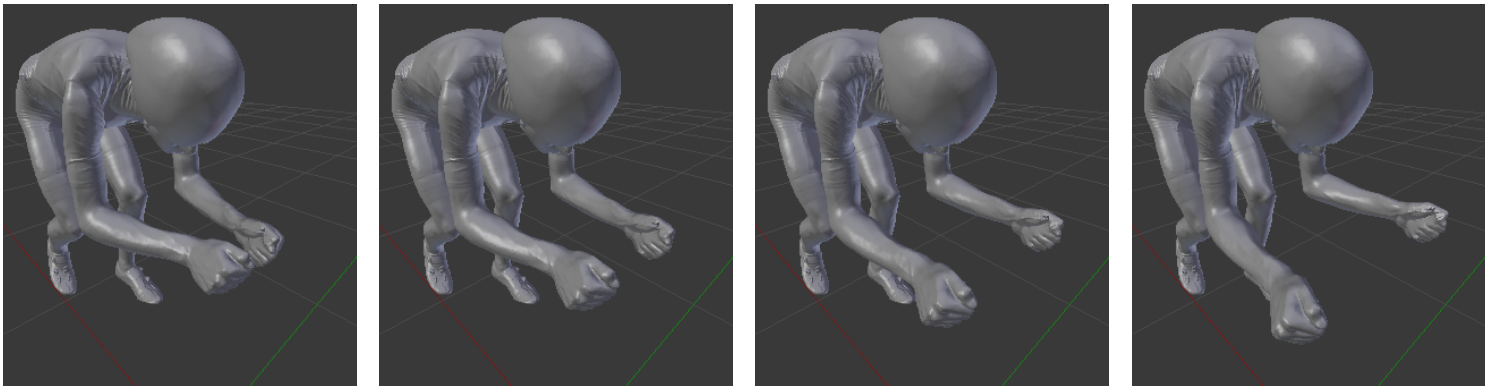

(i) Elbow extension = 0.625
Distance between hands = 0.125

(j) Elbow extension = 0.625
Distance between hands = 0.375

(k) Elbow extension = 0.625
Distance between hands = 0.625

(l) Elbow extension = 0.625
Distance between hands = 0.875

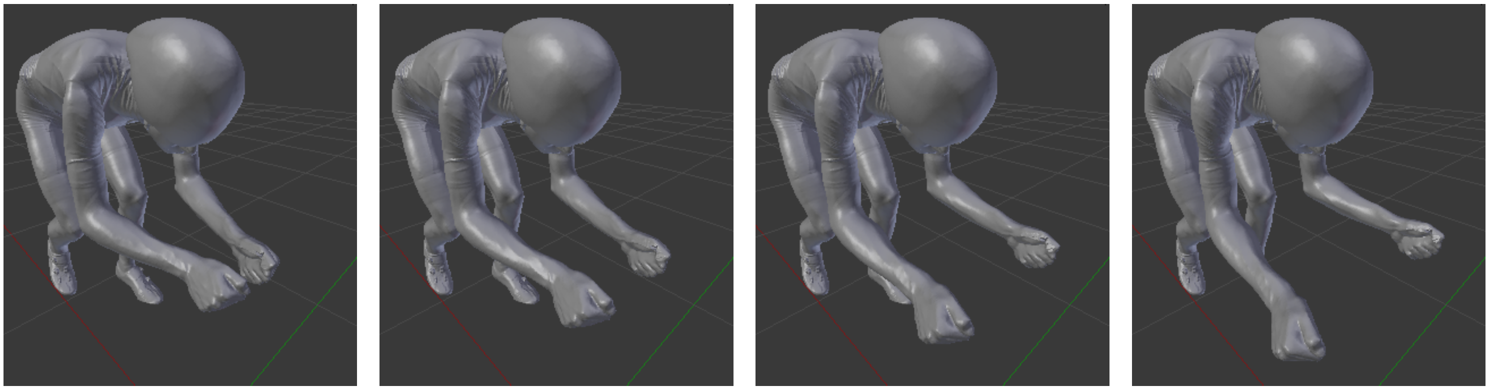

(m) Elbow extension = 0.875
Distance between hands = 0.125

(n) Elbow extension = 0.875
Distance between hands = 0.375

(o) Elbow extension = 0.875
Distance between hands = 0.625

(p) Elbow extension = 0.875
Distance between hands = 0.875

Models with elbows more than shoulder width apart (elbow position = 0.875)

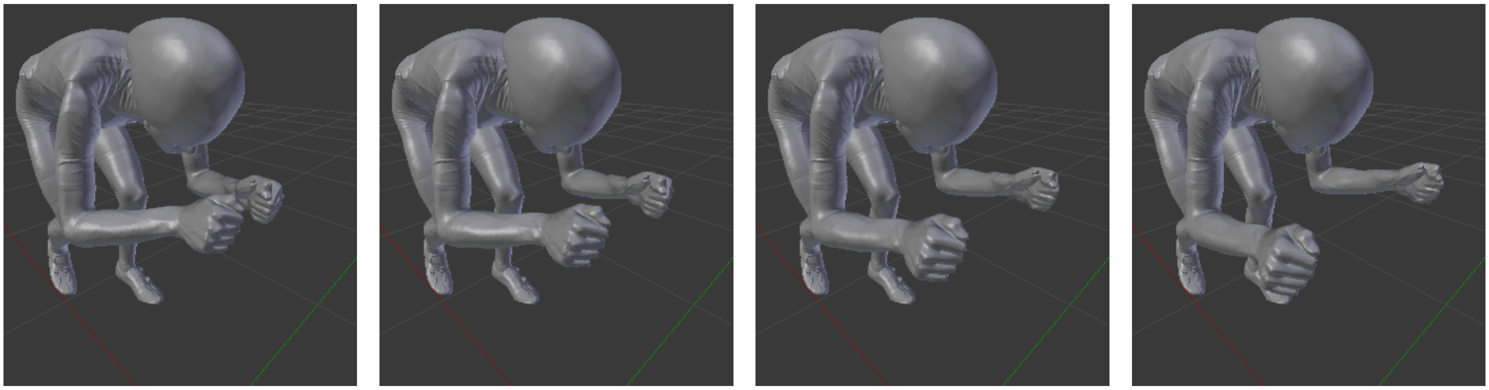

(a) Elbow extension = 0.125
Distance between hands = 0.125

(b) Elbow extension = 0.125
Distance between hands = 0.375

(c) Elbow extension = 0.125
Distance between hands = 0.625

(d) Elbow extension = 0.125
Distance between hands = 0.875

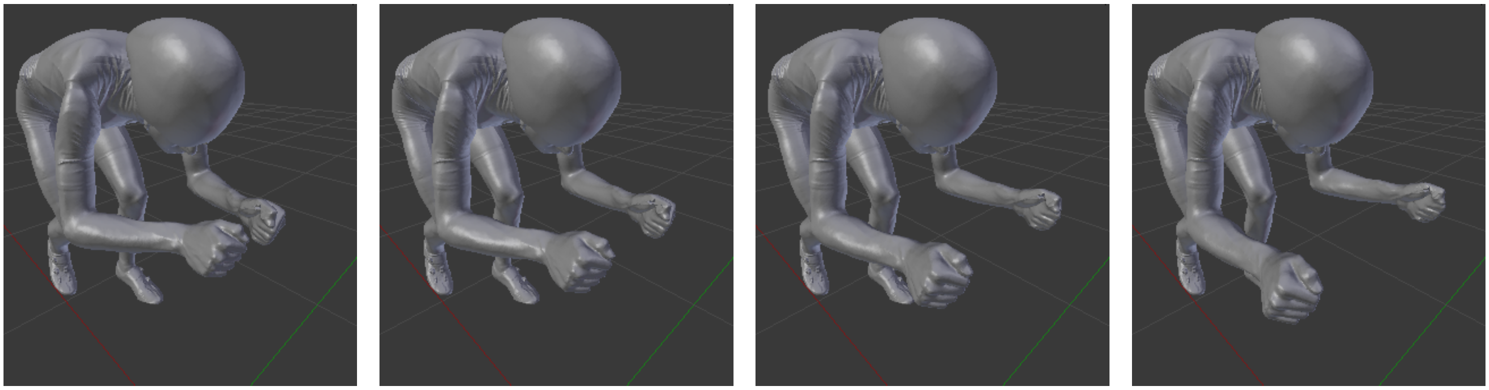

(e) Elbow extension = 0.375
Distance between hands = 0.125

(f) Elbow extension = 0.375
Distance between hands = 0.375

(g) Elbow extension = 0.375
Distance between hands = 0.625

(h) Elbow extension = 0.375
Distance between hands = 0.875

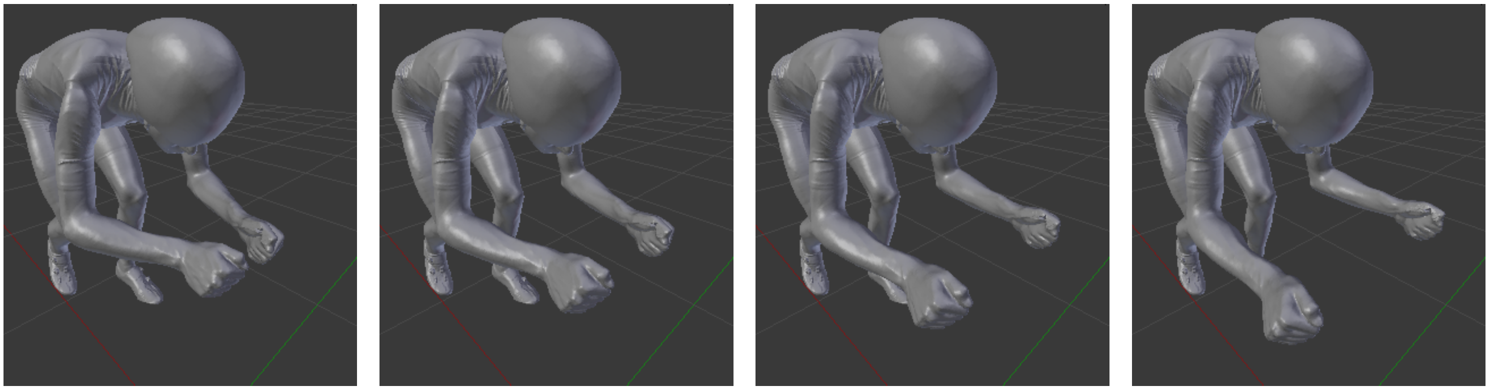

(i) Elbow extension = 0.625
Distance between hands = 0.125

(j) Elbow extension = 0.625
Distance between hands = 0.375

(k) Elbow extension = 0.625
Distance between hands = 0.625

(l) Elbow extension = 0.625
Distance between hands = 0.875

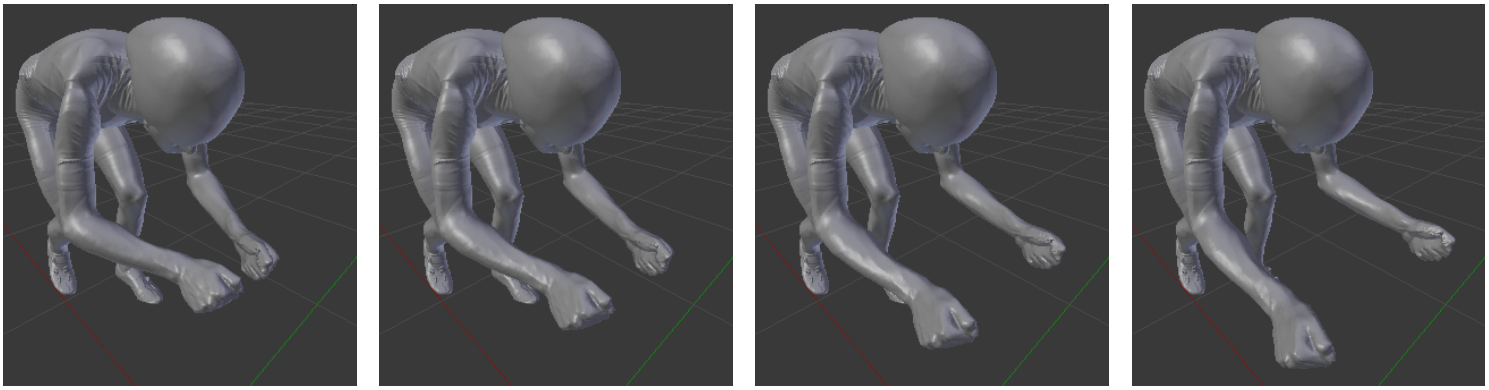

(m) Elbow extension = 0.875
Distance between hands = 0.125

(n) Elbow extension = 0.875
Distance between hands = 0.375

(o) Elbow extension = 0.875
Distance between hands = 0.625

(p) Elbow extension = 0.875
Distance between hands = 0.875